Dynamics Modeling and Control of Variable Length Remotely Operated Vehicle Tether

by

Sairam Prabhakar
B. Eng., University of Bombay, 2002

A Thesis Submitted in Partial Fulfillment of the
Requirements for the Degree of

MASTER OF APPLIED SCIENCE

in the Department of Mechanical Engineering

We accept this thesis as conforming
to the required standard

Dynamics Modeling and Control of Variable Length Remotely Operated Vehicle Tether

by

Sairam Prabhakar
B. Eng., University of Bombay, 2002

A Thesis Submitted in Partial Fulfillment of the
Requirements for the Degree of

MASTER OF APPLIED SCIENCE

in the Department of Mechanical Engineering

We accept this thesis as conforming
to the required standard

Dr. B. Buckham, Supervisor (Dept. of Mechanical Engineering)

Dr. E. Park, Departmental Member (Dept. of Mechanical Engineering)

Dr. S. Dost, Departmental Member (Dept. of Mechanical Engineering)

Dr. R. Dewey, External Examiner (University of Victoria)

Supervisor: Dr. Brad Buckham.

Abstract

In this work, a computational model is developed to simulate the dynamics of variable length tether in a tethered underwater vehicle system. The system is comprised of a surface ship and winch, a slender armored cable that links the surface ship and the remotely operated vehicle (ROV), and the ROV itself. The cable is considered to be variable length to facilitate paying out and reeling in maneuvers. The motion equation for variable length tether is obtained from Newton's second law of motion for variable mass systems. Unlike many existing formulations, the model can treat the rapid deployment and retrieval of tether accurately. The Weighted Residual Finite Element technique is applied to the continuous motion equation to obtain a system of spatially discrete nonlinear second order differential equations. Time domain simulation of variable length maneuvers is used to validate the performance of the model for low and high tension cable states

The model is applied to the development of a dynamic positioning system for a submerged point on the tether, called the control node, for the Remotely Operated Platform for Ocean Sciences (ROPOS) operated by the Canadian Scientific Submersible Facility (CSSF). A decoupled controller incorporating a Dahlin Controller for positioning in the longitudinal plane and a PD Controller for depth regulation produces ship motion and winch activity to position the control node. It is shown that the use of the control system to regulate the position of the control node brings about significant reduction in the disturbance force exerted by the tether on the ROV during a station-keeping maneuver.

Dr. B. Buckham, Supervisor (Dept. of Mechanical Engineering)

Dr. E. Park, Departmental Member (Dept. of Mechanical Engineering)

Dr. S. Dost, Departmental Member (Dept. of Mechanical Engineering)

Dr. R. Dewey, External Examiner (University of Victoria)

Table of Contents

List of Figures

Acknowledgements

There could be no better day than this, Thanksgiving, 2005, to acknowledge the contributions of the individuals who made this work possible.

To my parents, who I owe a debt of immense gratitude.

To family, across two continents, for opening their homes to me.

To Dr. Brad Buckham, for giving direction to my work, rigor to my thought, and encouragement when I needed it the most. Through the rest of my career, in whatever work I do, there will always be something that I have learned from him.

To Dr. Ed Park, and Dr. Sadik Dost, for taking the time to examine this work.

To Dean, Alp, Serdar and all those who stopped by and shared a moment.

Thank you all.

Chapter 1
Introduction

1.1 Robotic exploration of the deep ocean

The deep ocean remains one of the humankind's unexplored frontiers. From the influence of ocean temperature gradients on global weather to the subsea life forms that thrive in impossibly hostile environments, the deep ocean bears a wealth of unexplored science. However, doing science in the deep ocean is no trivial matter. The high risks involved in delivering a human to the ocean depths have largely impeded scientific inquiry for the last century.

Robotic systems that have evolved over the last half century offer an effective alternative to human intervention. As an example, the recent NEPTUNE and VENUS projects (Delaney et al. [1]) off the coast of British Columbia and Washington state aim to establish lasting deep ocean sensing systems by integrating advanced robotic and communications systems. It is envisioned that unmanned robotic platforms would play a key role in the future of the ocean sciences. These robotic platforms incorporating robotic vehicles for subsea operation are classified as either Remotely Operated Vehicles (ROVs) or Autonomous Underwater Vehicles (AUVs), depending upon the mode of control.

In ROVs, the vehicle chassis bears end-effectors and sensing systems, and is propelled by several thrusters. The entire system is linked to the deployer vessel on the

surface by means of a fiber optic cable called the tether or umbilical. The umbilical serves as a high bandwidth conduit for power and telemetry affording simultaneous control of the vehicle thrusters, the instrument payload, and the robotic end-effector by a human operator in the surface vessel. AUVs are not tethered to the deployer vessel and rely on onboard computers for motion control.

1.2 Remotely Operated Vehicle Systems

As of the present time, AUVs cannot be programmed to handle a wide range of operating circumstances, payloads and ancillary devices, and hence have limited operational capability. The human-in-the-loop nature of ROV control enables them to perform a wide variety of underwater tasks. ROVs are also a mature technology and, as such, more reliable than AUVs in the unpredictable deep ocean environment. As a result, ROVs remain the umanned platform of choice for a wide variety of subsea intervention tasks.

Figure 1.1 shows the range of ROV sizes and capabilities. Figure 1.1 (a) shows a small tethered ROV used for observation. Figure 1.1 (b) shows a large ROV that is equipped with dexterous robotic arms.

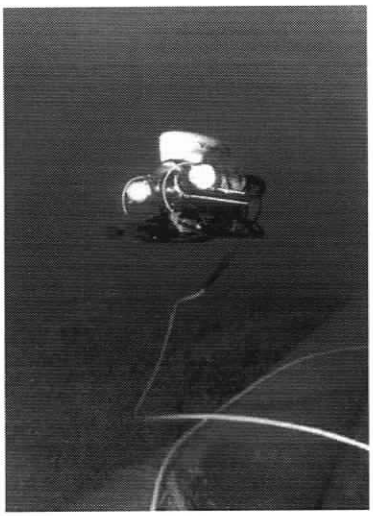

(a)

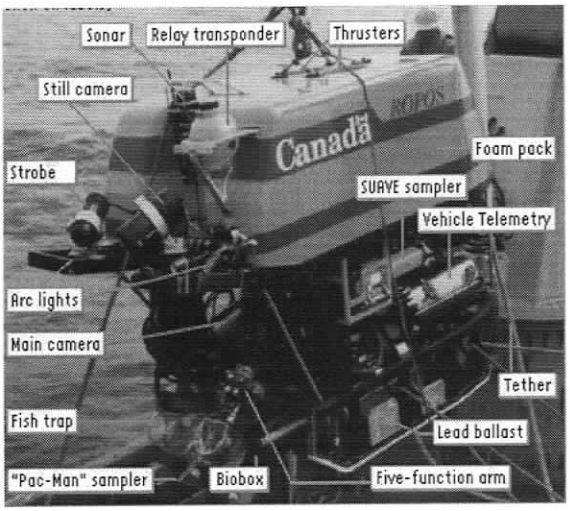

(b)

Figure 1.1 (a): An Inspection Class ROV (b) The Work Class ROV ROPOS

Figure 1.1: The range ROV sizes for different applications. Figure 1.1 (a) shows a small ROV designed primarily for observation. It is light weight and mainly bears vision sensors. Figure 1.2 (b) shows the larger Work Class ROV ROPOS (Remotely Operated Platform for Ocean Science) operated by the Canadian Scientific Submersible Facility (CSSF). It is bulkier in design and carries a number of end-effectors capable of performing dexterous tasks deep underwater.

Typically, the ROV system functions in two modes:

1. The two-body system, where the vehicle is linked to the deployer vessel through an intermediate heavy cage. This is shown in Figure 1.2 (a). The winch regulating the ROV tether in this case is located in the cage and the cage is linked to the deployer vessel.

2. The liveboating system, where the vehicle is linked directly to the ship. Here there is no intermediate cage and the ROV is run directly off the ship. This is shown schematically in Figure 1.2 (b).

Figure 1.2 (a) : A caged ROV system being deployed off the ship. The cage or garage bearing the ROV is linked to the ship through an armored tether and is used to position the ROV. The ROV umbilical links the ROV to the cage, both of which are underwater.

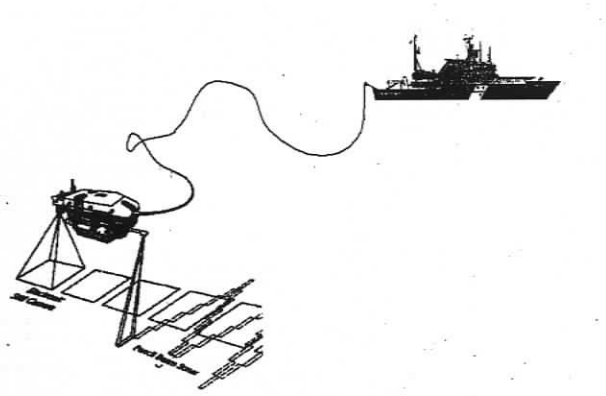

Figure 1.2 (b): Liveboating ROV performing a bathymetric survey. Here, in the absence of the cage, the ROV is driven straight off the winch on the vehicle. This eliminates the possibility of snap loads due to the intermediate cage as in Figure 1.2 (a) and reduces the weight of the entire system but could increase the drag on the ROV due to the larger amount of bare ROV cable in the water, and also create problems while positioning the ROV in the absence of the intermediary cage.

Figure 1.2: Different modes of operation of the ROV system. In this work, we are particularly interested in the liveboating configuration (Figure 1.2 (b)) of the ROV ROPOS shown in Figure 1.1 (b) at depths in excess of 2000 meters.

1.3 The need for ROV Tether Dynamics Modeling

The large Work Class ROV ROPOS of Figure 1.1 (b) operates at depths greater than 2000 meters in the liveboating mode of Figure 1.2 (b). The greater the operating depth, the greater is the amount of tether in the water. Consequently the vehicle thrusters have to work harder to overcome the hydrodynamic drag of the long submerged cable. In this Section, the role of tether dynamics modeling in advanced ROV applications is highlighted.

1.3.1 Tether Dynamics Modeling for Advanced ROV Applications

The ROV system consists of the vehicle, linked by flexible tether to the deployer vessel. For the large liveboating Work Class ROV systems operating at depths greater than 2000 meters, the dynamics of the vehicle and the tether are strongly coupled, and the prominence of the effect of the tether dynamics on the vehicle dynamics has sometimes led it to be described as the "tail that wags the dog." Modeling the dynamics of the tether in the time domain consequently plays an important role in advanced ROV operations. One such advanced application is the use of the dynamics model of the tether for controller synthesis, as will be shown in the present work. Here, in Chapter 5, the tether dynamics model is used to synthesize a controller to regulate the position of a single submerged point on the tether, called the control node, to significantly reduce the disturbance force exerted by the tether on the vehicle. Other possible applications involve the use of the dynamics models of the tether in vehicle navigation and the design of interactive pilot training simulators. As an example, ROV simulators would enable ROV crews to resolve their operational limits in terms of what sea states would permit

the achievement of specific mission goals. These objectives have driven the research into underwater vehicle cable dynamics over the past decade.

1.3.2. The Role of Variable Length Tether Dynamics Modeling

The deployed span of cable linking the ROV to the ship is not fixed in length over the course of an ROV mission. During deployment and retrieval of the ROV, cable length is varied using the winch mounted on the ship. It is also common practice to pay in or reel out cable during the operation of the vehicle to overcome the effects of inappropriate deployed tether length on vehicle maneuverability. For instance, a very short tether would pull on the ROV while excessively long submerged tether could accumulate drag along its span to swamp the vehicle thrusters.

Most existing time domain simulations of the ROV tether provide high fidelity models of the cable and vehicle for a constant length of umbilical. However in order to realize complete generality to model all phases of ROV operation, it is essential that the time domain simulation be able to deal with varying tether length. It is also envisioned that a variable length time domain simulation would enable the synthesis of a novel tether winch control system to augment the existing thruster control on the underwater vehicle.

1.4 Computational Underwater Tether Dynamics Modeling

In this Section, a brief review of existing work on underwater tether dynamics modeling is presented. Subsection 1.4.1 deals with previously developed fixed length tether dynamics models. Next in Subsection 1.4.2, past developments in variable length tether dynamics modeling are presented. The role that this work intends to play, in terms

of furthering the body of knowledge in the area of variable length tether dynamics modeling and using variable length tether dynamics models in control system design is highlighted.

1.4.1 Fixed Length Tether Dynamics Modeling

Mathematical modeling of the dynamics of submerged cables has been a topic of research for over half a century. Walton and Polachek [14] first presented a model for the dynamics of subsea cables. The spatially continuous equations were discretized in space, by modeling of the cable as a concatenation of elements, linked together at nodes. A centered finite difference scheme was used to discretize the time derivative steps to propagate the spatially discrete model in time.

The early models were applicable to taut cables. The dynamics of low tension cables have only recently been considered. Park, Jung and Koterayama [15] have shown that slack cables, where the dynamic tension is of the same order as the static tension, have significantly more complex dynamics. The small restoring force permits large three dimensional deformations of the cable, precluding the geometric linearization commonly used in the analysis of taut cables. Ablow and Schechter [16] showed that for slack cables, if the tension vanishes anywhere along the cable span, the determinant of the stiffness matrix becomes zero, resulting in an ill-posed problem. Triatafyllou and Howell [8] later showed that incorporating the bending stiffness helps overcome the singularity created by the slack cable dynamics.

During field operation of the ROV tether, it is subjected to a wide range of tension levels. In order to isolate the vehicle from disturbances originating at the deployer, the

cable is maintained at a state of low tension close to the vehicle. However, close to the deployer, the cable is often in a state of high tension. Modeling the nonlinear dynamics of the ROV umbilical subjected to high and low tension states is a challenging task. While maintaining high fidelity for taut cable dynamics modeling, it is required that the mathematical model remains well-posed in the low tension regions of the cable. Buckham et al [11] present a numerical model of the cable dynamics meeting these requirements. The salient features of this model are the inclusion of bending and torsional stiffness which capture the flexural and torsional dynamics dominating the response of slack cables. The only state variables required are the three positions and three velocities of each node in the spatially discrete model. This reduces the number of state variables, enabling computationally efficient simulation of the cable dynamics.

1.4.2 Variable Length Tether Dynamics Modeling

Closely related to the tethered underwater vehicle systems under consideration in this work, are the Tethered Satellite Systems (TSS). The majority of research in variable length tethered systems has been conducted for TSS. Deployment rate control is an important aspect in the operation of a TSS. A considerable body of literature exists on the dynamics modeling of varying length TSS tethers. The idea of using a long tether to support a satellite from an orbiting platform was proposed in 1974 by Colombo [2]. The first TSS mission was launched in late summer 1992. There have been several missions since then. Along with empirical testing there has been great interest in computational dynamics models for tethered satellite systems. This has led to two standard computational packages for variable length space tether modeling used by space agencies

around the world. They are the Generalized Tether Object Simulation System (GTOSS) and the Dynamic Interaction Simulator (DIS) (Leamy et al [3]). In GTOSS the number of discrete elements concatenated to form the tether is constant and the length of all elements is increased or decreased uniformly to simulate variable length. In DIS the number of fixed length elements is varied to model varying tether length.

In space, the tether largely remains taut and straight and is not subjected to the large, three dimensional deformations that are characteristic of slack submerged cables, thereby making the dynamics and control of space tethers more tractable. On the other hand, few instances of work deal with underwater systems with varying tether length. Kamman and Houston develop a model for varying the tether length for a towed body in [4]. However their model considers length change as a passive phenomenon and make no account for thrust forces that accompany the forced payout of tether at the winch termination. Rather, the nominal length of the finite segments representing the cable closest the deployer are adjusted on a time-based schedule. Bannerjee and Do [5] present a tether tension control system for a towed underwater vehicle using varying cable lengths. Makarenko et al [6] and Badour and Raman-Nair [7] also develop dynamics models for variable length tethered underwater systems. In all of the above cases, the cable is modeled as a chain of rigid rods. The cable profile in space is modeled by a linear interpolation of node points and bending and torsional stiffnesses are neglected. However, as discussed in Section 1.4.1, neglecting the bending stiffness leads to an ill-posed problem for low tension cable dynamics. Hence it remains to develop a variable length model based on a tether representation with low-tension capabilities.

Burgess presented a model for variable length underwater tether dynamics incorporating bending stiffness [9]. However, in this case, the variable length dynamics are mapped over the entire cable span. This is analogous to the DIS model of space tethers and, as will be shown in Chapter 3 of this work, corresponds to the Lagrangian approach to modeling the variable length dynamics: where the observer moves with the cable being deployed or retrieved. However, as will be shown in Chapter 3, it is desirable to use an Eulerian approach, where the variable length effect is modeled only at the interface of the winch and the deployed cable span. One of the objectives of this work is to develop a variable length cable model using an Eulerian formulation, capable of handling both high and low tension cable dynamics. As will be discussed in Chapter 3, the Eulerian formulation is a natural fit for finite segment cable models such as those of Kamman and Huston [4] or finite element models of Buckham et al [11].

Another issue that has seldom been addressed in the literature is the possibility of using the deployer vessel for dynamic positioning of an underwater point on the long submerged cable. Figure 1.3 shows a schematic of a tethered underwater vehicle linked to the deployer vessel through the umbilical in the liveboating configuration.

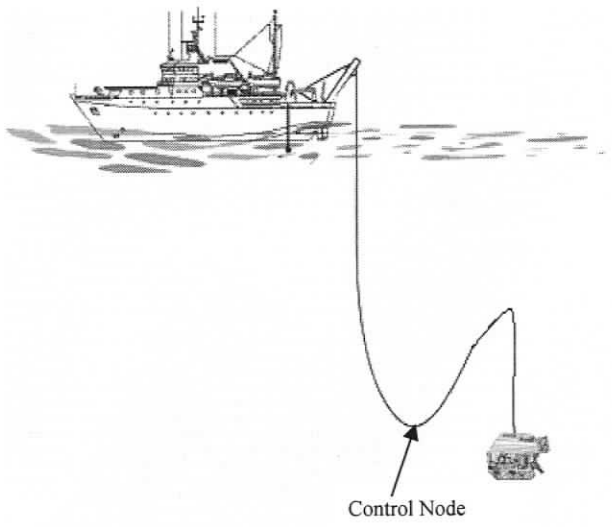

Figure 1.3: Tethered Underwater Vehicle operating in the liveboating configuration. The absence of the cage as in the two-body system of Figure 1.2 (a) makes the position control of the ROV a difficult problem. In this work, the position control strategy developed relies on the positioning the point labeled as the Control Node.

The tether is configured in the form of an S-curve close to the vehicle through the use of floats. In Chapter 5, a control system is investigated for the positioning of the control node using a combination of ship motion and tether payin/payout from the winch on board the ship, using the position of the control node as the feedback signal. It is envisioned that regulating the position of the control node would help reduce the disturbance exerted by the cable on the vehicle in the face of an ocean current.

The presence of a large time delay between ship motion and ROV motion for typical cable lengths, greater than 2000 meters, makes the closed loop dynamic positioning of the control node a difficult problem. Triantafyllou and Grosenbaugh use the Smith Predictor to develop a closed loop positioning system [10]. This continuous control

strategy relies on a continuous stream of cable bottom position data. Given the finite rate of position updates realized with an acoustic measurement system, it remains to clarify if a controller can be effectively implemented in the discrete time domain.

1.5 Thesis Overview

The objective of this thesis is twofold. The first objective is to develop a time domain simulation to model the dynamics of variable length underwater tether. This is achieved by augmenting the finite element formulation for fixed length tether dynamics of Buckham et al [11] with a variable length boundary, or thrust, element that can be assembled with the constant length elements.

The second objective of this work is to investigate the use of a discrete time control algorithm for systems with large dead time, the Dahlin Controller, to develop a closed loop dynamic positioning system for an underwater point on the ROV cable using winch deployment/retrieval of cable and surface ship motion as control signals.

Chapter 2 reviews mathematical models for fixed length underwater cable dynamics. The geometric nonlinearity and ill-posed nature of low tension cable dynamics is discussed. Starting from first principles of the balance of linear and angular momentum, a dynamics model for fixed length cable dynamics is formulated. The discretization in space by Galerkin's Weighted Residual Finite Element technique is demonstrated. This provides the necessary basis for the discussion of the variable length cable dynamics model in subsequent Chapters.

Chapter 3 covers the theoretical aspects of formulating a dynamical model for variable length tether. Newton's second law of motion for variable mass systems is reviewed. It is

applied to the dynamics of a rocket and also to the control volume analysis for the translation of a cable as shown by Tiersten [12]. The Eulerian and Lagrangian approaches to modeling the variable length cable dynamics are discussed. The equivalence between the Lagrangian approach and the work of Burgess [9] is brought out. The Eulerian approach is shown to be synergistic with Newton's second law of motion for variable mass systems. The fixed length governing dynamics equation of the cable developed in Chapter 2 is augmented with new terms to reflect the effect of variable length. The spatially discrete form of the overall variable length governing dynamics equation is obtained by the application of Galerkin's Weighted Residual technique.

Chapter 4 completes the time domain simulation of the spatially discrete dynamics of Chapter 3. Numerical examples of slack and taut cable are used to illustrate the ability of the dynamics model to simulate variable length tether. The need for rediscretization in order to maintain the integrity of the model is highlighted. Conservation of strain energy is shown to hold during the rediscretization time steps.

Chapter 5 describes the synthesis of a control system for positioning of a submerged point on the ROV cable called the control node, described in Figure 1.3. The ROV system simulated is the ROPOS vehicle operated by the CSSF, depicted in Figure 1.1(b). A decoupled controller using the Dahlin controller for longitudinal positioning and a winch PD controller for depth regulation is shown to successfully position the control node. The final issue addressed is the positioning of the control node in the face of an ocean current. It is shown that by regulating the control node position when the system is subjected to an ocean current, a significant reduction is realized in the disturbance force exerted by the tether on the ROV during a station-keeping maneuver.

1.6 Thesis Contributions

This work has two main objectives, as described in Section 1.5. It focuses on the development of a computational dynamics model for variable length ROV tether, and investigates the design of a position control system for a submerged control node on the tether. Correspondingly, the chief contributions of this work are:

1. The development of a variable length cable dynamics model that appends the fixed length element equations. This formulation will capture the effects of rapid deployment/retrieval of ROV cable that is missing in a majority of existing models.
2. The development of a discrete time controller for an underwater point on the cable. It will be shown that the resultant position regulation capability of the controller designed here brings about a significant reduction in the disturbance force exerted by the tether on the vehicle. This will expand the range of vehicle operating conditions, and has the potential to save thousands of dollars in ship time, during ROV deployment.

Chapter 2

Remotely Operated Vehicle Tether Dynamics Modeling

2.1 Overview

Before developing the dynamics model for variable length underwater vehicle tether, which is the objective of this work, it is necessary to start with a review of existing dynamics models for fixed length tethers. In this Chapter the dynamics formulation for ROV tether subject to low and high tension states is presented. Section 2.2 describes a tether dynamics model starting from the expressions for the balance of linear and angular momentum. The Galerkin Weighted Residual Finite Element technique is shown to produce the spatially discrete governing dynamics equations. The resulting model is computationally efficient, and capable of simulating low and high tension cable dynamics.

2.2 Dynamics Model for fixed length tether dynamics

As detailed in Chapter 1, the work of Buckham et al [11] provides a numerical model capable of modeling both low and high tension underwater tether states using only the positions and velocities of the nodes as the state variables. These distinguishing features make this model the basis for the present work, with the subsequent Chapters dealing with the extension of the fixed length cable dynamics model to incorporate the effects of

varying tether length. In the following subsections we review the key aspects of the fixed length cable dynamics formulation.

2.2.1 Foundations

Consider the schematic of the tethered ROV system shown in Figure 2.1.

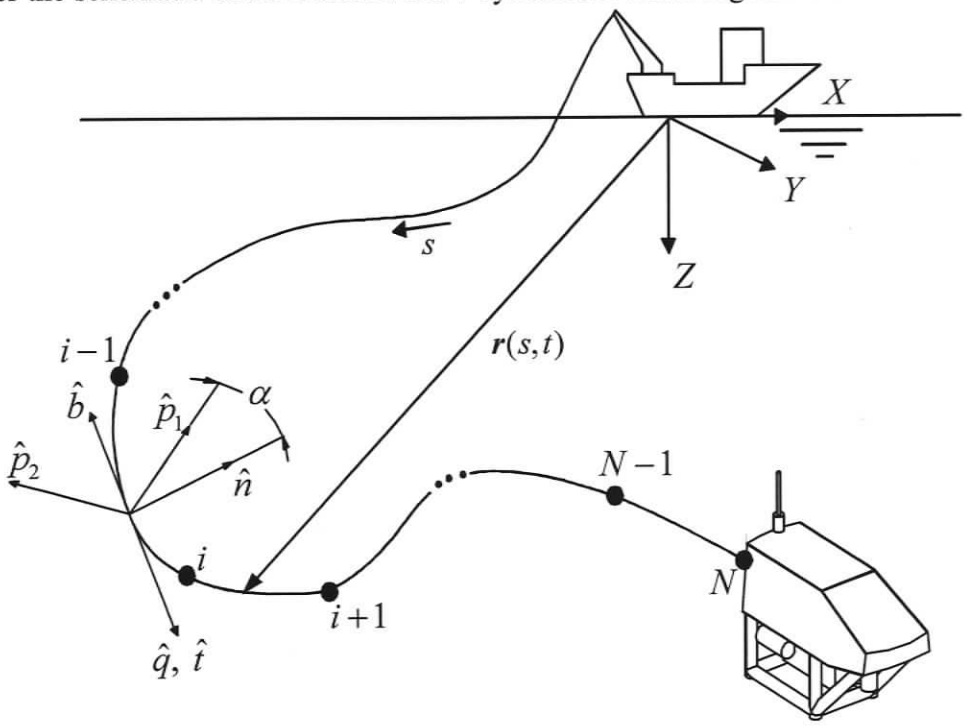

Figure 2.1: Schematic of the tethered ROV system. The robotic platform or ROV is linked to the deployer vessel through the flexible umbilical or tether. The discretized tether is a concatenation of cubic spline elements, where the i^{th} element is bounded by the $(i-1)^{th}$ and i^{th} nodes. Each element has an associated $\left(\hat{\mathbf{t}},\hat{\mathbf{n}},\hat{\mathbf{b}}\right)$ Frenet Frame and the $\left(\hat{\mathbf{t}},\hat{\mathbf{p}}_1,\hat{\mathbf{p}}_2\right)$ Local Reference Frame as shown

The free body diagram of a differential cable element of length ds is shown in Figure 2.2.

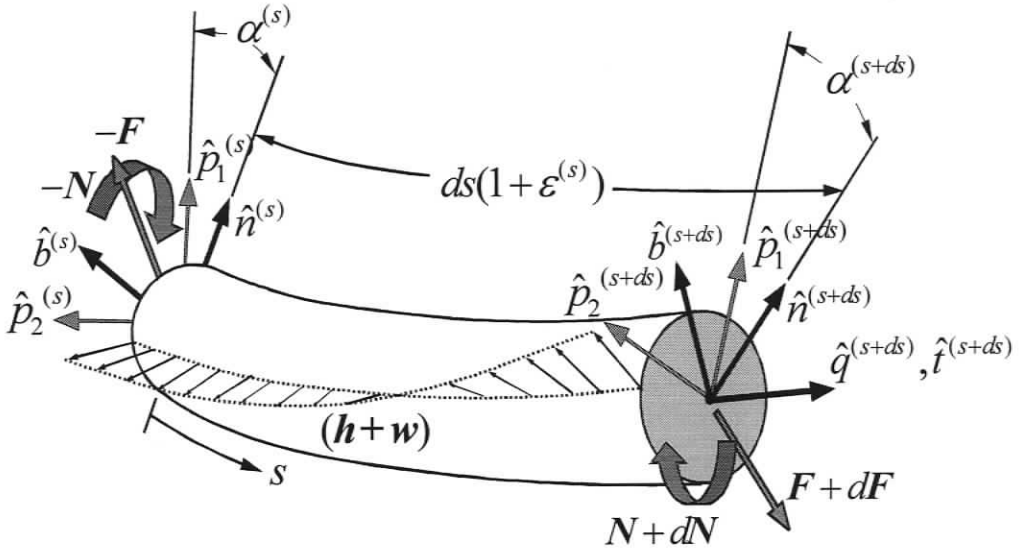

Figure 2.2: Free Body Diagram of the differential cable element. An additional degree of freedom α specifies the orientation of the body-fixed frame relative to the Frenet frame.

The center line or neutral axis of the cable is a space curve which is specified by giving its position vector $\mathbf{r}$ in the inertial (**XYZ**) frame of Figure 2.1, as a function of the unstretched curvilinear coordinate or arc length s and time t. According to Nordgren [17], the internal state of stress at any point on the cable is fully characterized by the resultant force $\mathbf{F}$ and the couple $\mathbf{N}$ acting about the central axis, as shown in Figure 2.2. The balance of linear momentum is given by:

$$\mathbf{F}' + \mathbf{q} = \left(\frac{1}{4}\pi d_c^{\,2}\rho_c\right)\ddot{\mathbf{r}} \qquad (2.1\text{ a})$$

Where $\mathbf{F}$ is the resultant internal force under the action of the external distributed load of $\mathbf{q}$ per unit length which is the resultant of the hydrodynamic load $\mathbf{h}$ and buoyancy force $\mathbf{w}$ in Figure 2.2, d_c is the effective diameter of the cable comprising of the wired core within the protective sheath, and ρ_c is the density of the cable, including the water

trapped in the voids between the strands. The superscript $(')$ represents differentiation with respect to the unstretched arc length s while the superscript $\left(\dot{}\right)$ represents differentiation with respect to time t. The hydrodynamic load $\mathbf{h}$ consists of two components, a normal component, and a tangential component, relative to the differential segment. Hence, a hydrodynamic frame, $(\hat{x} \quad \hat{y} \quad \hat{z})$ is defined, where $\hat{z}$ is along the local tangent to the differential segment, $\hat{x}$ is along the normal, and $\hat{y}$ completes the right-handed triad. The mapping between the hydrodynamic frame, and the inertial frame within which the other quantities are described, can be realized through a *Z-Y-X* $(\psi \quad \theta \quad \phi)$ Euler angle rotation scheme. In terms of the inertial frame of reference, the hydrodynamic and buoyancy loads acting on the differential segment are given by:

$$\mathbf{h} = -1/2\rho_W d_C (\dot{\mathbf{r}}\cdot\dot{\mathbf{r}})\mathbf{R}_{IH}\begin{bmatrix} f_p C_D \dfrac{v_{\hat{x}}}{\sqrt{v_{\hat{x}}^2 + v_{\hat{y}}^2}} \\ f_p C_D \dfrac{v_{\hat{y}}}{\sqrt{v_{\hat{x}}^2 + v_{\hat{y}}^2}} \\ -\mathrm{sgn}(v_{\hat{z}}) f_q C_D \end{bmatrix} \qquad \mathbf{w} = (\rho_C - \rho_W)\frac{\pi (d_C)^2}{4}\mathbf{g} \tag{2.1b}$$

Where $\mathbf{R}_{IH}$ is the rotation matrix relating the hydrodynamic reference frame described above, to the inertial reference frame, f_p and f_q are the hydrodynamic loading coefficients in the normal and tangential directions respectively, ρ_w is the water density, $v_{\hat{x}}$, $v_{\hat{y}}$, and $v_{\hat{z}}$ are the components of the differential segment velocity $\mathbf{v}$, and C_D is the normal hydrodynamic drag coefficient (Buckham [11]).

Neglecting the shear deformation, the balance of angular momentum is given by:

$$\mathbf{N}' + \hat{\mathbf{t}} \times \mathbf{F} + \mathbf{n} = \frac{d\left([\mathbf{J}]\dot{\boldsymbol{\theta}}\right)}{dt} \tag{2.2 a}$$

Here, $\hat{\mathbf{t}}$ is the unit tangent vector, $\mathbf{n}$ is the applied moment per unit length (analogous to $\mathbf{q}$ described earlier), $[\mathbf{J}]$ is the tensor of mass moment of inertia per unit length of the cable, and $\dot{\boldsymbol{\theta}}$ is the vector of angular velocities. The equation (2.2 a) may be simplified by assuming static equilibrium in the rotational degree of freedom as shown by Buckham et al [11], by applying the following assumptions:

1. For the slender cable, the rotational inertia is negligible.
2. The angular acceleration of the submerged cable is limited by the water pulley effect ([11]).
3. No external moments act on the submerged cable.

The expression for the balance of angular momentum given in equation (2.2 a) consequently reduces to the following form for static rotational equilibrium:

$$\mathbf{N}' + \hat{\mathbf{t}} \times \mathbf{F} = \mathbf{0} \tag{2.2 b}$$

The Frenet frame consisting of the unit tangent $\hat{\mathbf{t}}$, unit normal $\hat{\mathbf{n}}$ and unit binormal vectors $\hat{\mathbf{b}}$ is oriented with the space curve formed by the neutral axis, $\mathbf{r}(s,t)$ as seen in Figure 2.1. From the principles of differential geometry, the changing orientation of the Frenet frame with the spatial coordinate s, is specified by two parameters, the curvature κ and the torsion γ.

These parameters are defined as:

$$\kappa = (\mathbf{r}'' \cdot \mathbf{r}'')^{1/2}, \gamma = \frac{\mathbf{r}'.(\mathbf{r}'' \times \mathbf{r}''')}{\mathbf{r}'' \cdot \mathbf{r}''} \tag{2.3}$$

The Frenet frame base vectors are defined as:

$$\hat{\mathbf{t}} = \mathbf{r}', \hat{\mathbf{n}} = \frac{\mathbf{r}''}{\kappa} \text{ and } \hat{\mathbf{b}} = \frac{\mathbf{r}' \times \mathbf{r}''}{\kappa^2} \tag{2.4}$$

The constitutive relation for the cable given by Love [18] yields the following relation for the internal couple $\mathbf{N}$:

$$\mathbf{N} = EI\kappa\hat{\mathbf{b}} + GJ\tau\hat{\mathbf{t}} \tag{2.5}$$

where E is the Young's modulus, I is the area moment of inertia, G is the shear modulus, J is the polar moment of inertia of the cable cross-section about the local tangent and τ is the overall twist of the cross section which consists of two parts. The first part is the torsion of the Frenet frame γ which is a geometric twist created as the neutral axis of the cable curves through space. The local frame $(\hat{\mathbf{t}}, \hat{\mathbf{p}}_1, \hat{\mathbf{p}}_2)$ is located relative to the Frenet frame $(\hat{\mathbf{t}}, \hat{\mathbf{n}}, \hat{\mathbf{b}})$ by an angular deformation α as shown in Figure 2.2. The second part of the tether twist is the spatial rate of change of the torsional deformation α about the local tangent. This is produced by external torsional couples applied at the cable boundaries. The total twist per unit length is given by Love's ordinary approximation theorem [18] as:

$$\tau = \gamma + \alpha' \tag{2.6}$$

Substituting for the internal couple $\mathbf{N}$ from equation (2.2 a) using equations (2.3) to (2.6), the expression for the internal force $\mathbf{F}$ is obtained as:

$$\mathbf{F}(s,t) = -(EI\mathbf{r}'')' + \left[\left((T+P) - EI\kappa^2\right)\mathbf{r}'\right] + \left[GJ\tau\left(\mathbf{r}' \times \mathbf{r}''\right)\right] \tag{2.7 a}$$

This expression for the internal force substituted into the expression for balance of linear momentum of equation (2.1 a) gives:

$$-(EI\mathbf{r}'')'' + [(T - EI\kappa^2)\mathbf{r}']' + [GJ\tau(\mathbf{r}' \times \mathbf{r}'')]' + \mathbf{q} = \left(\frac{1}{4}\pi d_c^{\,2}\rho_c \mathbf{I}\right)\ddot{\mathbf{r}} \qquad (2.7\text{ b})$$

In the equations (2.7 a) and (2.7 b), $\mathbf{I}$ is the 3×3 identity matrix and T is the internal axial force, defined using the constitutive relationship:

$$T = EA\varepsilon + C_{ID}\dot{\varepsilon}\,,\ \varepsilon = \frac{1}{2}\left[(r'\cdot r')^{1/2} - 1\right] \qquad (2.8)$$

Here, ε is the strain, and C_{ID} is the internal viscous damping coefficient, representing the frictional dissipation of energy within the tether. For the submerged cable, the applied force vector $\mathbf{q}$ is the resultant of the distributed hydrodynamic, buoyancy and applied forces.

The balance of angular momentum given by the vector equation (2.2 b) projected along the tangent direction $\hat{\mathbf{t}}$, along with the constitutive relation from equation (2.5), produces the following equilibrium equation governing the torsional mechanics of the cable.

$$(GJ\tau)' = 0 \qquad (2.9)$$

Equations (2.7 b) and (2.9) together define the motion of the underwater tether.

2.2.2 Finite Element Discretization

The governing motion equations given by (2.7 b) and (2.9) are continuous differential equations in s and t. As seen in equations (2.3) to (2.9), these differential equations incorporate terms that are highly nonlinear and, as such, are intractable to analytical

solution. It is necessary to reduce these continuous or infinite dimensional equations to discrete or finite dimensional form using a suitable technique. The equations are to be discretized in space, and then integrated in time in order to obtain the solution. A finite dimensional spatial model is obtained by the application of the Galerkin Weighted Residual Method, a Finite Element technique which is described briefly in this section.

I Translational Dynamics

Equation (2.7 b) may be written for a differential element of cable in the compact form, in terms of functions of the arc length s and time t as:

$$\frac{d\mathbf{F}(s,t)}{ds} = \mathbf{G}(s,t) \tag{2.10}$$

In the above, $\mathbf{F}(s,t)$ represents the internal bending, torsional and axial forces:

$$\mathbf{F}(s,t) = -(EI\mathbf{r}'')' + \left[\left((T+P) - EI\kappa^2\right)\mathbf{r}'\right] + \left[GJ\tau\left(\mathbf{r}' \times \mathbf{r}''\right)\right] \tag{2.11}$$

$\mathbf{G}(s,t)$ is the resultant of the distributed external force ($\mathbf{q}$) and the inertial force and is given by:

$$\mathbf{G}(s,t) = \left(\frac{1}{4}\pi d^2 \rho_c\right)\ddot{\mathbf{r}} - \mathbf{q} \tag{2.12}$$

The solution of equation (2.10) is a vector function $\mathbf{r}(s,t)$ defined over the tether span s and the time domain of the simulation. In the spatially discrete model sought, the continuous span of the cable is reduced to a concatenation of N elements, where each of the $i = 1,2,\ldots,N$ element dynamics is governed by N instances of equations having the form of equation (2.10). The first step in the Weighted Residual technique is the

formulation of the trial solution. The trial solution for the continuous position vector over the span of the i^{th} element, $\mathbf{r}_i(s)$, is represented in the form:

$$\mathbf{r}_i(s,t) = \sum_{j=1}^{n+1} \nu_{i,j}(t)\phi_{i,j}(s) \tag{2.13 a}$$

This expression is defined over the spatial domain $s \in (s^{(i-1)}, s^{(i)})$. $\nu_{i,j}$ are time-varying generalized displacements, $\phi_{i,j}$ are shape functions or interpolation functions that define the spatial variation of the generalized displacement over the domain of the element and n is the geometric order of the trial solution. Following Buckham et al [11], the tether element is modeled to have a cubic spline profile, corresponding to which, the parameters in equation (2.13 a) are:

$$\nu_{i,1} = \mathbf{r}^{(i-1)} \qquad \phi_{i,1} = \frac{s^{(i)} - s}{L_i}$$

$$\nu_{i,2} = \mathbf{r}''^{(i-1)} \qquad \phi_{i,2} = \frac{1}{6}\left(\phi_{i,1}{}^3 - \phi_{i,1}\right)L_i{}^2$$

$$\nu_{i,3} = \mathbf{r}^{(i)} \qquad \phi_{i,3} = \frac{s - s^{(i-1)}}{L_i}$$

$$\nu_{i,4} = \mathbf{r}''^{(i)} \qquad \phi_{i,4} = \frac{1}{6}\left(\phi_{i,3}{}^3 - \phi_{i,3}\right)L_i{}^2 \tag{2.13 b}$$

Where $L_i = s^{(i)} - s^{(i-1)}$ is the undeformed or nominal element length. The next step is to define the residual. The residual of the differential equation (2.10) is defined as:

$$\mathbf{R}(s,t) = \frac{d\mathbf{F}(s,t)}{ds} - \mathbf{G}(s,t) \tag{2.14}$$

Whereas the value of the residual for the actual continuous differential equation (2.10) is exactly zero, the approximate weighted residual solution seeks to make only the weighted average of the residual over the spatial domain of the element defined by $s \in (s^{(i-1)}, s^{(i)})$ to be zero. So, the equation (2.10) cast in the approximate weighted residual form is:

$$\int_{s^{(i-1)}}^{s^{(i)}} \mathbf{R}_i(s,t)\beta_{i,j}(s)ds = \mathbf{0} \tag{2.15}$$

$\mathbf{R}_i$ is the residual defined over the ith differential element. $\beta_{i,j}$ for $j = 1, 2, \ldots, n$ are the n weighting functions.

There exist a number of different ways to select the weighting functions. Each manner of selection corresponds to a different Weighted Residual Finite Element technique. Here, we consider the Bubnov-Galerkin Weighted Residual technique, where the weighting functions are taken to be the same as the shape functions of the trial solution, i.e.

$$\beta_{i,j} = \phi_{i,j} \tag{2.16}$$

Where $\phi_{i,j}$ $j = 1, 2, 3, 4$ are the four shape functions defined in equation (2.13 b).

From equations (2.14) ,(2.15), and (2.16)

$$\int_{s^{(i-1)}}^{s^{(i)}} \frac{d\mathbf{F}_i(s,t)}{ds}\phi_{i,j}(s)ds - \int_{s^{(i-1)}}^{s^{(i)}} \mathbf{G}_i(s,t)\phi_{i,j}(s)ds = \mathbf{0} \tag{2.17}$$

The highest spatial derivative on the left hand side of (2.17) is integrated by parts to give a boundary term and a term involving the derivative of the shape function:

$$\int_{s^{(i-1)}}^{s^{(i)}} \frac{d\mathbf{F}_i(s,t)}{ds}\phi_{i,j}(s)ds = \left[\mathbf{F}_i(s,t)\phi_{i,j}(s)\right]_{s^{(i-1)}}^{s^{(i)}} - \int_{s^{(i-1)}}^{s^{(i)}} \mathbf{F}_i(s,t)\frac{d\phi_{i,j}(s)}{ds}ds \tag{2.18}$$

From equations (2.17) and (2.18) we get

$$\left[\mathbf{F}_i(s,t)\phi_{i,j}(s)\right]_{s^{(i-1)}}^{s^{(i)}} - \int_{s^{(i-1)}}^{s^{(i)}} \mathbf{F}_i(s,t)\frac{d\phi_{i,j}(s)}{ds}ds - \int_{s^{(i-1)}}^{s^{(i)}} \mathbf{G}_i(s,t)\phi_{i,j}(s)ds = \mathbf{0} \tag{2.19}$$

The final step is to carry out the above integration operations over the spatial domain to obtain the spatially discrete form of the governing equation (2.7 b). The 12 scalar residual equations for the balance of linear momentum are obtained as:

$$\begin{aligned}&\int_{s^{(i-1)}}^{s^{(i)}} \left(\left(-EI\mathbf{r}_i''' + \left[\left((T+P)-EI\kappa^2\right)_i \mathbf{r}_i'\right] + \left[GJ\tau_i\left(\mathbf{r}_i'\times\mathbf{r}_i''\right)\right]\right)\phi_{i,j}{}' + \left(\mathbf{q}_i - \left(\frac{1}{4}\pi d^2\rho_c\right)\ddot{\mathbf{r}}_i\right)\phi_{i,j}\right)ds = \\ &\left[\left(-EI\mathbf{r}_i''' + \left[\left((T+P)-EI\kappa^2\right)_i \mathbf{r}_i'\right] + \left[GJ\tau_i\left(\mathbf{r}_i'\times\mathbf{r}_i''\right)\right]\right)\phi_{i,j}\right]_{s^{(i-1)}}^{s^{(i)}} \quad j=1,2,3,4\end{aligned} \tag{2.20}$$

Using equation (2.11), the boundary term in equation (2.20) evaluates to:

$$\left[\left(-EI\mathbf{r}_i''' + \left[\left((T+P)-EI\kappa^2\right)_i \mathbf{r}_i'\right] + \left[GJ\tau_i\left(\mathbf{r}_i'\times\mathbf{r}_i''\right)\right]\right)\phi_{i,j}\right]_{s^{(i-1)}}^{s^{(i)}} = \left[(-F_i)\phi_{i,j}\right]_{s^{(i-1)}}^{s^{(i)}} \tag{2.21}$$

The above integrals were evaluated by Buckham et al [11]. The form of the residual in equation (2.20) for the i^{th} cable element was obtained as:

$$\left(\left[\mathbf{K}_B\right]_i + \left[\mathbf{K}_A\right]_i + \left[\mathbf{K}_T\right]_i\right)\left\{\mathbf{r}^{(i-1)T}\ \mathbf{r}''^{(i-1)T}\ \mathbf{r}^{(i)T}\ \mathbf{r}''^{(i)T}\right\}^T + \mathbf{H}_i + \mathbf{W}_i + \mathbf{B}_i = \mathbf{M}_i\ddot{\mathbf{R}}_i \tag{2.22}$$

where $\mathbf{R}_i = \left\{\ddot{\mathbf{r}}^{(i-1)T}\ \ddot{\mathbf{r}}''^{(i-1)T}\ \ddot{\mathbf{r}}^{(i)T}\ \ddot{\mathbf{r}}''^{(i)T}\right\}^T$. The 12×12 stiffness matrices $\left[\mathbf{K}_A\right]_i$, $\left[\mathbf{K}_B\right]_i$, and $\left[\mathbf{K}_T\right]_i$ represent the internal axial, bending and torsional effects respectively. The 12×1 nonlinear load vectors $\mathbf{H}_i$, $\mathbf{W}_i$, and $\mathbf{B}_i$ represent the generalized nodal forces due to hydrodynamic, gravitational and applied boundary loads respectively. $\mathbf{M}_i$ is the 12×12

mass matrix which includes the true and added mass terms as detailed in Buckham et al [11].

II Torsional Mechanics

Applying the Finite Element technique to the twist equilibrium given by equation (2.9), 2 scalar residual equations are obtained as:

$$GJ \int_{s^{(i-1)}}^{s^{(i)}} (\gamma_i + \alpha_i')\phi_{i,j}' ds = [GJ\tau_i]\phi_{i,j}\Big|_{s^{(i-1)}}^{s^{(i)}} \quad j = 1,2,3,4 \tag{2.23}$$

Following a similar procedure as for the translational dynamics, the residual equation for torsional equilibrium of the i^{th} element was obtained as:

$$\frac{GJ}{L_i}\begin{bmatrix} 1 & -1 \\ -1 & 1 \end{bmatrix}\begin{Bmatrix} \alpha^{(i-1)} \\ \alpha^{(i)} \end{Bmatrix} = GJ\begin{Bmatrix} \gamma^{(i)} \\ -\gamma^{(i)} \end{Bmatrix} + \begin{Bmatrix} GJ\tau_i^{(i-1)} \\ GJ\tau_i^{(i)} \end{Bmatrix} \tag{2.24}$$

Where the bracketed superscript is the node number and the unbracketed subscript is the element number. $GJ\tau_i^{(i-1)}$ and $GJ\tau_i^{(i)}$ represent the internal restoring torque at the boundaries of the i^{th} element.

2.2.3 Application of first order continuity.

The cubic spline trial function satisfies first order or $C^1(s)$ continuity, resulting in a series of constraint equations applicable to the curvature vectors $\mathbf{r}_i''$, across the node points over the span of the cable for $i = 1,2,\ldots,N$. These equations have the form given in equation (2.25)

$$\begin{bmatrix} \frac{L_1}{3}\mathbf{I} & \frac{L_1}{6}\mathbf{I} & 0 & 0 & 0 \\ \frac{L_1}{6}\mathbf{I} & \frac{L_1+L_2}{3}\mathbf{I} & \frac{L_2}{3}\mathbf{I} & 0 & 0 \\ 0 & \ddots & \ddots & \ddots & 0 \\ 0 & 0 & \frac{L_{N-1}}{3}\mathbf{I} & \frac{L_{N-1}+L_N}{3}\mathbf{I} & \frac{L_N}{6}\mathbf{I} \\ 0 & 0 & 0 & \frac{L_N}{6}\mathbf{I} & \frac{L_N}{3}\mathbf{I} \end{bmatrix} \begin{Bmatrix} \mathbf{r}''^{(0)} \\ \mathbf{r}''^{(1)} \\ \vdots \\ \mathbf{r}''^{(N-1)} \\ \mathbf{r}''^{(N)} \end{Bmatrix} =$$

$$\begin{Bmatrix} \frac{\mathbf{r}^{(1)}-\mathbf{r}^{(0)}}{L_1} \\ \frac{\mathbf{r}^{(2)}-\mathbf{r}^{(1)}}{L_2} - \frac{\mathbf{r}^{(1)}-\mathbf{r}^{(0)}}{L_1} \\ \vdots \\ \frac{\mathbf{r}^{(N)}-\mathbf{r}^{(N-1)}}{L_N} - \frac{\mathbf{r}^{(N-1)}-\mathbf{r}^{(N-2)}}{L_{N-1}} \\ \frac{\mathbf{r}^{(N)}-\mathbf{r}^{(N-1)}}{L_N} \end{Bmatrix} + \begin{Bmatrix} -\mathbf{r}'^{(0)} \\ 0 \\ \vdots \\ 0 \\ \mathbf{r}'^{(N)} \end{Bmatrix} \tag{2.25}$$

Given the positions of the nodes, and the tangent vectors (and hence the first spatial derivatives of the position vectors from equation (2.4)), at the top and bottom boundaries of the cable, the vector of curvatures can be obtained from the constraint equation (2.25). Hence it is seen that as a consequence of selecting the cubic spline element as the trial function for the Finite Element solution, the state of the cable is completely defined by only the positions and the velocities of the node points. This results in a computationally efficient technique, needing only 6 state variables per element, relative to other finite element formulations like those of O'Brien and McNamara [19] which need 12 or 13 state variables per element.

2.2.4 Reduction by the Lumped Mass Assumption

In equation (2.22) the inertial terms on the right hand side are given by:

$$\mathbf{M}_i\ddot{\mathbf{R}}_i = \begin{bmatrix} \frac{1}{3}\mathbf{M}_i & \frac{-1}{45}L_i^2\mathbf{M}_i & \frac{1}{6}\mathbf{M}_i & \frac{-7}{360}L_i^2\mathbf{M}_i \\ & \frac{2}{945}L_i^4\mathbf{M}_i & \frac{-7}{360}L_i^2\mathbf{M}_i & \frac{31}{15120}L_i^4\mathbf{M}_i \\ & & \frac{1}{3}\mathbf{M}_i & \frac{-1}{45}L_i^2\mathbf{M}_i \\ \text{SYM} & & & \frac{2}{945}L_i^4\mathbf{M}_i \end{bmatrix} \begin{Bmatrix} \ddot{\mathbf{r}}^{(i-1)} \\ \ddot{\mathbf{r}}'^{(i-1)} \\ \ddot{\mathbf{r}}^{(i)} \\ \ddot{\mathbf{r}}'^{(i)} \end{Bmatrix} \tag{2.26}$$

The mass matrix above is a consistent matrix. The inertial term depends on the second time derivatives of curvatures $\ddot{\mathbf{r}}'^{(i-1)}$ and $\ddot{\mathbf{r}}'^{(i)}$. The variation of the element shape is composed of two parts: a linear interpolation of the node positions and a cubic refinement that is superposed over this line. The second time derivative of curvature in equation (2.26) represents motion of the element between the nodes. Employing the lumped mass approximation of Buckham et al [11], there is no mass associated with these points and hence they do not contribute to the inertial terms of the right hand side of equation (2.22). The first step in applying the lumped mass approximation is the reduction of the system by pre-multiplying both sides of equation (2.22) by the matrix $\mathbf{P}_i$:

$$\mathbf{P}_i = \begin{bmatrix} \mathbf{I} & \frac{1}{L_i^2}\mathbf{I} & \mathbf{0} & \mathbf{0} \\ \mathbf{0} & \mathbf{0} & \mathbf{I} & \frac{1}{L_i^2}\mathbf{I} \end{bmatrix} \tag{2.27}$$

As a result, the inertial term on the right hand side of equation (2.22) can be partitioned as:

$$\boldsymbol{P}_i\boldsymbol{M}_i\ddot{\boldsymbol{R}}_i = L_i\begin{bmatrix}\mathbf{M}_i & \mathbf{0}\\ \mathbf{0} & \mathbf{M}_i\end{bmatrix}\left(\begin{bmatrix}\frac{14}{45}\mathbf{I} & \frac{53}{360}\mathbf{I}\\ \frac{53}{360}\mathbf{I} & \frac{14}{45}\mathbf{I}\end{bmatrix}\begin{Bmatrix}\ddot{\boldsymbol{r}}^{(i-1)}\\ \ddot{\boldsymbol{r}}^{(i)}\end{Bmatrix} - L_i^2\begin{bmatrix}\frac{19}{945}\mathbf{I} & \frac{263}{15120}\mathbf{I}\\ \frac{263}{15120}\mathbf{I} & \frac{19}{945}\mathbf{I}\end{bmatrix}\begin{Bmatrix}\ddot{\boldsymbol{r}}'^{(i-1)}\\ \ddot{\boldsymbol{r}}'^{(i)}\end{Bmatrix}\right) \quad (2.28)$$

Following the lumped mass assumption, the matrix on the right hand side associated with the higher time derivative of curvature is neglected. The final form of the translational dynamics equation for the i^{th} element presented by Buckham et al [11] is shown in equation (2.29). The Mass matrix on the right hand side has been reduced to diagonal form from the original consistent form of equation (2.26).

$$\mathbf{P}_i\left(\left(\left[\mathbf{K}_B\right]_i+\left[\mathbf{K}_A\right]_i+\left[\mathbf{K}_T\right]_i\right)\left\{\mathbf{r}^{(i-1)T}\ \mathbf{r}'^{(i-1)T}\ \mathbf{r}^{(i)T}\ \mathbf{r}'^{(i)T}\right\}^T+\mathbf{H}_i+\mathbf{W}_i+\mathbf{B}_i\right) = L_i\begin{bmatrix}\frac{1}{2}\mathbf{M}_i & \mathbf{0}\\ \mathbf{0} & \frac{1}{2}\mathbf{M}_i\end{bmatrix}\begin{Bmatrix}\ddot{\mathbf{r}}^{(i-1)}\\ \ddot{\mathbf{r}}^{(i)}\end{Bmatrix} \quad (2.29)$$

2.2.5 Spatially Discrete Dynamics Equations.

Finally, the element equations for the individual elements are assembled to obtain the global spatially discrete motion equations for the tether. The assembled equations for the translational dynamics of the tether are given in equation (2.30) below:

$$\left(\left[\mathbf{K}_B\right]_G+\left[\mathbf{K}_A\right]_G+\left[\mathbf{K}_T\right]_G\right)\left\{\mathbf{r}^{(0)T}\ \mathbf{r}'^{(0)T}\ \mathbf{r}^{(1)T}\ \mathbf{r}'^{(1)T}\ \cdots\ \mathbf{r}'^{(N)T}\right\}^T+\mathbf{H}_G+\mathbf{W}_G+\mathbf{B}_G=\mathbf{M}_G\ddot{\mathbf{R}} \quad (2.30)$$

where $\mathbf{R} = \left\{\mathbf{r}^{(0)T} \;\; \mathbf{r}^{(1)T} \;\; \cdots \;\; \mathbf{r}^{(N)T}\right\}^T$. The $3(N+1)\times 6(N+1)$ stiffness matrices $\left[\mathbf{K}_B\right]_G$, $\left[\mathbf{K}_A\right]_G$, and $\left[\mathbf{K}_T\right]_G$ represent the internal bending, axial and torsional effects respectively. The $3(N+1)\times 1$ nonlinear load vectors $\mathbf{H}_G$, $\mathbf{W}_G$, and $\mathbf{B}_G$ represent the generalized nodal forces due to hydrodynamic, gravitational and applied boundary loads. $\mathbf{M}_G$ is the $3(N+1)\times 3(N+1)$ lumped mass matrix including the true and added mass terms. The parenthesized superscripts indicate the node number and the subscript $_G$ indicates a global entity created in the assembly step.

The torsional dynamics of the tether are given by:

$$GJ\left[\mathbf{L}\right]_G \boldsymbol{\alpha}_G = GJ\left\{\Delta\boldsymbol{\gamma}_G\right\} + \left\{\mathrm{T}^{(0)} \;\; 0 \;\; \cdots \;\; 0 \;\; \mathrm{T}^{(N)}\right\}^T \tag{2.31}$$

Where $\left[\mathbf{L}\right]_G$ is a tridiagonal matrix with entries based on the nominal element lengths, $\boldsymbol{\alpha}_G = \left\{\alpha^{(0)} \;\; \alpha^{(1)} \;\; \cdots \;\; \alpha^{(N)}\right\}^T$ is the vector of torsional deformations at the node points, and $\Delta\boldsymbol{\gamma}_G = \left\{\Delta\gamma_1 \;\; \Delta\gamma_2 \;\; \cdots \;\; \Delta\gamma_N\right\}^T$ where $\Delta\gamma_i = \gamma_i - \gamma_{i-1}$ and γ_i is the average torsion for the i^{th} element.

The assembled equations in (2.30) and (2.31) represent the general nonlinear initial value problem of the form:

$$\mathbf{F}(t, \mathbf{R}, \dot{\mathbf{R}}) = \mathbf{M}_G \ddot{\mathbf{R}} \tag{2.32}$$

Time domain simulation of the cable dynamics is obtained by propagating equation (2.32) above in time through the use of a suitable temporal integration algorithm.

2.3 Closure

In this Chapter, the dynamics equations for fixed length underwater vehicle tether were formulated from first principles. The Galerkin Weighted Residual Finite Element technique, used with a cubic spline shape function for the elements, was shown to produce the spatially discrete form of the governing dynamics equations. The higher order shape function captures the flexural and torsional effects which are dominant in the dynamics of low tension tether. The formulation is applicable to all levels of cable tension and is computationally efficient, needing only 6 state variables, the positions and velocities of the nodes, to fully describe the state of the cable. In the next chapter, the fixed length model shown here is extended to model varying length of cable.

Chapter 3
Dynamics Model for Variable Length ROV Tether

3.1 Overview

In this chapter the fixed length cable model is augmented with a variable length calculation. In an ROV system, the umbilical linked to the vehicle is wound around a winch. The winch platform is mounted on the deployer ship. The winding or unwinding of tether around the rotating winch results in retrieval or deployment of the vehicle.

The fixed length tether dynamics model described in the previous chapter treats the ship as a prescribed kinematic boundary condition at the top end of the tether. In the spatially discrete tether model, the topmost or 0^{th} node of the cable assembly is constrained to move as the deployer vessel. In keeping with the fixed length model, the ship motion is maintained as a kinematic constraint at the top end of the cable in the variable length tether dynamics modeling considered in this Chapter. The entire span of the tether is a long, spatially distributed system, part of which is on the winch and part of which is deployed in the water. The winch acts as the source of mass flux for the portion of tether presently in the water. The portion of the tether on the winch is constrained by the prescribed kinematic top boundary condition of ship motion. It is the deployed segment, with time varying length (and mass) that is of interest. Consequently, the

dynamics are formulated and evaluated only for the segment of tether in the water. In this chapter the following questions are addressed:

1. How does time-varying length (and hence mass) of the submerged ROV tether change the governing tether dynamics equations of Chapter 2?
2. How are the additional dynamics terms discretized for application in the new spatially discrete model?

One of the most commonly encountered and widely studied variable mass systems is the rocket, ejecting propellant during flight. This is used as the starting point in Section 3.2 for the development of the dynamics equations of variable mass systems. Next, in Section 3.3, Tiersten's momentum flux formulation [12] leading to Newton's Second Law of motion for variable mass systems is presented as a generalization of the rocket equation. In Section 3.4, the Lagrangian and Eulerian approaches to modeling variable length tether dynamics are presented. It is shown that the approach of Burgess [9] corresponds to the Lagrangian approach. The Eulerian approach is shown to be analogous to Newton's Second Law for variable mass systems as given by Tiersten [12]. Next, in Section 3.5 a case study for the dynamics modeling of a translating cable is presented, and the utility of the momentum flux formulation in correctly modeling the dynamics of the control volume is brought out. The results of the case study coupled with the ability to model low tension cable dynamics are the reasons for the selection of the Eulerian approach to model the dynamics of variable length tether in this work. The governing translational dynamics equations of the fixed length cable element in Chapter 2 are augmented with the new variable length terms in Section 3.6. In Section 3.7 Galerkin's Weighted Residual technique is applied to the governing equation for the differential

element to obtain the spatially discrete governing dynamics for a variable length element. The final assembly of the spatially discrete cable consisting of fixed and variable length elements is presented.

3.2 The Rocket Equation.

The formulation of the dynamics equation for a rocket dates back to the work of the Russian futurist Ivan Vsevolodovich Meshchersky in 1897 [21]. Consider a rocket with mass m and velocity $\mathbf{v}$ relative to the inertial frame at time t. At time $t+\Delta t$ a quantum of matter $\Delta\mu$ is ejected out as burnt fuel, with velocity $-\mathbf{v}_e$ relative to the rocket, while the velocity of the remaining mass of the rocket $(m-\Delta\mu)$ increases to $\mathbf{v}+\Delta\mathbf{v}$. At the instant $t+\Delta t$, the mass $\Delta\mu$ has a velocity $\mathbf{v}+\Delta\mathbf{v}-\mathbf{v}_e$ relative to the ground, as shown in Fig. 3.1.

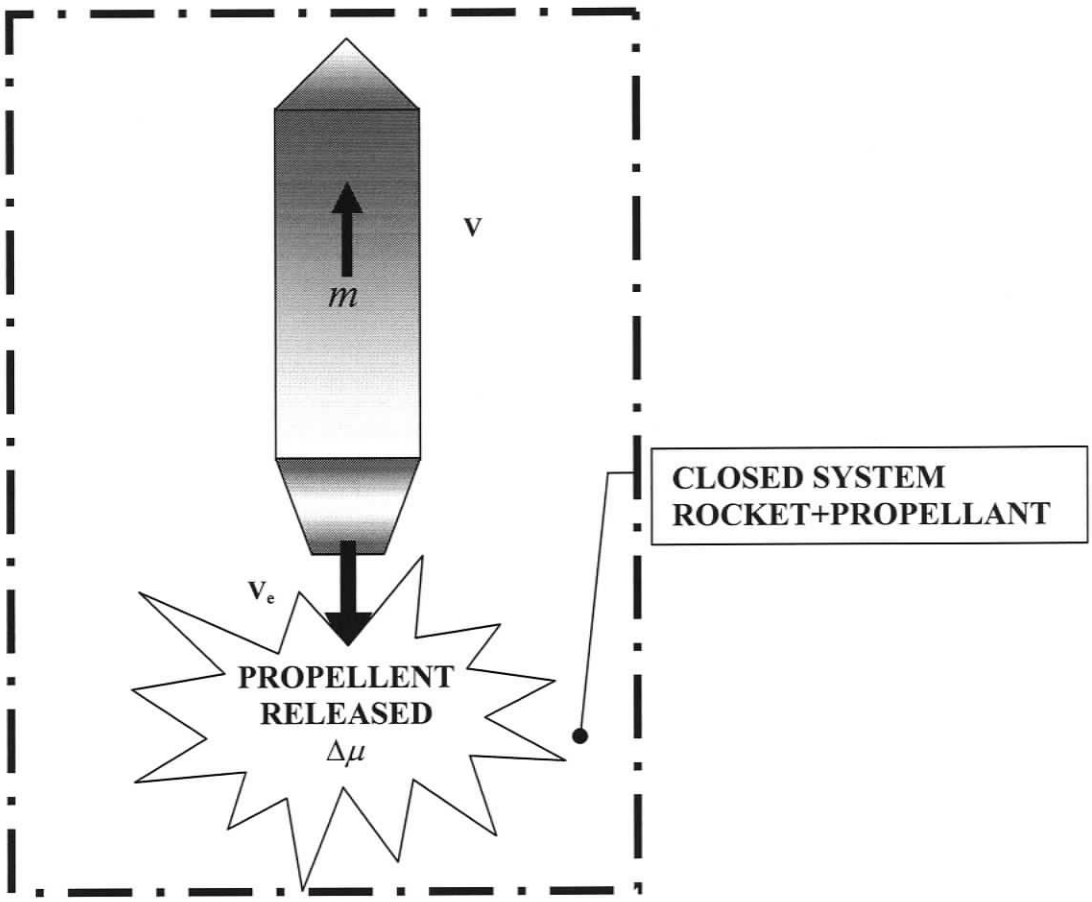

Figure 3.1: Variable Mass Rocket, with the dashed line representing the boundary of the closed system.

Consider the closed system incorporating the rocket and the lost propellant mass. The momentum of the total system before mass ejection is:

$$\mathbf{p}(t) = m\mathbf{v} \tag{3.1}$$

The momentum after mass ejection is:

$$\mathbf{p}(t+\Delta t) = (m-\Delta\mu)(\mathbf{v}+\Delta\mathbf{v}) + \Delta\mu(\mathbf{v}+\Delta\mathbf{v}-\mathbf{v}_e) \tag{3.2}$$

Let $\mathbf{F}^{ext}$ be the external forces acting on the system during the period of mass loss Δt. From Newton's second law of motion:

$$\frac{1}{\Delta t}\left(\mathbf{p}(t+\Delta t)-\mathbf{p}(t)\right)=\mathbf{F}^{\text{ext}} \tag{3.3}$$

(2.3)

From equations (3.1), (3.2), and (3.3)

$$\frac{1}{\Delta t}\left(m\Delta\mathbf{v}-\mathbf{v}_e\Delta\mu\right)=\mathbf{F}^{\text{ext}} \tag{3.4}$$

In the limit $\Delta t \to 0$, the above equation reduces to

$$m\frac{d\mathbf{v}}{dt}-\mathbf{v}_e\frac{d\mu}{dt}=\mathbf{F}^{\text{ext}} \tag{3.5}$$

Equation (3.5) was derived considering an amalgamation of two systems: the rocket, and the exhaust gasses. The mass of the total system, the rocket and the ejected fuel, is given by:

$$M=m+\mu \tag{3.6}$$

This does not change in time (since mass is merely interchanged between the two subsystems of the closed volume). As a result,

$$\frac{dM}{dt}=\frac{dm}{dt}+\frac{d\mu}{dt}=0 \tag{3.7}$$

So,

$$\frac{dm}{dt}=-\frac{d\mu}{dt} \tag{3.8}$$

Focusing on the rocket as the primary system, equations (3.5) and (3.8) yield:

$$m\frac{d\mathbf{v}}{dt}=\mathbf{F}^{\text{ext}}-\mathbf{v}_e\frac{dm}{dt} \tag{3.9}$$

Equation (3.9) describes the governing dynamics equation for the variable mass system that is losing mass to the surroundings. The second term on the right hand side is the thrust due to mass flux. The thrust force is proportional to the discharge velocity and the density of the exhaust gasses.

3.3 Momentum flux formulation

The standard rocket equation derived above shows that the governing dynamics for variable mass systems is not of the form $F = ma$. In this Section, a generic modification of Newton's second law of motion is presented, to model the dynamics of variable mass systems. Tiersten [12] presents an approach to modeling the dynamics of variable mass systems when only a finite volume of the system is of interest. This volume is called the control volume. The dynamic effect of influx/outflow of mass is accounted for by augmenting Newton's second law of motion with a new term called the momentum flux.

Consider the system of interest contained within the control volume shown in Figure 3.2. The instantaneous mass of the system is M. An external force $\mathbf{F}^{ext}$ acts on the system. The absolute velocity of the system is $\mathbf{v}$ and absolute acceleration is $\dot{\mathbf{v}}$. The system interacts with its surroundings beyond the control volume boundary by gaining mass at the rate of $\frac{dM}{dt}$. In this work, the control volume may be visualized as containing the cable deployed in the water, and the mass flux represents the cable leaving the ship winch. The material points representing the mass flux move with velocity of $\mathbf{u}$ as shown in Figure 3.2.

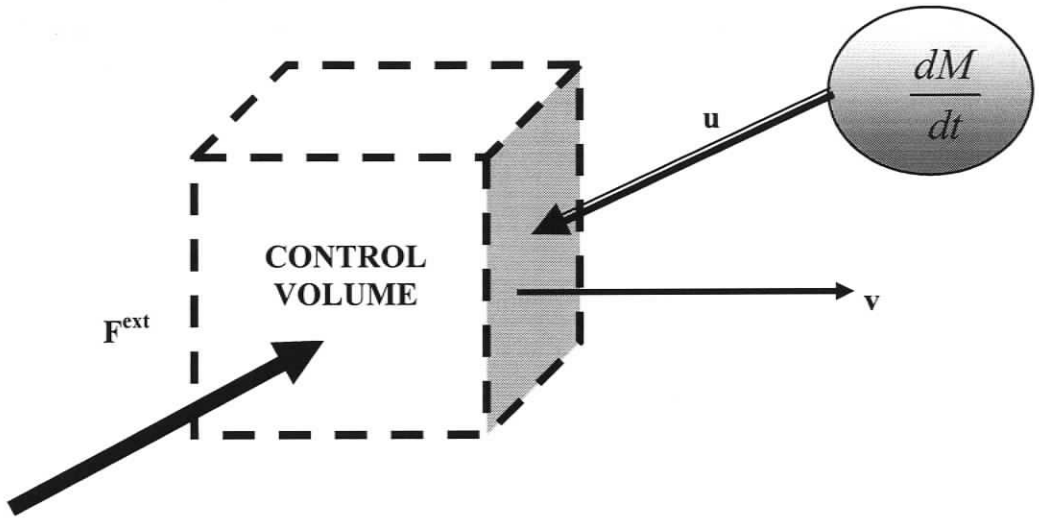

Figure 3.2: Control Volume representation of variable mass system dynamics. Contrary to the rocket problem of Section 3.2, the control volume encompasses only the subsystem that is gaining mass from the surroundings.

Tiersten defines Newton's second law for such a system as:

$$\frac{d(M\mathbf{v})}{dt} = \mathbf{F}^{\text{ext}} + \frac{dM}{dt}\mathbf{u} \tag{3.10 a}$$

This is Newton's second law of motion for fixed mass systems augmented by a momentum flux term, $\frac{dM}{dt}\mathbf{u}$. On expanding equation (3.10 a), an expression analogous to the rocket equation (3.9) is obtained as:

$$M\frac{d\mathbf{v}}{dt} = \mathbf{F}^{\text{ext}} + \frac{dM}{dt}(\mathbf{u} - \mathbf{v}) \tag{3.10 b}$$

Both equations (3.9) and (3.10 b) have the form of the familiar Newton's second law for fixed mass systems, augmented by a term which is the product of rate of mass influx/outflow and the relative velocity of mass gain/loss.

3.4 Lagrangian and Eulerian approaches to modeling variable length cable dynamics

There are two different approaches to model the changing length of the spatially discrete cable. One is to change the length of the elements while keeping the number of elements fixed. The second is to change the number of elements in the cable assembly while keeping the length of each element constant. In the literature on variable length underwater cables, the former approach has been adopted by Kamman and Huston [4] and Bannerjee and Do [5] while the latter has been used by Burgess [9]. Within the existing literature, there has been little or no justification for the use of either approach. In this Section, the foundations of the two approaches, in terms of classical mechanics principles, is clarified. It is shown that the two existing approaches can be developed from the Eulerian and Lagrangian frameworks for dynamics modeling. First the definitions of the Eulerian and Lagrangian approaches are reviewed by invoking some fundamental results from fluid mechanics and then their utility in variable length cable dynamics modeling is investigated.

3.4.1 Fluid Mechanics Definitions of the Eulerian and Lagrangian Approaches

One of the key aspects of a fluid, in contrast to a solid, is the ability to redistribute its particles in space. However, the system of interest is restricted to a finite space. The finite

volume of space through which the transport process occurs is referred to as the control volume, as described for the momentum flux formulation of Section 3.3. The rest of the universe is called the surrounding. Mass, energy and momentum balance expressions are applied to material particles traversing the control volume. This approach is synergistic with our treatment of the deployed span of the cable as the main system or control volume and the cable on the deployer as the surrounding. Next, an important question needs to be answered when describing the properties of the fluid. Are these properties attributed to a fixed element of fluid, or at a fixed point in space? Since the elements of a fluid could possibly move around from point to point, these two views will differ. The two views are:

Eulerian: here changes are described as they occur at a fixed point in the fluid.

Lagrangian: here changes are described, following a fluid particle along its trajectory.

From the above it is hypothesized that using the Lagrangian approach, the variable length (and mass) of the cable would be modeled by taking mass flow to occur throughout the cable span. In the Eulerian approach however the mass increase or decrease is restricted to the discrete cable element at the interface of the cable assembly and the source of mass flux (most commonly the winch on the deployer). This element is called the boundary element or thrust element. Next, the implications of adopting either approach, on the formulation for variable length cable dynamics is examined.

3.4.2 Lagrangian approach

In the Lagrangian approach, every differential segment of the tether serves as a conduit for the mass flow. There is no "accumulation" of mass at a particular point. Consider a segment of the cable shown in Figure 3.3.

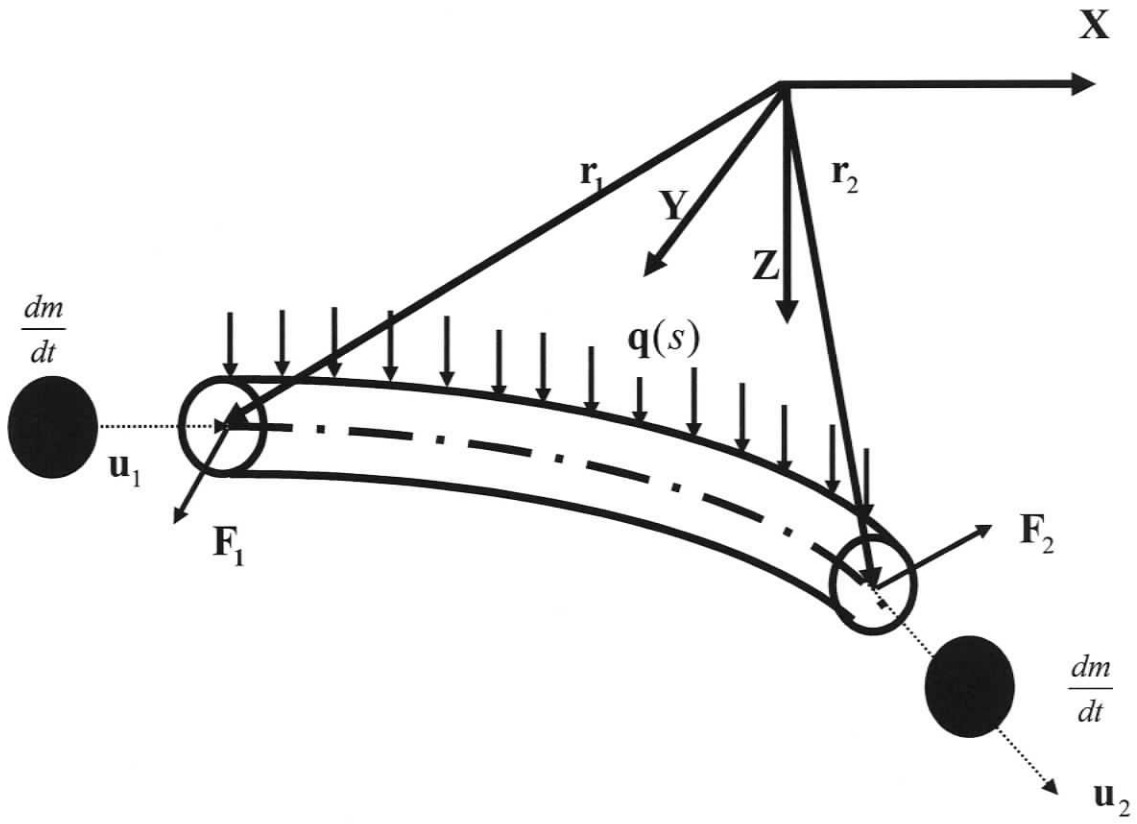

Figure 3.3: Free Body Diagram for mass flux through the cable in the Lagrangian formulation. Material particles (shown as darkened ovals) enter at point 1 with absolute velocity $\mathbf{u}_1$ and leave at point 2 with absolute velocity $\mathbf{u}_2$ along the respective local tangents.

The cable segment is bounded by points 1 and 2, defined in space by the curvilinear coordinates s_1 and s_2 as shown. In the free body diagram of this segment, the internal forces at the points 1 and 2 are given by $\mathbf{F}_1$ and $\mathbf{F}_2$ respectively. The external distributed

force is given by $\mathbf{q}(s)$ and is the resultant of the hydrodynamic force $\mathbf{h}$, and buoyancy force $\mathbf{w}$. The positions and velocities of points 1 and 2 are state variables and given by $\mathbf{r}_1, \mathbf{r}_2$ and $\dot{\mathbf{r}}_1, \dot{\mathbf{r}}_2$ respectively in the inertial **(XYZ)** coordinate system as shown. Mass enters at point 1, and leaves the cable segment at point 2, at the rate of $\frac{dm}{dt}$, along the local tangents as shown. The material particles associated with the mass flux have absolute velocity of $\mathbf{u}$ directed along the local tangent. The magnitude of $\mathbf{u}$ is prescribed by the rate of deployment or retrieval of the cable. Consequently, the mass flux is given by:

$$\frac{dm}{dt} = \lambda u \tag{3.11}$$

where λ is the mass per unit length (or linear density) of the cable.

In the Lagrangian formulation, the total mass of the cable segment remains constant. The net momentum flux is hypothesized to be the sum of two distinct contributions. One is the effect of the changing momentum of a point on the cable due its changing mass. Considering the point 1, this momentum change corresponding to the changing mass would be given by $\frac{dm}{dt}\dot{\mathbf{r}}_1$. The other part of the net momentum flux is the effect of the new material particles moving in with a velocity $\mathbf{u}_1$ at the point 1. This contribution to the momentum change is given by $\frac{dm}{dt}\mathbf{u}_1$. The net rate of change of momentum due to mass flux would be given by the sum of both these effects.

For this case, following the work of Tabbarok et al [20], the balance of linear momentum can be written as:

$$\frac{d}{dt}\int_{s_1}^{s_2}\lambda\dot{\mathbf{r}}\,ds = \mathbf{F}_2 - \mathbf{F}_1 + \int_{s_1}^{s_2}\mathbf{q}(s)\,ds + \frac{dm}{dt}\dot{\mathbf{r}}_1 + \frac{dm}{dt}\mathbf{u}_1 - \frac{dm}{dt}\dot{\mathbf{r}}_2 - \frac{dm}{dt}\mathbf{u}_2 \tag{3.12}$$

In the equation (3.12) the last four terms on the right hand side represent the rate of change of momentum as the mass flows through the cable, as explained previously. The equation (3.12) can be written in the equilibrium form as:

$$\int_{s_1}^{s_2}\left(\frac{d(\lambda\dot{\mathbf{r}})}{dt} + \frac{dm}{dt}\frac{d\dot{\mathbf{r}}}{ds} + \frac{dm}{dt}\frac{d\mathbf{u}}{ds} - \frac{d\mathbf{F}}{ds} - \mathbf{q}(s)\right)ds = 0 \tag{3.13}$$

For an arbitrary integration interval between s_1 and s_2 the equation (3.13) above holds only if the integrand is identically zero. Hence, the balance of linear momentum is obtained for a differential element of length ds as;

$$\frac{d(\lambda\dot{\mathbf{r}})}{dt} + \frac{dm}{dt}\frac{d\dot{\mathbf{r}}}{ds} + \frac{dm}{dt}\frac{d\mathbf{u}}{ds} - \frac{d\mathbf{F}}{ds} - \mathbf{q}(s) = 0 \tag{3.14}$$

Now, in equation (3.14) above, the term $\frac{d\mathbf{u}}{ds}$ for a differential element can be taken equal to zero, since magnitude of $\mathbf{u}$ is a constant and is prescribed by the payin/payout speed, and the tangent direction can be taken to be constant over the span of a small differential element. Substituting for $\frac{dm}{dt}$ from equation (3.11) and noting that the mass per unit length of the cable λ is time invariant, equation (3.14) reduces to:

$$\lambda\left(\frac{d\dot{\mathbf{r}}}{dt}+u\frac{d\dot{\mathbf{r}}}{ds}\right)=\frac{d\mathbf{F}}{ds}+\mathbf{q}(s) \tag{3.15}$$

In the left hand side above, it is clear that the rate of change of translational momentum is given by the Material Derivative $\frac{D}{Dt}(\ )=\frac{d}{dt}(\ )+u\frac{d}{ds}(\ )$. This is the Lagrangian formulation for variable length tether dynamics. The Lagrangian approach was used by Burgess [9] in conjunction with a centered in space and centered in time finite difference algorithm. In the spatially discrete computational model of that work, the lengths of all elements were constant, in keeping with the assumption that mass flows in and out of the element in the Lagrangian view. The length change of the cable being deployed or retrieved was modeled by increasing or decreasing the number of computational nodes during the variable length maneuver.

3.4.3 Eulerian approach

In the Eulerian approach, it is hypothesized that the change in mass of the cable occurs only at the interface of the winch and the deployed cable for a differential segment at that location. Referring to the Figure 3.3 above, the mass flux would not be balanced at the two ends of the element. So the tangential mass flux at point 2 would be zero. Considering the differential boundary element in the segment of cable, the expression for balance of linear momentum would be given by:

$$\frac{d(m(t)\dot{\mathbf{r}})}{dt}=\frac{d}{ds}(\mathbf{F})+\mathbf{q}(s)+\frac{dm}{dt}\mathbf{u}_1 \tag{3.16}$$

The following points are noted:

1. The effect of mass flux, in the Eulerian approach exists only at the interface of the segment of cable and source of mass flux. Hence, the momentum flux due to the material particles entering is defined only at the point 1 and is the last term on the right hand side of equation (3.16).
2. The momentum rate change term due to the changing mass of the differential element is embedded within the inertial term on the left hand side of equation (3.16).

Rearranging the terms in equation (3.16), the balance of linear momentum for the boundary element in the Eulerian approach is given by:

$$m(t)\frac{d\dot{\mathbf{r}}}{dt} = \frac{d}{ds}(\mathbf{F}) + \mathbf{q}(s) + \frac{dm}{dt}\left(\mathbf{u}_1 - \dot{\mathbf{r}}\right) \tag{3.17}$$

It is clear that the form of equation (3.17) is analogous to that of Tieresten's general form of the momentum flux equation given in equation (3.10 b). This shows the equivalence between the Eulerian formulation for variable length tether dynamics developed here, and Newton's Second Law of Motion for variable mass systems as given by Tiersten [12].

3.4.4 Choice of Methodology

Having established the significance of the two approaches in variable length cable dynamics modeling, the question arises as to which to adopt in the present work. The key assumption in the Lagrangian approach is that the mass flow occurs at a uniform rate across the entire span of the cable. In the case of a low tension, neutrally buoyant cable with a curved and twisted profile in space, it is not possible to guarantee this condition. It is known from practical experience of the deployment of slack, neutrally buoyant cable,

that in the absence of tension to "suck up" the slack, most of the excess deployed cable would remain close to the deployer. The influence of mass flux would not be experienced at a point far downstream from the deployer. This situation however is synergistic with the Eulerian view whereby the mass change is restricted to the region of the cable close to the deployer. Hence the Eulerian approach appears to be better suited for this work.

3.5 Case Study of a Variable Mass Dynamical System: One-dimensional Translation of a Cable

In this Section, the utility of the momentum flux formulation of Tiersten[12] in modeling the dynamics of a spatially distributed system is demonstrated. When the dynamics of only a finite volume of a spatially distributed system is of interest, this principal part of interest becomes the control volume. The control volume interacts with other parts of the system through momentum interchange, as described in Section 3.3.

Consider a cable, assumed to be rigid, being dragged by a constant force k across a frictionless surface. Only a given volume of space, called the control volume, is considered to be of significance, and is shown in Figure 3.4. The total length of the cable is L. The time varying length of the cable within the control volume is $x(t)$, as shown. The mass per unit length of the cable is λ.

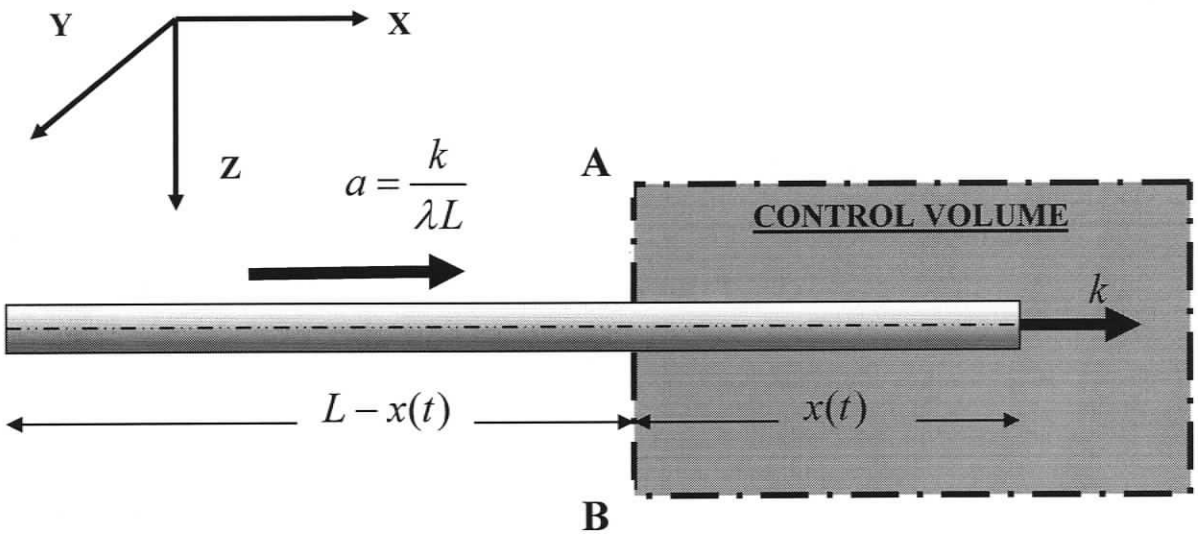

Figure 3.4: Control Volume analysis of a rigid cable being pulled on a frictionless surface. Only a finite volume of the system, shown within the control volume is of interest during the analysis.

The acceleration of every material point of the rigid cable is given by:

$$a = \frac{k}{\lambda L} \tag{3.18}$$

The line AB marks the boundary of the control volume. The region of space to the right of AB is the sub-system of interest.

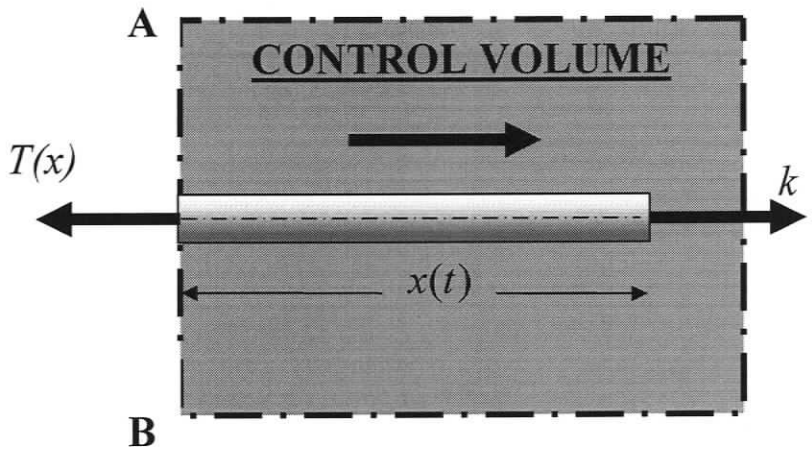

Figure 3.5: Free Body Diagram of control volume interface.

Figure 3.5 above, shows the free body diagram of the cable severed at the control volume boundary. The internal force within the cable given by the tension $T(x)$ at this point. Considering the portion of the cable within the control volume to be a rigid body, the net force acting on it is given by:

$$F = k - T(x) \tag{3.19}$$

3.5.1 Standard Newtonian Analysis

First Newton's second law of motion for fixed mass systems is applied to the problem at hand. Consequently:

$$F = \frac{d(Mv)}{dt} \tag{3.20}$$

So, from equations (3.19) and (3.20), and noting that M includes only the mass within the control volume under consideration:

$$k - T(x) = \frac{d(\lambda x v)}{dt} \tag{3.21}$$

Where v is the velocity of the cable.

Expanding equation (3.21)

$$k - T(x) = \lambda x \dot{v} + \lambda \dot{x} v \tag{3.22}$$

Noting that

$$\dot{x} = v; \quad \ddot{x} = \dot{v} = a = \frac{k}{\lambda L} \tag{3.23}$$

The following result is obtained

$$k - T(x) = \lambda x \left(\frac{k}{\lambda L} \right) + \lambda v^2 \tag{3.24}$$

The expression for tension at the control volume boundary, at a distance x from the point of application of the force is given by:

$$T(x) = k\left(1 - \frac{x}{L}\right) - \lambda v^2 \tag{3.25}$$

The tension is expected to decline linearly with distance from the point of application of the force. Consequently the term λv^2 appears as a spurious term in the tension expression of equation (3.25).

3.5.2 Variable Mass Newtonian Analysis.

Next, Tiersten's formulation discussed in Section 3.3 is applied to the present problem. Accordingly, the dynamics of the principal part of the system i.e. the cable within the control volume is given by:

$$\frac{d(Mv)}{dt} = F^{ext} + u\frac{dM}{dt} \tag{3.26}$$

The various terms in equation (3.26) are:

$$M = \lambda x\,;\; u = v = \dot{x}\,;\; F^{ext} = k - T(x) \tag{3.27}$$

From equations (3.26) and (3.27),

$$\frac{d(\lambda xv)}{dt} = (k - T(x)) + v(\lambda v) \tag{3.28}$$

Evaluation of the terms in (3.28) using the results from equation (3.23) gives the expression for the tension at the control volume boundary as:

$$T(x) = k\left(1 - \frac{x}{L}\right) \tag{3.29}$$

This is the correct expression for tension. It is noted that the spurious term λv^2 appearing in equation (3.26) is removed through the inclusion of the momentum flux term. This shows the appropriateness of the momentum flux formulation for variable mass dynamics problems where the dynamics of only a finite volume of a spatially distributed system is

of interest. The results of this case study reinforce the decision to use the Eulerian approach based on Newton's second law for variable mass cable dynamics in this work.

3.6 Variable Length Cable Dynamics

Following the results of the previous Sections, Newton's second law of motion for variable mass systems is applied to the differential boundary element of the cable, in keeping with the Eulerian approach. The governing equation for the variable length differential element can hence be written as:

$$\frac{d(\mathbf{M}(t)\dot{\mathbf{r}}(s,t))}{dt} = \frac{d\mathbf{F}}{ds} + \mathbf{q}(s) + (\lambda V_p \mathbf{I})(V_p \hat{\mathbf{t}}) \tag{3.30}$$

Where, $\mathbf{M}(t)$ is the time-varying mass matrix which is the sum of actual and added mass terms, $\hat{\mathbf{t}}$ is the tangent vector at the interface of the differential element on the cable boundary, and the source of mass flux , which is most commonly the segment of cable on the deployer winch and $\mathbf{I}$ is the identity matrix. Noting that the mass flux, $\frac{d\mathbf{M}(t)}{dt} = \lambda V_p \mathbf{I}$, the above equation may be reduced to obtain

$$\mathbf{M}(t)\frac{d\dot{\mathbf{r}}(s,t)}{dt} = \frac{d\mathbf{F}}{ds} + \mathbf{q}(s) + \lambda V_p \mathbf{I}(V_p \hat{\mathbf{t}} - \dot{\mathbf{r}}(s,t)) \tag{3.31}$$

From equation (3.31), it is apparent that the dynamics of the variable length cable element is given by the dynamics of the fixed length element with time varying mass and an additional term which is a thrust force. This is the third expression on the right hand side of equation (3.31). It has the general form:

$$\mathbf{F}_{thrust} = \frac{d\mathbf{M}}{dt}(\mathbf{V}_{rel}) \tag{3.32}$$

Where $\frac{d\mathbf{M}}{dt} = \lambda V_p \mathbf{I}$ is the mass flux and the relative velocity, $\mathbf{V}_{rel} = V_p \hat{\mathbf{t}} - \dot{\mathbf{r}}(s,t)$.

The next step is to apply Galerkin's Weighted Residual technique to the dynamics equation for a variable length differential element:

$$\mathbf{M}(t)\ddot{\mathbf{r}} = \frac{d\mathbf{F}}{ds} + \mathbf{q} + \frac{d\mathbf{M}}{dt}(V_p \hat{\mathbf{t}} - \dot{\mathbf{r}}) \tag{3.33}$$

in order to obtain the form of the thrust force for a discrete cable element of finite length.

3.7 Application of the Weighted Residual Technique

The first step towards realizing time domain simulation of the new governing motion equation (3.33) is to obtain a discrete spatial representation. The Weighted Residual technique described in Chapter 2 is applied with the cubic spline trial solution to obtain the spatially discrete form of the governing equation. Figure 3.6 shows an assembly of spatially discrete cable elements.

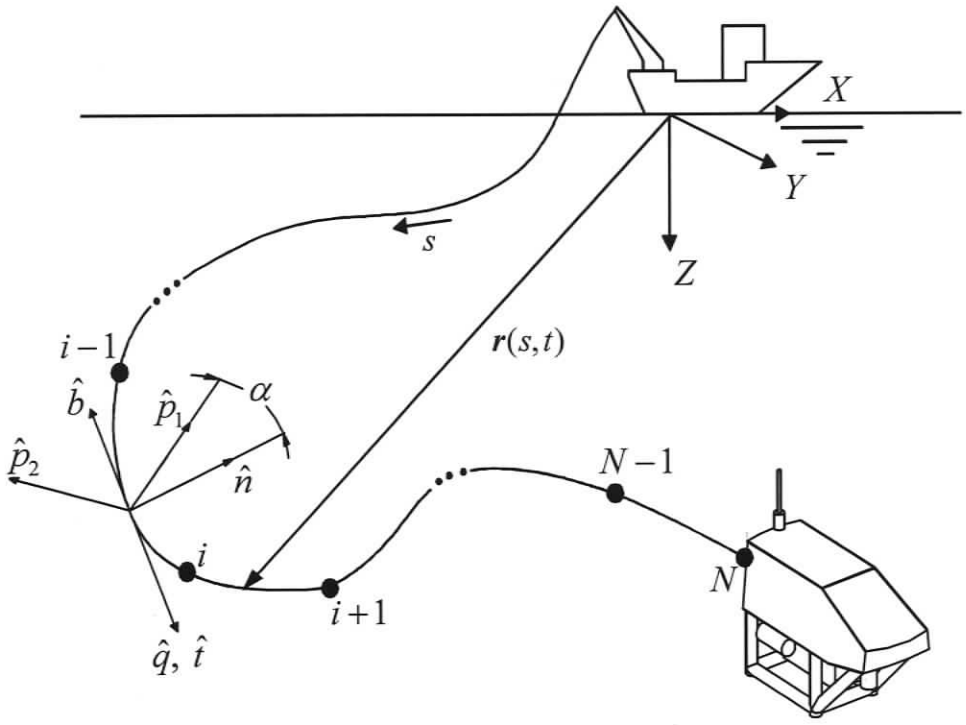

Figure 3.6: Spatially discrete tether consisting of N nodes, labeled $i = 1,2,...,N$. The i^{th} element is bounded by the $(i-1)^{th}$ and the $(i)^{th}$ nodes. For the system shown, in keeping with the Eulerian approach, only the discrete cable element closest the ship, or the $i = 1$ element is variable length whereas all the others are fixed length, and have dynamics equations given by equation (2.29) of Chapter 2.

Here, only the results for the new terms which augment the fixed length dynamics are given. For the two new terms of the right hand side of equation (3.33), the Residual for the i^{th} cable element is evaluated as:

$$\mathbf{Int}(s,t) = \int_{s^{(i-1)}}^{s^{(i)}} \lambda V_p^2 \mathbf{I}\, \hat{\mathbf{t}} \phi_{i,j}(s) ds - \int_{s^{(i-1)}}^{s^{(i)}} \lambda V_p \mathbf{I}\, \dot{\mathbf{r}}_l \phi_{i,j}(s) ds \qquad (3.34)$$

$$j = 1,2,3,4$$

Where $\mathbf{I}$ is the 3×3 identity matrix and $\phi_{i,j}$ are the shape functions or interpolation functions defined in Chapter 2. Each term of the residual in equation (3.34) is considered individually.

The first term is:

$$\mathbf{Int}_1 = \lambda V_p^{\,2} \int_{s^{(i-1)}}^{s^{(i)}} \hat{\mathbf{t}}\, \phi_{i,j}(s)ds\, \mathbf{I} \qquad j=1,2,3,4 \tag{3.35}$$

Here, $\hat{\mathbf{t}}$ is the tangent vector at the interface between the variable length element and the source of mass flux. It is recalled that from the trial solution, the continuous position vector over the span of the i^{th} element is given by the following blend of the positions $\mathbf{r}$ and curvatures $\mathbf{r}''$ of the nodes bounding the element.

$$\mathbf{r}_i(s,t) = \mathbf{r}^{(i-1)}(t)\phi_{i,1}(s) + \mathbf{r}''^{(i-1)}(t)\phi_{i,2}(s) + \mathbf{r}^{(i)}(t)\phi_{i,3}(s) + \mathbf{r}''^{(i)}(t)\phi_{i,4}(s) \tag{3.36}$$

Correspondingly, the first spatial derivative of the position vector is:

$$\mathbf{r}_i' = \mathbf{r}^{(i-1)}\phi_{i,1}' + \mathbf{r}''^{(i-1)}\phi_{i,2}' + \mathbf{r}^{(i)}\phi_{1,3}' + \mathbf{r}''^{(i)}\phi_{i,4}' \tag{3.37}$$

The tangent vector $\hat{\mathbf{t}}$ is related to the first spatial derivative of the position vector, $\mathbf{r}_i'$ through the axial strain of the i^{th} differential element ε_i as:

$$\hat{\mathbf{t}}_i = \frac{1}{1+\varepsilon_i}(\mathbf{r}^{(i-1)}\phi_{i,1}' + \mathbf{r}''^{(i-1)}\phi_{i,2}' + \mathbf{r}^{(i)}\phi_{i,3}' + \mathbf{r}''^{(i)}\phi_{i,4}') \tag{3.38}$$

Where the strain ε_i is taken as the average strain incurred over the element. From equations (3.35) and (3.38), the expression for $\mathbf{Int}_1$ is obtained as a product of a stiffness matrix and the vector of generalized displacements, i.e. nodal positions and curvatures as:

$$\mathbf{Int}_1 = \frac{\lambda V_p^2}{1+\varepsilon_i}\begin{bmatrix} \int_{s^{(i-1)}}^{s^{(i)}} \phi'_{i,1}\phi_{i,1}ds\,\mathbf{I} & \int_{s^{(i-1)}}^{s^{(i)}} \phi'_{i,2}\phi_{i,1}ds\,\mathbf{I} & \int_{s^{(i-1)}}^{s^{(i)}} \phi'_{i,3}\phi_{i,1}ds\,\mathbf{I} & \int_{s^{(i-1)}}^{s^{(i)}} \phi'_{i,4}\phi_{i,1}ds\,\mathbf{I} \\ \int_{s^{(i-1)}}^{s^{(i)}} \phi'_{i,1}\phi_{i,2}ds\,\mathbf{I} & \int_{s^{(i-1)}}^{s^{(i)}} \phi'_{i,2}\phi_{i,2}ds\,\mathbf{I} & \int_{s^{(i-1)}}^{s^{(i)}} \phi'_{i,3}\phi_{i,2}ds\,\mathbf{I} & \int_{s^{(i-1)}}^{s^{(i)}} \phi'_{i,4}\phi_{i,2}ds\,\mathbf{I} \\ \int_{s^{(i-1)}}^{s^{(i)}} \phi'_{i,1}\phi_{i,3}ds\,\mathbf{I} & \int_{s^{(i-1)}}^{s^{(i)}} \phi'_{i,2}\phi_{i,3}ds\,\mathbf{I} & \int_{s^{(i-1)}}^{s^{(i)}} \phi'_{i,3}\phi_{i,3}ds\,\mathbf{I} & \int_{s^{(i-1)}}^{s^{(i)}} \phi'_{i,4}\phi_{i,3}ds\,\mathbf{I} \\ \int_{s^{(i-1)}}^{s^{(i)}} \phi'_{i,1}\phi_{i,4}ds\,\mathbf{I} & \int_{s^{(i-1)}}^{s^{(i)}} \phi'_{i,2}\phi_{i,4}ds\,\mathbf{I} & \int_{s^{(i-1)}}^{s^{(i)}} \phi'_{i,3}\phi_{i,4}ds\,\mathbf{I} & \int_{s^{(i-1)}}^{s^{(i)}} \phi'_{i,4}\phi_{i,4}ds\,\mathbf{I} \end{bmatrix} \begin{Bmatrix} \mathbf{r}^{(i-1)} \\ \mathbf{r}''^{(i-1)} \\ \mathbf{r}^{(i)} \\ \mathbf{r}''^{(i)} \end{Bmatrix} \tag{3.39}$$

Evaluating the integrals within the above matrix, using the definitions of the shape functions $\phi_{i,j}$, the following skew-symmetric stiffness matrix $\left[\mathbf{K}_{\mathbf{thrust}}\right]_i$ is obtained as:

$$\left[\mathbf{K}_{\mathbf{thrust}}\right]_i = \frac{\lambda V_p^2}{1+\varepsilon_i}\begin{bmatrix} -\frac{1}{2}\mathbf{I} & \frac{-L_i^2}{24}\mathbf{I} & \frac{1}{2}\mathbf{I} & \frac{-L_i^2}{24}\mathbf{I} \\ \frac{L_i^2}{24}\mathbf{I} & 0 & \frac{-L_i^2}{24}\mathbf{I} & \frac{L_i^4}{720}\mathbf{I} \\ -\frac{1}{2}\mathbf{I} & \frac{L_i^2}{24}\mathbf{I} & \frac{1}{2}\mathbf{I} & \frac{L_i^2}{24}\mathbf{I} \\ \frac{L_i^2}{24}\mathbf{I} & \frac{-L_i^4}{720}\mathbf{I} & \frac{-L_i^2}{24}\mathbf{I} & 0 \end{bmatrix} \tag{3.40}$$

and the residual is evaluated as:

$$\mathbf{Int}_1 = \left[\mathbf{K}_{\mathbf{thrust}}\right]_i \mathbf{X}_i \tag{3.41}$$

where $\mathbf{X}_i$ is the vector of generalized displacements.

Next consider the second term:

$$\mathbf{Int}_2 = -\int_{s^{(i-1)}}^{s^{(i)}} \lambda V_p \dot{\mathbf{r}}_i \phi_{i,j}(s)ds\,\mathbf{I} \qquad j = 1,2,3,4 \tag{3.42}$$

The expression for the continuous velocity vector follows from differentiating the trial solution in equation (3.36) with respect to time,

$$\dot{\mathbf{r}}_i = \dot{\mathbf{r}}^{(i-1)}\phi_{i,1} + \dot{\mathbf{r}}'^{(i-1)}\phi_{i,2} + \dot{\mathbf{r}}^{(i)}\phi_{1,3} + \dot{\mathbf{r}}'^{(i)}\phi_{i,4} \tag{3.43}$$

From (3.42) and (3.43):

$$\mathbf{Int}_2 = -\lambda V_p \begin{bmatrix} \int_{s^{(i-1)}}^{s^{(i)}} \phi_{i,1}{}^2 ds\,\mathbf{I} & \int_{s^{(i-1)}}^{s^{(i)}} \phi_{i,2}\phi_{i,1} ds\,\mathbf{I} & \int_{s^{(i-1)}}^{s^{(i)}} \phi_{i,3}\phi_{i,1} ds\,\mathbf{I} & \int_{s^{(i-1)}}^{s^{(i)}} \phi_{i,4}\phi_{i,1} ds\,\mathbf{I} \\ \int_{s^{(i-1)}}^{s^{(i)}} \phi_{i,1}\phi_{i,2} ds\,\mathbf{I} & \int_{s^{(i-1)}}^{s^{(i)}} \phi_{i,2}{}^2 ds\,\mathbf{I} & \int_{s^{(i-1)}}^{s^{(i)}} \phi_{i,3}\phi_{i,2} ds\,\mathbf{I} & \int_{s^{(i-1)}}^{s^{(i)}} \phi_{i,4}\phi_{i,2} ds\,\mathbf{I} \\ \int_{s^{(i-1)}}^{s^{(i)}} \phi_{i,1}\phi_{i,3} ds\,\mathbf{I} & \int_{s^{(i-1)}}^{s^{(i)}} \phi_{i,2}\phi_{i,3} ds\,\mathbf{I} & \int_{s^{(i-1)}}^{s^{(i)}} \phi_{i,3}{}^2 ds\,\mathbf{I} & \int_{s^{(i-1)}}^{s^{(i)}} \phi_{i,4}\phi_{i,3} ds\,\mathbf{I} \\ \int_{s^{(i-1)}}^{s^{(i)}} \phi_{i,1}\phi_{i,4} ds\,\mathbf{I} & \int_{s^{(i-1)}}^{s^{(i)}} \phi_{i,2}\phi_{i,4} ds\,\mathbf{I} & \int_{s^{(i-1)}}^{s^{(i)}} \phi_{i,3}\phi_{i,4} ds\,\mathbf{I} & \int_{s^{(i-1)}}^{s^{(i)}} \phi_{i,4}{}^2 ds\,\mathbf{I} \end{bmatrix} \begin{Bmatrix} \dot{\mathbf{r}}^{(i-1)} \\ \dot{\mathbf{r}}'^{(i-1)} \\ \dot{\mathbf{r}}^{(i)} \\ \dot{\mathbf{r}}'^{(i)} \end{Bmatrix} \tag{3.44}$$

Evaluating the above integrals, the following symmetric damping or coriolis matrix is obtained:

$$\left[\mathbf{C}_{\mathbf{thrust}}\right]_i = -\lambda V_p L_i \begin{bmatrix} \frac{1}{3}\mathbf{I} & \frac{-L_i^2}{45}\mathbf{I} & \frac{1}{6}\mathbf{I} & \frac{-7L_i^2}{360}\mathbf{I} \\ \frac{-L_i^2}{45}\mathbf{I} & \frac{2L_i^4}{945}\mathbf{I} & \frac{-7L_i^2}{360}\mathbf{I} & \frac{31L_i^4}{15120}\mathbf{I} \\ \frac{1}{6}\mathbf{I} & \frac{-7L_i^2}{360}\mathbf{I} & \frac{1}{3}\mathbf{I} & \frac{-L_i^2}{45}\mathbf{I} \\ \frac{-7L_i^2}{360}\mathbf{I} & \frac{31L_i^4}{15120}\mathbf{I} & \frac{-L_i^2}{45}\mathbf{I} & \frac{2L_i^4}{945}\mathbf{I} \end{bmatrix} \tag{3.45}$$

and the residual is evaluated as

$$\mathbf{Int}_2 = \left[\mathbf{C}_{\mathbf{thrust}}\right]_i \dot{\mathbf{X}}_i \tag{3.46}$$

where $\dot{\mathbf{X}}_i$ is the vector of generalized velocities.

Hence, the dynamics of the i^{th} element with variable length is given by the following spatially discrete differential equation which is second order in time:

$$\left([\mathbf{K_B}]_i + [\mathbf{K_A}]_i + [\mathbf{K_T}]_i + [\mathbf{K_{thrust}}]_i\right)\mathbf{X}_i + [\mathbf{C_{thrust}}]_i \dot{\mathbf{X}}_i + \mathbf{W}_i + \mathbf{H}_i + \mathbf{B}_i = [\mathbf{M}]_i \ddot{\mathbf{X}}_i \quad (3.47)$$

The other terms in equation (3.47) represent the dynamics of the fixed length element, as described in equation (2.29) of Chapter 2. $[\mathbf{K_B}]_i, [\mathbf{K_A}]_i, [\mathbf{K_T}]_i$ are the stiffness matrices corresponding to the internal bending, axial, and torsional forces respectively. Load vectors $\mathbf{W}_i, \mathbf{H}_i, \mathbf{B}_i$ represent the buoyancy, hydrodynamic and boundary loads respectively. $[\mathbf{M}]_i$ is the mass matrix, including the added mass and true mass terms.

Next, the consistent mass matrix $[\mathbf{M}]_i$ is made diagonal in keeping with the lumped mass assumption as discussed in Section 2.2.4, by pre-multiplying both sides of equation (3.47) by $\mathbf{P}_i$, where

$$\mathbf{P}_i = \begin{bmatrix} \mathbf{I} & \frac{1}{L_i^2}\mathbf{I} & \mathbf{0} & \mathbf{0} \\ \mathbf{0} & \mathbf{0} & \mathbf{I} & \frac{1}{L_i^2}\mathbf{I} \end{bmatrix} \quad (3.48)$$

The corresponding expressions for the thrust force terms are:

$$\mathbf{P}_i[\mathbf{K_{thrust}}]_i = \frac{\lambda V_p^2}{1+\varepsilon_i}\begin{bmatrix} \frac{-11}{24}\mathbf{I} & \frac{-1}{24}L_i^2\mathbf{I} & \frac{11}{24}\mathbf{I} & \frac{-29}{720}L_i^2\mathbf{I} \\ \frac{-11}{24}\mathbf{I} & \frac{29}{720}L_i^2\mathbf{I} & \frac{11}{24}\mathbf{I} & \frac{1}{24}L_i\mathbf{I} \end{bmatrix} \quad (3.49)$$

$$\mathbf{P}_i[\mathbf{C}_{\mathbf{thrust}}]_i = -\lambda V_p L_i \begin{bmatrix} \frac{14}{45}\mathbf{I} & \frac{-19}{945}L_i^2\mathbf{I} & \frac{53}{360}\mathbf{I} & \frac{-263}{15120}L_i^2\mathbf{I} \\ \frac{53}{360}\mathbf{I} & \frac{-263}{15120}L_i^2\mathbf{I} & \frac{14}{45}\mathbf{I} & \frac{-19}{945}L_i^2\mathbf{I} \end{bmatrix} \tag{3.50}$$

The above expression for $\mathbf{P}_i[\mathbf{C}_{\mathbf{thrust}}]_i$ represents the contributions of the time derivative of the curvature $\dot{\mathbf{r}}'$ in addition to the velocities $\dot{\mathbf{r}}$. It may be partitioned as:

$$\mathbf{P}_i[\mathbf{C}_{\mathbf{thrust}}]_i = -\lambda V_p L_i \left(\begin{bmatrix} \frac{14}{45}\mathbf{I} & \frac{53}{360}\mathbf{I} \\ \frac{53}{360}\mathbf{I} & \frac{14}{45}\mathbf{I} \end{bmatrix} \left\{ \dot{\mathbf{r}}^{(i-1)} \;\; \dot{\mathbf{r}}^{(i)} \right\}^T + \begin{bmatrix} \frac{-19}{945}L_i^2\mathbf{I} & \frac{-263}{15120}L_i^2\mathbf{I} \\ \frac{-263}{15120}L_i^2\mathbf{I} & \frac{-19}{945}L_i^2\mathbf{I} \end{bmatrix} \left\{ \dot{\mathbf{r}}'^{(i-1)} \;\; \dot{\mathbf{r}}'^{(i)} \right\}^T \right) \tag{3.51}$$

Following the work of Buckham et al [11], as described in Chapter 2, the lumped mass model concentrates the element mass at the node points with the rate of change of curvature not being associated with any momentum change. Hence, the last matrix term with time derivatives of curvature, on the right hand side of equation (3.51) is dropped, to get;

$$\mathbf{P}_i[\mathbf{C}_{\mathbf{thrust}}]_i = -\lambda V_p L_i \begin{bmatrix} \frac{14}{45}\mathbf{I} & \frac{53}{360}\mathbf{I} \\ \frac{53}{360}\mathbf{I} & \frac{14}{45}\mathbf{I} \end{bmatrix} \left\{ \dot{\mathbf{r}}^{(i-1)} \;\; \dot{\mathbf{r}}^{(i)} \right\}^T \tag{3.52}$$

The next step is to assemble the individual element equations to obtain the global dynamics formulation for the tether, which is a concatenation of N cubic spline elements. In this work, we are most frequently concerned with the case when the ship is deploying/retrieving cable connected to an underwater vehicle. The equation (3.47) is applicable only for a variable length boundary element which is at the interface of the cable and source of mass flux. Consequently, in this case, the topmost element, $i = 1$, is of

varying length and all others are of fixed length, and the spatially discrete differential equations for them are obtained by setting $V_p = 0$. The final form of the Global assembled equations is:

$$\left([\mathbf{K_B}]_G + [\mathbf{K_A}]_G + [\mathbf{K_T}]_G + [\mathbf{K_{thrust}}]_G\right)\mathbf{X}_G + [\mathbf{C_{thrust}}]_G \dot{\mathbf{X}}_G + \mathbf{W}_G + \mathbf{H}_G + \mathbf{B}_G = [\mathbf{M}]_G \ddot{\mathbf{X}}_G \tag{3.53}$$

Where the subscript $_G$ represents a globally assembled entity as mentioned in Chapter 2, Section 2.2.5.

The thrust force terms in the global assembly are obtained as:

$$[\mathbf{K_{thrust}}]_G = \frac{\lambda V_p^2}{1+\varepsilon_i}\begin{bmatrix} \frac{-11}{24}\mathbf{I} & \frac{-1}{24}L_i^2\mathbf{I} & \frac{11}{24}\mathbf{I} & \frac{-29}{720}L_i^2\mathbf{I} & 0 & \cdots & 0 \\ \frac{-11}{24}\mathbf{I} & \frac{29}{720}L_i^2\mathbf{I} & \frac{11}{24}\mathbf{I} & \frac{1}{24}L_i\mathbf{I} & 0 & \cdots & 0 \\ 0 & 0 & 0 & 0 & 0 & \cdots & 0 \\ \vdots & \vdots & \vdots & \vdots & \vdots & \vdots & \vdots \\ 0 & 0 & 0 & 0 & 0 & 0 & 0 \\ 0 & 0 & 0 & 0 & 0 & 0 & 0 \end{bmatrix}_{3N\times 3N} \tag{3.54}$$

$$[\mathbf{C_{thrust}}]_G = -\lambda V_p L_i \begin{bmatrix} \frac{14}{45}\mathbf{I} & \frac{53}{360}\mathbf{I} & 0 & 0 & 0 & \cdots & 0 \\ \frac{53}{360}\mathbf{I} & \frac{14}{45}\mathbf{I} & 0 & 0 & 0 & \cdots & 0 \\ 0 & 0 & 0 & 0 & 0 & \cdots & 0 \\ \vdots & \vdots & \vdots & \vdots & \vdots & \vdots & \vdots \\ 0 & 0 & 0 & 0 & 0 & 0 & 0 \\ 0 & 0 & 0 & 0 & 0 & 0 & 0 \end{bmatrix}_{3N\times 3N} \tag{3.55}$$

3.8 Closure

In this chapter, the governing equation for the dynamics of variable length tether of an ROV is derived. The Lagrangian and Eulerian approaches to the variable length dynamics modeling are examined, and the Eulerian framework was adopted on account of it's applicability to the low tension variable length cable dynamics. Newton's second law of motion for variable mass systems is obtained by augmenting Newton's second law for fixed mass systems with the momentum flux term. Two examples, that of the thrust on a rocket, and the motion of a cable are presented to highlight the significant features of Newton's second law for variable mass systems. A general expression for thrust force on a differential element during cable deployment and retrieval is formulated and the discrete spatial representation for the continuous cable of varying length is obtained by Galerkin's Weighted Residual technique. The formulation is kept consistent with that adopted in the fixed length dynamics model. This consistency enables the simple augmenting of the fixed length dynamics equation with the new terms reflecting the effect of variable undeformed length of the cable elements. Hence the new variable length element inherits the virtues of the fixed length formulation, in particular, the need for a minimal number of state variables to simulate the dynamics, as discussed in Chapter 2.

The governing equation for the variable length element does not impose any restriction on where this element may be placed in the discrete cable element assembly. The Eulerian framework permits the flexibility of defining a variable length boundary element

at the interface of a mass flux source anywhere along the length of the cable. This would enable the modeling of cabled systems with multiple branches, and with each branch having its own tether management system.

Having obtained the motion equation for the spatially discrete representation of the variable length cable, the next chapter considers the time integration of the motion equation to propagate the variable length tether state in time. Implicit and Explicit integrators are considered for the integration. The implication of the Eulerian framework in terms of confining the mass flow to the boundary element is revisited. We consider the logistics of integrating the length change during pay-out/reel-in to maintain knowledge of the actual element length and look at a rediscretization of the cable assembly to maintain the boundary element length within prescribed limits.

Chapter 4
Time Domain Simulation of Variable Length Tether Dynamics

4.1 Overview

Chapter 3 presented the spatially discrete equations that are the basis for the ROV simulations and controller synthesis of Chapter 5. In this chapter the spatially discrete governing dynamics equations of Section 3.7 are integrated in time using two numerical integrators: the adaptive Runge-Kutta, and the Generalized-α integrators. The numerical and logistical issues surrounding the time domain integration of the dynamics of variable length elements are addressed. A primary focus is the model behavior during rediscretization. As discussed in Chapter 3, cable length changes are contained to a boundary element. In this Chapter it is shown that elements must be added or subtracted such that the boundary element length is bounded. In Section 4.2 the explicit adaptive Runge-Kutta and implicit Generalized-α integrators are reviewed. This is followed by an introduction to the algorithmic damping of the Generalized-α integrator in Section 4.3. Section 4.4 introduces the concept of normalized strain energy as a means to evaluate the performance of the time integration algorithms. In Section 4.5, time domain simulations of variable length cables are presented. Two cases, that of a taut cable with a depressor, and a slack neutrally buoyant cable are considered. In the first case, the influence of the algorithmic dissipation of the Generalized-α integrator on the time domain modeling of the deployment and retrieval of

axially stiff cables is presented. In the second case, the implication of the Eulerian framework, whereby the effects of the varying length are restricted to the region of the cable closest the deployer, is brought out.

4.2 Time Integration.

Having obtained the spatially discrete form of the governing dynamics equation for the continuous cable, the next step is to obtain time domain simulation of the dynamics by propagating the globally assembled equations given by (3.53) in time. This is achieved by the use of a time integration algorithm as demonstrated in Figure 4.1 below.

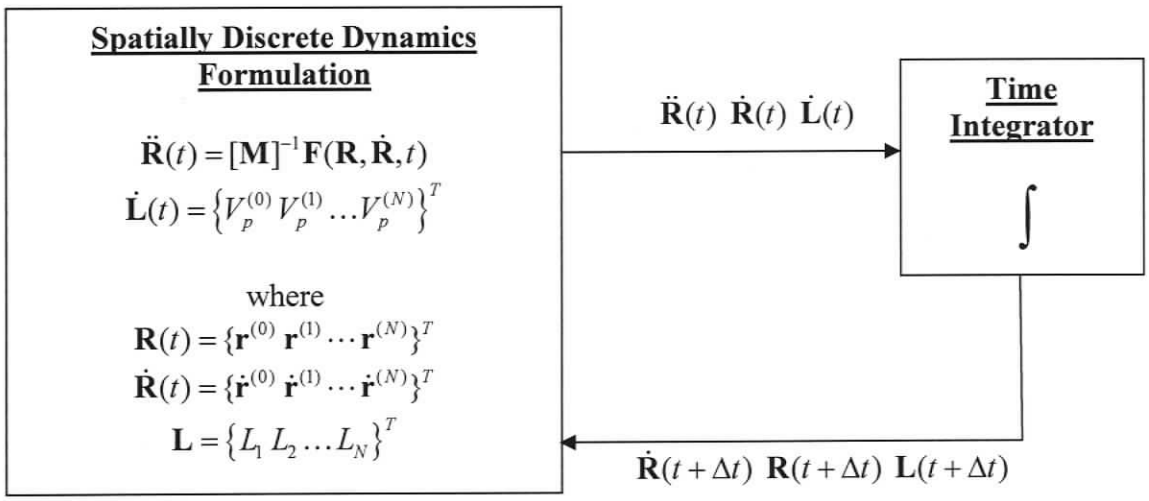

Figure 4.1: Schematic of time integration. The time integrator calls the dynamics function to retrieve derivatives of the state variables which it uses to update the state variables in time.

As seen above, the integrator takes the velocities $\dot{\mathbf{R}}(t)$, accelerations $\ddot{\mathbf{R}}(t)$ and deployment/retrieval rates $\dot{\mathbf{L}}(t)$ at a given time station t as input, and produces as output the new positions $\mathbf{R}(t+\Delta t)$, velocities $\dot{\mathbf{R}}(t+\Delta t)$ and unstretched element lengths $\mathbf{L}(t+\Delta t)$ a finite interval of time Δt in the future. The size of the time step Δt that can be used is a

function inherent in the system dynamics, the desired accuracy, and the algorithmic damping (or stability of the numerical integrator).

Integration algorithms for dynamics problems may be classified into explicit and implicit algorithms. In this work, we consider the explicit adaptive Runge-Kutta algorithm and the implicit Generalized-α algorithm. The fundamental difference between the two is that in explicit integrators, the differentials are approximated as backward differences whereas implicit integrators approximate differentials as forward differences. Consider the simple first order differential equation:

$$\frac{\mathrm{d}x(t)}{\mathrm{d}t} = f(x,t) \tag{4.1}$$

When the dependent variable x in the above equation is approximated by a backward difference, as in an explicit time integrator, the discrete form of the equation is given as:

$$\frac{x(t+\Delta t)-x(t)}{\Delta t} = f(x(t),t) \tag{4.2}$$

So, the future value of x depends on the value of the function f evaluated at the present instant of time t.

When the dependant variable x in the equation (4.1) above is approximated by a forward difference, as in an implicit time integrator, the solution is given as:

$$\frac{x(t+\Delta t)-x(t)}{\Delta t} = f(x(t+\Delta t),t+\Delta t) \tag{4.3}$$

Clearly, the future value of x depends on the value of the function f evaluated at a future instant of time $t+\Delta t$. Hence the term "implicit". Appendix A presents numerical case studies on the stability of explicit and implicit integrators.

In the context of structural dynamics problems, the function f can be regarded as the forcing function. Consequently it is seen that while an explicit integrator uses the value of the forcing function at the start of the time integration step, the implicit integrator relies on knowledge of the function at some future time station. The difficulty in implementing implicit techniques is that the nonlinear dynamics function f makes solution for the future states $x(t+\Delta t)$ an iterative process. In this Chapter, both implicit Generalized-α (Hulbert and Chung [22]) and explicit adaptive Runge-Kutta integration algorithms are used in the time domain simulation of the variable length cable dynamics. The Generalized-α integrator, uses a fixed time step, and looks for unconditional stability for the linear problem. The adaptive Runge-Kutta integrator on the other hand looks for robustness by varying the time step size during the time domain integration.

4.3 Rediscretization during variable length cable dynamics modeling.

As described in the previous section, the nominal lengths of the elements $\mathbf{L}(t)$ are state variables and are integrated in time. For the Eulerian framework used in this work, the only variable length element is the boundary element at the interface of the cable on the winch and the segment of cable deployed in the water. Consequently, the length of this element would increase during deployment. One of the primary decisions to be made in any finite element model is the size of the mesh. This corresponds to the unstretched lengths of the elements in the assembly. Long elements result in poor spatial resolution of the dynamics being modeled. Hence it is desirable to constrain the size of the growing boundary element during deployment. When a variable length element exceeds the prescribed length limit, it's growth

is stopped. A new element is subjected to increasing length from this point onwards. This represents the introduction of a new element from the cable winch on the ship into the water.

On the other hand, during retrieval, the length of the boundary element decreases. A zero length element in the deployed cable assembly would represent a singularity that the time domain simulation is unable to handle. In addition, the presence of a very short element would introduce spurious high frequency modes, not otherwise present in the dynamic response of the actual system, resulting in a numerical instability in the time integration process. Hence, when the length of the element being retrieved falls below a certain limit, it is removed from the assembly, and the subsequent downstream element now becomes the element of declining length or the new boundary element. This represents the process of an element leaving the water for the ship winch.

4.4 Algorithmic Damping in the implicit time integrator

When the cable is discretized, a series of small elements are concatenated to represent the cable in space. These small discrete elements may introduce high frequency motions that are not present in the actual system as was mentioned in Section 4.3. The implicit Generalized-α integrator provides a user-specified level of numerical dissipation of the high frequency modes, while leaving the lower frequency modes unaffected. This Section provides a review of the implicit integrator, and the concept of numerical dissipation.

4.4.1 Implicit Integrators for Structural Dynamics

The Generalized-α integrator is the newest of the implicit integrators that have been developed over the last four decades. The work of Hulbert and Chung [22] has established

the basic framework of the algorithm. Gobat et al [23] have applied it to the integration of the motion of a hanging chain. Buckham et al [24] have demonstrated its utility in low tension tether dynamics.

The spatially discrete nonlinear governing cable dynamics equation obtained in Chapters 2 and 3 can be written as:

$$[\mathbf{M}]\ddot{\mathbf{R}} = \mathbf{F}(\mathbf{R}, \dot{\mathbf{R}}, t) \tag{4.4}$$

Where $[\mathbf{M}]$ is the assembled mass matrix in the inertial frame of reference including the added mass terms. The equation (4.4) may be written without loss of generality in the form:

$$[\mathbf{M}]\ddot{\mathbf{R}}(t) + [\mathbf{C}]\dot{\mathbf{R}}(t) + [\mathbf{K}]\mathbf{R}(t) = \mathbf{F}_{ext}(t) \tag{4.5}$$

In the above, $\mathbf{F}_{ext}(t)$ is the external forcing term. $[\mathbf{C}]$ and $[\mathbf{K}]$ are the nonlinear matrices that are themselves functions of $\mathbf{R}$ and $\dot{\mathbf{R}}$. In the literature, equation (4.5) is called the semi-discrete structural dynamics equation to denote the fact that it is discrete in space but continuous in time.

The Generalized -α integrator is one of the family of implicit integrators that are designed specifically for this second order differential equation. The most commonly used implicit time integration algorithm is the Newmark-β algorithm, which serves as the starting point for the discussion here.

In addition to the governing dynamics equation (4.5) the Newmark-β integrator uses Taylor series expansions in the time parameter for the position and velocity vectors, $\mathbf{R}(t)$ and $\dot{\mathbf{R}}(t)$ respectively to provide two more equations:

$$\mathbf{R}_{t+\Delta t} = \mathbf{R}_t + \Delta t\dot{\mathbf{R}}_t + \frac{\Delta t^2}{2!}\ddot{\mathbf{R}}_t + \frac{\Delta t^3}{3!}\dddot{\mathbf{R}}_t + \ldots \tag{4.6}$$

$$\dot{\mathbf{R}}_{t+\Delta t} = \dot{\mathbf{R}}_t + \Delta t\ddot{\mathbf{R}}_t + \frac{\Delta t^2}{2!}\dddot{\mathbf{R}}_t + \ldots \tag{4.7}$$

Here, the subscript denotes the time at which the quantity is evaluated. Δt is the time step used. Newmark [25] truncated these equations to third order and expressed them in the following form:

$$\mathbf{R}_{t+\Delta t} = \mathbf{R}_t + \Delta t\dot{\mathbf{R}}_t + \frac{\Delta t^2}{2!}\ddot{\mathbf{R}}_t + \beta\frac{\Delta t^3}{3!}\dddot{\mathbf{R}} \tag{4. 8}$$

$$\dot{\mathbf{R}}_{t+\Delta t} = \dot{\mathbf{R}}_t + \Delta t\ddot{\mathbf{R}}_t + \gamma\frac{\Delta t^2}{2!}\dddot{\mathbf{R}} \tag{4. 9}$$

Where β and γ are algorithmic parameters accounting for the truncation of higher order terms in the original Taylor series expansion. Newmark assumed a linear variation of acceleration with time, to obtain the expression for the jerk as:

$$\dddot{\mathbf{R}} = \frac{\ddot{\mathbf{R}}_{t+\Delta t} - \ddot{\mathbf{R}}_t}{\Delta t} \tag{4.10}$$

From the result of equation (4.10), equations (4.8) and (4.9) can be written as:

$$\mathbf{R}_{t+\Delta t} = \mathbf{R}_t + \Delta t\dot{\mathbf{R}}_t + \frac{\Delta t^2}{2!}((1-2\beta)\ddot{\mathbf{R}}_t + 2\beta\,\ddot{\mathbf{R}}_{t+\Delta t}) \tag{4.11}$$

and

$$\dot{\mathbf{R}}_{t+\Delta t} = \dot{\mathbf{R}}_t + \Delta t((1-\gamma)\ddot{\mathbf{R}}_t + \gamma\ddot{\mathbf{R}}_{t+\Delta t}) \tag{4.12}$$

From the above, it is clear that both the position $\mathbf{R}_{t+\Delta t}$ and the velocity $\dot{\mathbf{R}}_{t+\Delta t}$ involve a linear blend of the asynchronous accelerations, $\ddot{\mathbf{R}}_t$ and $\ddot{\mathbf{R}}_{t+\Delta t}$ respectively. The algorithmic parameters β and γ act as weights in the linear blend. The equations (4.11) and (4.12) are

referred to as the *update equations* whereas equation (4.5) is referred to as the *balance equation* of the time integration algorithm. Given the initial state defined by $\mathbf{R}_t, \dot{\mathbf{R}}_t, \ddot{\mathbf{R}}_t$, equations (4.11) and (4.12) along with equation (4.5) provide three equations for the three unknowns $\mathbf{R}_{t+\Delta t}, \dot{\mathbf{R}}_{t+\Delta t}, \ddot{\mathbf{R}}_{t+\Delta t}$.

The time-marching integration scheme can be represented, for a linear dynamics formulation in symbolic form as:

$$\mathbf{x}_{t+\Delta t} = [\mathbf{A}]\mathbf{x}_t \tag{4.13}$$

Where $\mathbf{x}$ is the state vector, and $[\mathbf{A}]$ is the amplification matrix which produces new states in time. For the linear dynamics function, as shown by Bathe and Wilson [37] , the principle of modal superposition enables one to decouple the overall response into the individual modal dynamics, with each mode treated as an undamped single degree of freedom dynamical system. The time-stepping equation (4.13) is obtained by tiling together the n single degree of freedom systems where n is the number of degrees of freedom in the spatially discrete assembly. The amplification matrix $[\mathbf{A}]$ is a function of the time integrator algorithmic parameters and the time step Δt used. The spectral radius $\rho(\Delta t)$ is defined as the largest magnitude eigenvalue of $[\mathbf{A}]$. The spectral radius describes how initial disturbances from the equilibrium state are attenuated or amplified by the integration scheme. For the time integration of the linear problem to be unconditionally stable, it is required that the spectral radius be lesser than or equal to unity for all the component modal frequencies of the dynamic response. A spectral radius lesser than unity will kill oscillations whereas a spectral radius greater than unity will cause the oscillations to grow unbounded, representing a

numerical instability. As the time step Δt increases, so does the spectral radius ρ. In the literature, the parameters of the Newmark-β integrator are taken as $\beta = \frac{1}{4}, \gamma = \frac{1}{2}$ with a suitable time-step to ensure a spectral radius equal to unity.

4.4.2 The Generalized-α integrator

The Newmark-β method has been used extensively over half a century for practical structural dynamics problems. However in most dynamics problems, it is desirable for the integration algorithm to provide a means to regulate the energy dissipation. In an ideal scenario, the integrator should damp out the high frequency modes of motion, those modes occurring in periods smaller than the time step, while leaving the lower frequency modes, occurring on periods larger than the time step, unaffected. This requirement stems from the fact that in most structural and multi-body dynamics problems, the high frequency modes represent parasitic motions, whereas the actual dynamic response is contained within the low frequency modes. This dissipation produced by the time integrator is referred to as algorithmic damping or numerical dissipation. Miranda et al [26] showed that algorithmic damping in implicit integrators results from the manipulation of the balance equation (4.5), so that not all terms are evaluated at the same time station. This principle was adopted by Hulbert and Chung [22], in the development of the Generalized-α algorithm. Modak and Sotelino [38] later related the work of Newmark [25], Bathe and Wilson [37] and Hulbert and Chung [22] by providing a nine parameter implicit integrator that encompassed all of these particular forms.

The Generalized -α algorithm uses update equations that are identical to the Newmark relations given in equations (4.11) and (4.12). The governing nonlinear dynamics equation is written for the Generalized -α integrator as:

$$[\mathbf{M}]_t \ddot{\mathbf{R}}_{t+\Delta t-\alpha_m} + [\mathbf{C}]_t \dot{\mathbf{R}}_{t+\Delta t-\alpha_f} + [\mathbf{K}]_t \mathbf{R}_{t+\Delta t-\alpha_f} = \mathbf{F}_{t+\Delta t-\alpha_f} \tag{4.14}$$

Where the subscript denotes the instant of time within the time step Δt between t and $t+\Delta t$ at which the respective quantity is considered. It is interpreted as linear blend between the values of the quantity at the start and the end of the time step, with an algorithmic parameter acting as the weighting term in the blend. So that:

$$(*)_{t+\Delta t-\alpha} = (1-\alpha)(*)_{t+\Delta t} + \alpha(*)_t \tag{4.15}$$

Figure 4.2 shows the evaluation of the different terms in the governing dynamics equation for the Generalized-α algorithm.

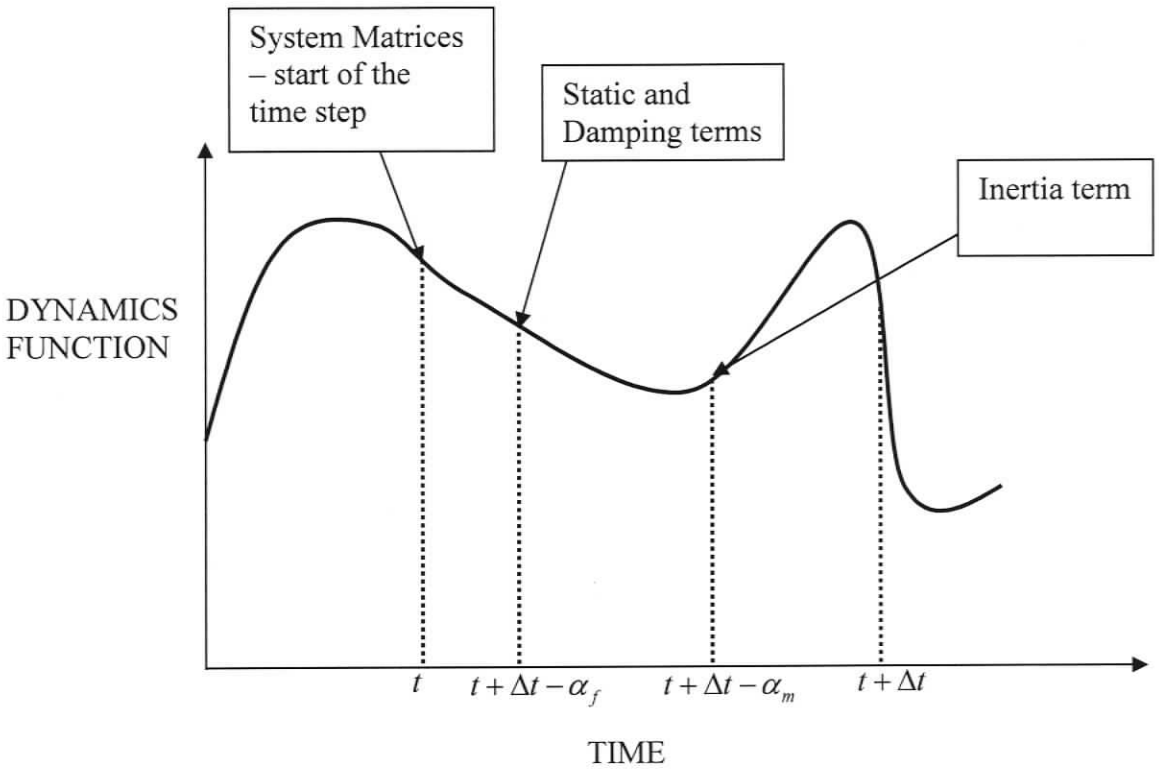

Figure 4.2: Evaluation of the various terms in the balance equation for the Generalized-α integrator.

The new parameters α_m and α_f regulate the contributions of the state variables from the beginning and end of the time step, and therefore introduce numerical damping. The degree of numerical dissipation is characterized in terms of the spectral radius. For the Generalized - α integrator applied to a linear dynamical formulation, the amplification matrix of equation (4.13), $[\mathbf{A}]$ is a function of the algorithmic parameters, $\alpha_m, \alpha_f, \beta, \gamma$, and the dimensionless frequency $\Omega = \omega \Delta t$, where Δt is the time step, and ω is the frequency of the mode

representing the single degree of freedom system as discussed previously. For the time integration of the linear problem to be unconditionally stable, it is required that the spectral radius ρ be lesser than or equal to unity for all frequencies $\Omega \to [0,\infty]$. Hulbert and Chung [22] show through asymptotic analysis that in the high frequency limit, $\Omega \to \infty$, the spectral radius is given by:

$$\rho_\infty = \frac{\alpha_f - \alpha_m - 1}{\alpha_f - \alpha_m + 1} \tag{4.16}$$

The numerical value of ρ_∞ may be set by the user. It defines the level of damping of the high frequency content of the dynamic response. A low value of ρ_∞ produces strong dissipation of the high frequency modes, and vice-versa. This is the mechanism by which the algorithmic damping of the integrator may be tuned. The optimal values of the algorithmic parameters, in terms of prescribed algorithmic damping ρ_∞ is given by Hulbert and Chung [22] as follows. For unconditional stability for the linear problem:

$$\alpha_m < \alpha_f \le \frac{1}{2}, \beta \ge \frac{1}{4} + \frac{1}{2}\left(-\alpha_m + \alpha_f\right) \tag{4.17}$$

For second order accuracy:

$$\gamma = \frac{1}{2} - \alpha_m + \alpha_f \tag{4.18}$$

For optimal high frequency dissipation and minimum low-frequency impact:

$$\alpha_m = \frac{2\rho_\infty - 1}{\rho_\infty + 1}, \alpha_f = \frac{\rho_\infty}{\rho_\infty + 1}, \beta = \frac{1}{4}\left(1 - \alpha_m + \alpha_f\right) \tag{4.19}$$

It is noted that the theory is developed for linear dynamical systems. There exists no means by which to guarantee the unconditional stability for the nonlinear dynamics of the problem

at hand. Consequently the Generalized - α integrator is used with small time step, of the order of a millisecond, to maintain stability and ensure good accuracy. If larger time steps are chosen, the simulations may progress, but significant modes of motion may be cut out. A spectral radius of 0.1, corresponding to high level of damping for high frequency modes, is selected for the simulations in this work. Equations (4.11), (4.12) and (4.14) comprise a system of algebraic equations, and given the state at the start, subsequent states are produced through the solution of the above system of algebraic equations. This system of equations is linear for the linear dynamics problem and can be solved through the standard matrix techniques. However, for the nonlinear cable dynamics, the resulting system of equations is nonlinear. An iterative technique, the globally convergent Newton-Raphson scheme (Press et al [27]) is then used. The Newton-Raphson solver is implemented based on convergence on an initial guess of the acceleration $\ddot{\mathbf{R}}_{t+\Delta t}$.

4.5 Strain Energy in Variable Length Cable Mechanics

For continuous variable length tethers, the strain energy must remain continuous during deployment or retrieval. During rediscretization steps, the numerical integrators are the dominant factor in capturing this continuous strain energy variation. The strain energy serves as a measure by which to gauge the performance and utility of an integrator used in modeling the undersea cable dynamics. In this Section, the strain energy for the cable is derived, and the normalized strain energy is presented as a performance metric for the numerical cases of time domain simulation of variable length cable dynamics taken up in the next Section.

Consider the i^{th} element of the cable subjected to uniform tension T_i as shown in the Figure 4.3.

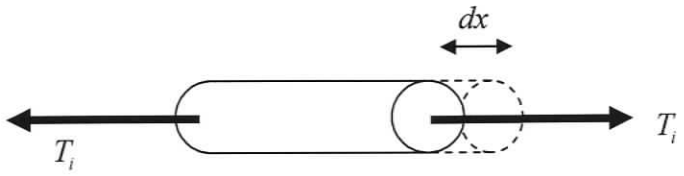

Figure 4.3: A differential element of the cable assembly subjected to an elongation of dx. The Strain Energy is the energy required to effect this elastic deformation.

The elementary work dU_i done by the tension T_i in elongating the element by differential length dx is given by

$$dU_i = T_i\, dx \tag{4.20}$$

So, for a finite elongation of the element by x_1 the net work is given by:

$$U_i = \int_0^{x_1} T_i\, dx \tag{4.21}$$

The work done by the tension T_i results in the increase of energy associated with the deformation of the element. This energy is referred to as the strain energy of the element. It is given by equation (4.21). The total strain energy depends on the length of the element L_i and the cross sectional area A_i of the element. The effect of size of the element on the strain energy may be removed by considering the strain energy density, or strain energy per unit volume. This is defined as:

$$\frac{U_i}{V_i} = \int_0^{x_1} \frac{T_i}{A_i} \frac{dx}{L_i} \tag{4.22}$$

Where $V_i = A_i\ L_i$ is the volume of the element. Recalling that $\frac{T_i}{A_i}$ represents the normal stress σ_x on the element, and $\frac{x}{L_i}$ is the normal strain ε_x, the expression for strain energy density u_i is obtained as :

$$u_i = \frac{U_i}{V_i} = \int_0^{\varepsilon_x} \sigma_x d\varepsilon_x \tag{4.23}$$

For elastic deformations, the normal stress σ_x varies linearly with the strain ε_x as:

$$\sigma_x = E\varepsilon_x \tag{4.24}$$

where E is the Young's modulus of the material.

From equations (4.23) and (4.24), the strain energy density for the uniformly loaded cable element is obtained as:

$$u_i = \frac{1}{2} E\varepsilon_x^2 = \frac{1}{2}\sigma_x\varepsilon_x = \frac{1}{2}\frac{\sigma_x^2}{E} \tag{4.25}$$

The total strain energy follows from equation (4.21) as:

$$U_i = \frac{T_i^2 L_i}{2EA_i} \tag{4.26}$$

In order to eliminate the effect of material and geometric properties, the Normalized Strain Energy is defined for the i^{th} cable element as:

$$\xi_i = T_i^2 L_i \tag{4.27}$$

4.6 Time Domain simulation of variable length cable dynamics

In this Section, two numerical cases of variable length cable dynamics modeling are studied. In the first case, a taut cable is deployed and retrieved at a rapid rate. The two integrators – implicit Generalized -α and explicit adaptive Runge-Kutta are used. It is seen that the algorithmic damping of the implicit Generalized -α enables it to dissipate high-frequency motions encountered during the rediscretization process.

In the second case, the rapid deployment of slack tether is considered to illustrate the Eulerian framework adopted in this work. A convergence analysis is used to demonstrate the loss in accuracy as the boundary element length increases.

4.6.1. Deployment and Retrieval of taut cable.

Here, the dynamics of a variable length cable suspended under the weight of a spherical depressor are modeled. The properties of the cable are listed in Table 4.1 below.

Property	Value
Tether Diameter	0.03332 m
Initial Cable Length (L_{TOT})	5.0 m
Torsional Rigidity (GJ)	1.00 Nm^2
Bending Stiffness (EI)	11920 Nm^2
Viscous Damping Coefficient	437 Ns
Tether Density (ρ_c)	1025.0 kg/m^3
Water Density (ρ_w)	1025.0 kg/m^3
Depressor Diameter	0.1 m
Depressor Drag Coefficient	1

Table 4.1: Properties of the tether used for variable length taut cable dynamics modeling . Three different values of axial stiffness are used in the tests.

The axial stiffness of the cable is given by the product of the Young's modulus (E) and the cross-sectional area of the cable (A). A range of Young's modulus have been reported in the literature on underwater cable dynamics. Buckham et al [11] use a neutrally buoyant umbilical with Young's modulus of 5 GPa. Burgess [9] quotes a higher Young's modulus of 50 GPa for the wire cored communication cable. In this study, three different values of axial stiffness, 0.45×10^6 N, 4.5×10^6 N and 45×10^6 N are used.

Starting with an initial deployed length of 0.1 m, cable is deployed at the rate of 0.5 m/s for 30 seconds, following which it is retrieved at the same rate. The rediscretization steps are carried out to maintain the length of the boundary element within 5 m during deployment and above 0.01 m during retrieval. The variation in strain energy during the maneuver, through the use of the explicit adaptive Runge-Kutta and the implicit Generalized-α integrators are plotted. The time-steps used for the integrators are listed in Table 4.2 below.

Tether Axial Stiffness	Adaptive Runge-Kutta Time Step (average time step)	Generalized-α Time Step (fixed time step, spectral radius = 0.1)
0.45×10^6 N	0.003946 s	0.005 s
4.5×10^6 N	0.001912 s	0.005 s
45×10^6 N	0.000636 s	0.005 s

Table 4.2: Time steps for the integrators used. The adaptive capability of the Runge-Kutta integrator results in a variable time-step that is set to ensure a predefined condition for numerical accuracy of the state variables being integrated. The value of the time step shown here is the average over the entire duration of the simulation.

In Figure 4.4, variation of Normalized Strain Energy during the maneuver with time integration using the adaptive Runge-Kutta integrator and the Generalized-α is shown .

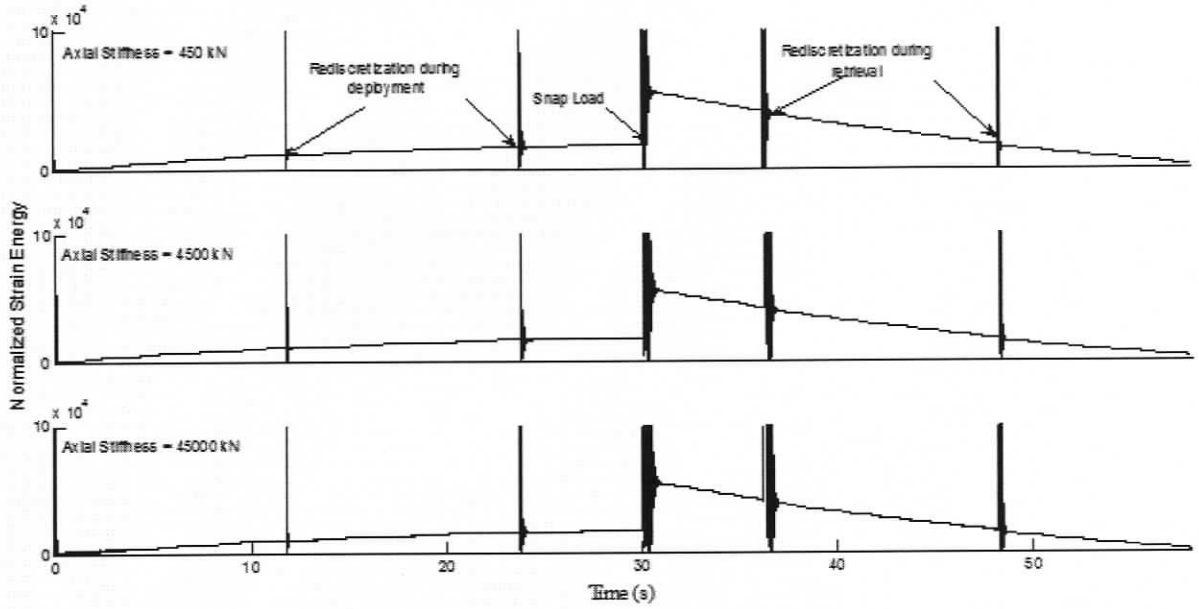

(a) Adaptive Runge-Kutta

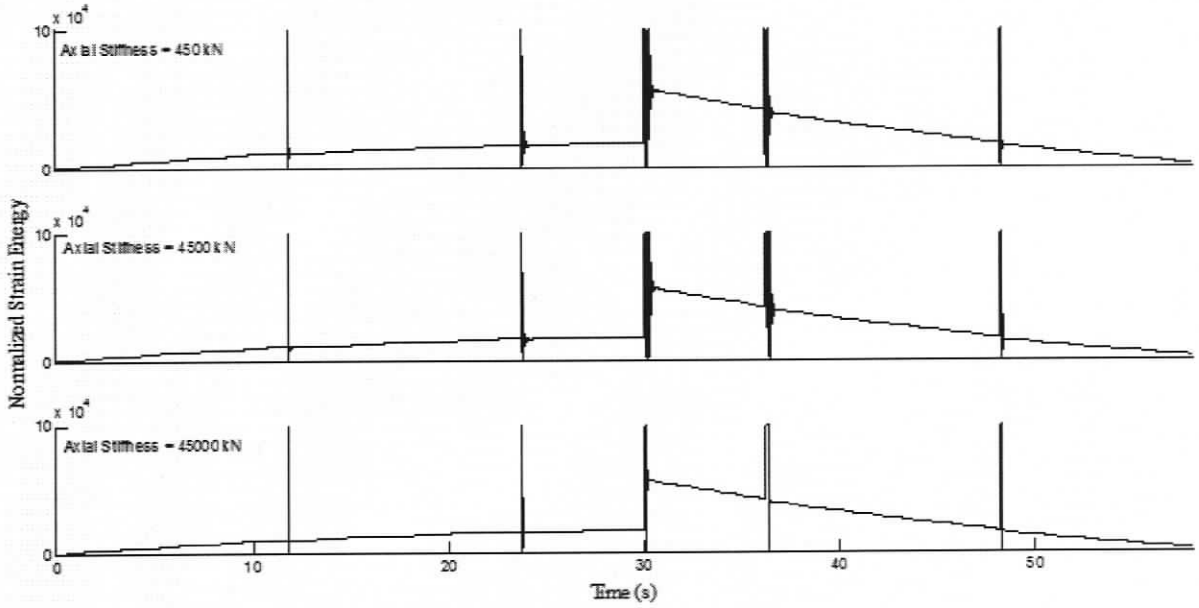

(b) Generalized-α

Figure 4.4: Variation in Normalized Strain Energy (a) using the Adaptive Runge-Kutta Integrator (b) using the Generalized-α Integrator.

It is seen in Figure 4.4 that spikes in strain energy occur during rediscretization during the deployment phase when an element is added to the cable assembly in the water and when an element is removed from the cable assembly during retrieval. Although the spikes in strain energy (curtailed in Figure 4.4) are of the order of 10^6 N^2m, the normalized energy varies as the square of the tension, and hence the axial stiffness, EA, which is of the order of 10^6 N. Consequently, the peak fluctuation in the element strain is of the order of 10^{-4} which is small. Whereas the normalized strain energy is conserved during a rediscretization step, it is not conserved for the snap load at the 30 second instant, when the deployment is reversed to retrieval.

It is seen that the strain energy profiles produced by the two integrators for the tethers with axial stiffness of 0.45×10^6 N and 4.5×10^6 N are nearly identical. However, for the stiffest cable, having an axial stiffness of 45×10^6 N, the variation in normalized strain energy during the rediscretization steps is quite different for the two integrators. A close-up of this variation for the first rediscretization step during cable retrieval is shown in Figure 4.5 below.

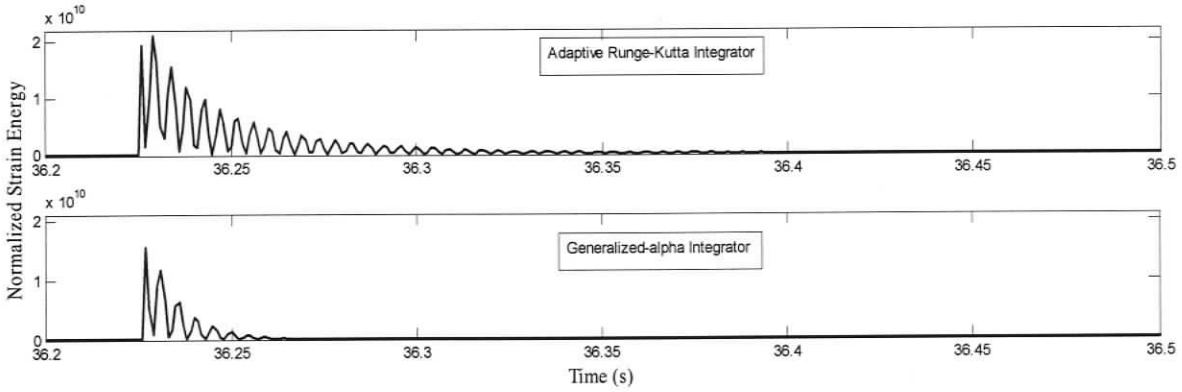

Figure 4.5: The effect of algorithmic damping of the Generalized-α integrator on the strain energy profile for the stiffest cable considered (axial stiffness 45×10^{6} N). The high frequency modes in this stiff cable are dissipated by the implicit integrator.

As described in Section 4.4, the Generalized-α integrator processes optimal numerical dissipation. It dissipates the highest frequency modes, while leaving the lower frequency modes unaffected In the case study considered here, the Generalized-α integrator has a time step of 0.005 s, and a spectral radius of 0.1. For these algorithmic parameters, the integrator successfully attenuates the high frequency changes in normalized strain energy occurring in the stiffest tether without affecting the lower frequency changes in the strain energy profiles for the less stiff tethers considered. This illustrates the effect of the optimal algorithmic damping of the implicit Generalized-α integrator.

The spike in the strain energy variation at the rediscretization step during deployment can be explained by the fact that a new element is introduced into the cable assembly at this stage. Consequently, the cubic spline profile of the spatially discrete cable is reset, resulting in a

momentary incorrect placement of the new node causing an increase in tension which is calculated explicitly from the node positions as described in Chapter 2.

At the rediscretization step during retrieval, an element is removed from the spline. The size of the element removed is shown to have an impact on the strain energy variation. When a large element is suddenly removed from the cable assembly, a jump in strain energy results. This can be reduced by lowering the length of the element removed at rediscretization during retrieval. This is shown in Figure 4.6.

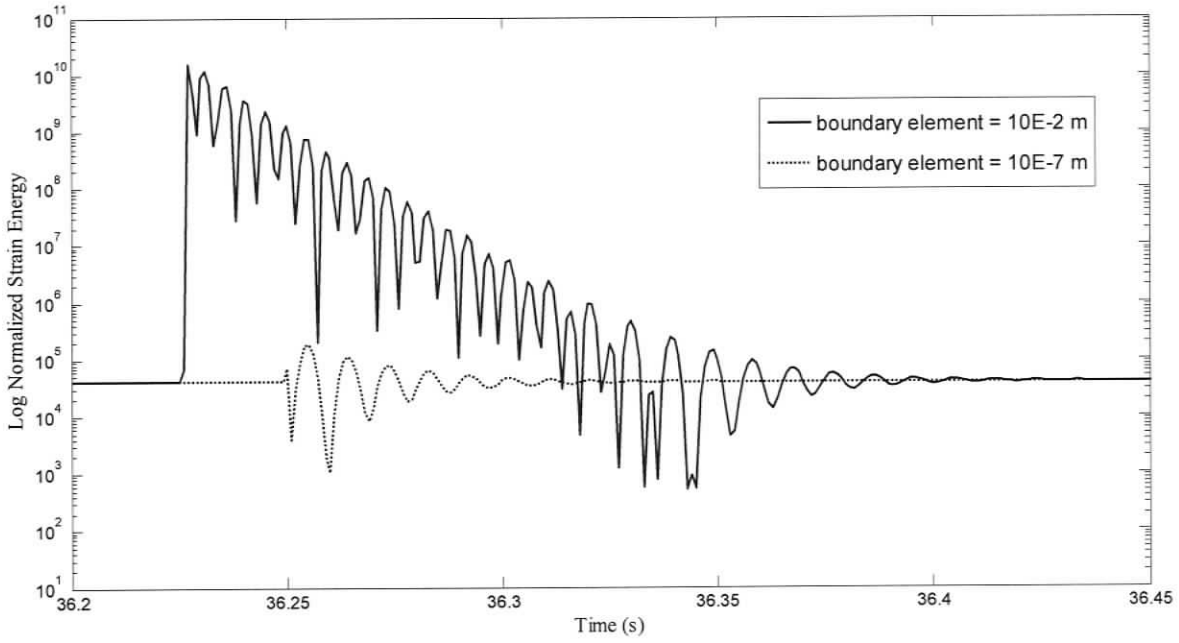

Figure 4.6: The use of a very short element with the Generalized-α integrator results in a significant reduction in the spike in the Normalized Strain Energy.

In the above, a very short boundary element of length 10^{-7} m was used with the Generalized-α integrator to realize significant improvement in the accuracy of the simulation during the rediscretization step. This short element introduces high frequency modes of

motion in the tether dynamics, and causes a numerical instability when used in conjunction with the adaptive Runge-Kutta integrator, making this level of accuracy unattainable. Hence, the high frequency dissipation capability of the Generalized-α integrator allows use of this short boundary element to improve the accuracy of the time domain simulation of cable retrieval.

4.6.2 Rapid Deployment of Low Tension Tether.

Here, the deployment of a slack cable is considered. The cable properties are listed in Table 4.3.

Property	Value
Tether Diameter	0.03332 m
Initial Cable Length (L_{TOT})	5.0 m
Torsional Rigidity (GJ)	1.00 Nm^2
Bending Stiffness (EI)	11920 Nm^2
Axial Stiffness (EA)	4.5×10^6N
Viscous Damping Coefficient (C_{ID})	437 Ns
Tether Density (ρ_c)	1025.0 kg/m^3
Water Density (ρ_w)	1025.0 kg/m^3

Table 4.3: Properties of Slack Tether being deployed.

The initial condition prior to deployment is shown in Figure 4.7

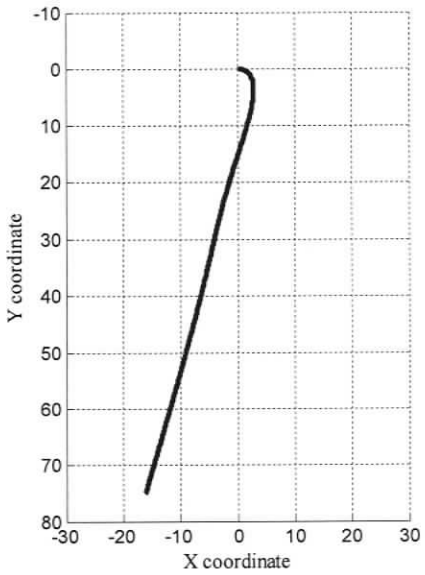

Figure 4.7: Initial Profile of the slack cable. It is on the surface of the water, contained in the inertial XY plane.

The initial profile of Figure 4.7 is for the cable in static equilibrium in quiescent water. Initially it consists of 4 elements, each 20 m long. The positions of the nodes in the inertial XY coordinate system is listed in Table 4.4

Node Number	X coordinate (m)	Y coordinate (m)
1	-0.5208	17.2007
2	-5.5293	36.4924
3	-10.6116	55.8296
4	-16.1115	75.0579

Table 4.4: Node positions in the initial cable profile.

Deployment is carried out at a rapid rate of 1 m/s over a period of 60 s. The adaptive Runge-Kutta integrator is used for the slack cable. As mentioned before, it is necessary to rediscretize the cable assembly during the deployment. For this, the greatest permissible length of the variable length boundary element needs to be prescribed. Towards this end, a convergence analysis was carried out for various cut off lengths of the boundary element. The parameter tracked during the convergence analysis was the Y coordinated of Node 1. The results for various boundary element lengths is shown in Figure 4.8

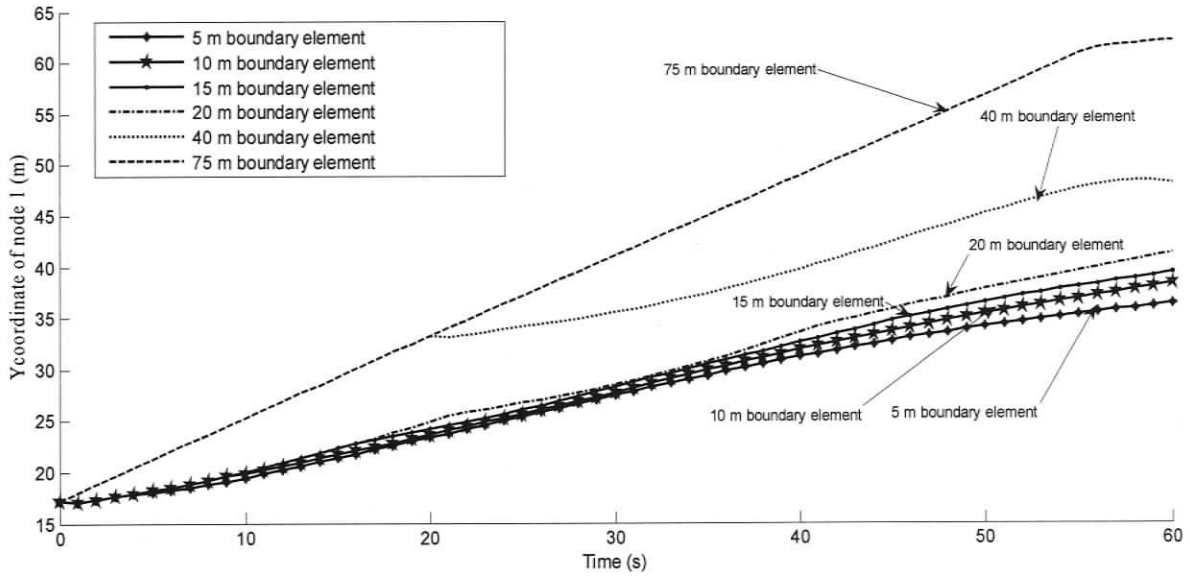

Figure 4.8: Convergence analysis for boundary element length during rediscretization of the cable being deployed. Larger boundary elements result in reduction of the accuracy of the simulation.

From the results of the convergence analysis, it is noted that the spatial resolution of the dynamics degrades as the allowable length of the boundary element increases. However, using very small length elements would increase the total number of elements in the mesh.

This increases the computational cost of the simulation due to larger memory requirement, and increased execution time for the larger number of rediscretization steps associated with the shorter elements. Consequently in this work, the maximum allowable boundary element length is taken to be 10 m as a compromise between accuracy and computational cost. The profile of the cable after 60 s of payout at a rate of 1 m/s is shown in Figure 4.9

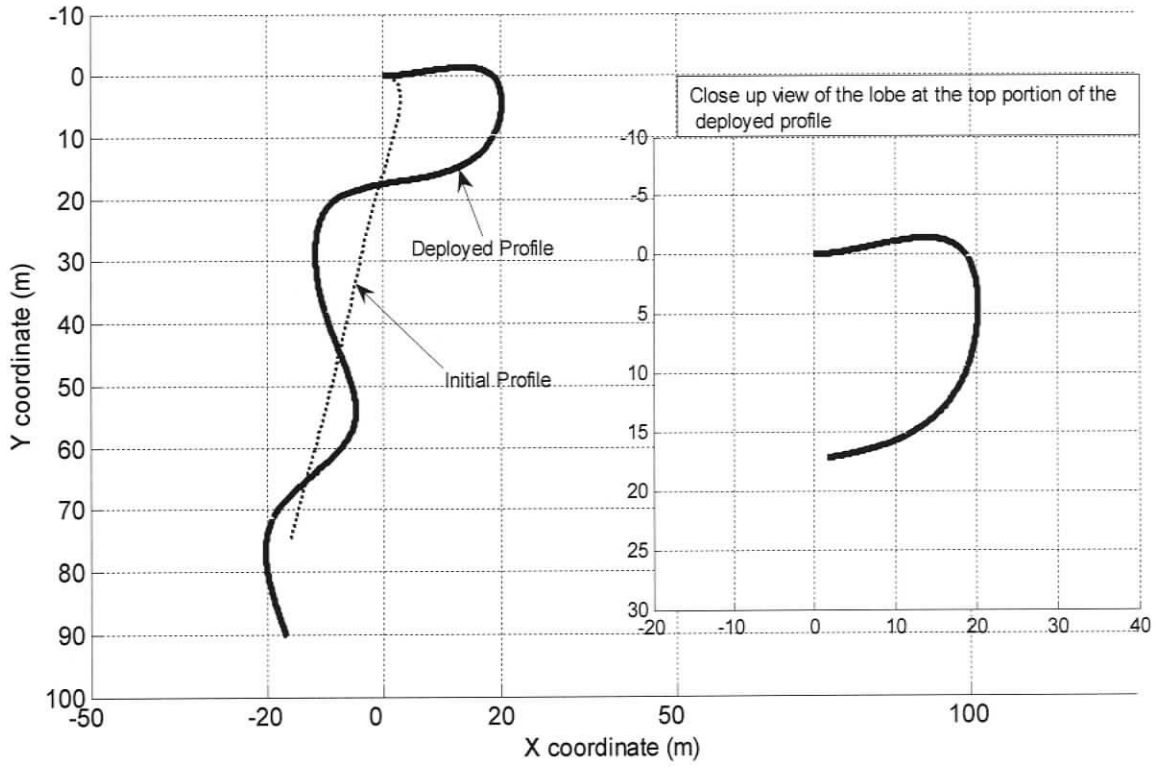

Figure 4.9: Deployment of slack cable. The inset shows the development of a lobe near the deployer, which represents cable accumulating close to the deployer in the absence of tension to take up the excess slack cable being introduced from the winch.

As seen in Figure 4.9 above, the motion of the tip of the slack cable does not follow the deployment schedule. In the absence of tension to take up the newly deployed cable, a lobe forms close to the deployer. This is consistent with practical experience from deployment of slack cable, and in the variable length tether dynamics simulation is a consequence of confining the variable length effects close to the deployer. This demonstrates the outcome of using the Eulerian approach described in Chapter 3 with the increase in length restricted to a single element at the boundary of the deployer and the span of cable in the water.

4.7 Closure

This chapter completes the dynamics model for variable length cable modeling, by presenting the time domain integration of the spatially discrete dynamics formulation developed in Chapter 3. The model has been shown to satisfactorily simulate the deployment and retrieval of tether in both low and high tension states. The effect of numerical dissipation on the strain energy profile of stiff cables has been highlighted. The rediscretization scheme presented here provides a means of maintaining the integrity of the simulation by constraining element lengths. As seen from the plots of strain energy conservation, it is clear that the rediscretization of the element assembly leaves no footprint on the tether mechanics being simulated. Having developed a numerical model for the time domain simulation of variable length tether dynamics, the next chapter deals with the implementation of the model to the dynamics modeling and control system simulation of an actual tethered underwater vehicle. A control system for the positioning of an underwater point on the tether of the

Remotely Operated Platform for Ocean Sciences (ROPOS), operated by the Canadian Scientific Submersible Facility (CSSF) is investigated in the next Chapter.

Chapter 5

A Position Regulator for the ROPOS Liveboating Configuration

5.1 Overview

In the previous Chapters, a time domain simulation was developed to model the dynamics of the variable length flexible tether of Remotely Operated Vehicles. An existing fixed length tether dynamics model developed by Buckham et al [11] was augmented to handle the changing tether length. Time domain simulations in the previous Chapter indicate the utility of the model in simulating the deployment and retrieval of tether at low and high tension states. In this Chapter the dynamics model is used to investigate a control system to regulate the position of a submerged point, called the control node, on the tether of an underwater vehicle system, the Remotely Operated Platform for Ocean Sciences (ROPOS) operated by the Canadian Scientific Submersible Facility (CSSF). The Chapter is organized as follows. Sections 5.2 and 5.3 provide a description of the robotic vehicle and the tether linking it to the surface deployer. The computational dynamics simulation of the coupled tether-vehicle system brings out the objective of regulating the position of the control node to reduce the cable disturbance force on the vehicle. Section 5.4 provides a background to the position control system design by presenting a reduced order model of the ROPOS system. The need for

decoupled longitudinal and depth controllers is shown due, to the different time scales of the dynamics. Sections 5.5 and 5.6 describe the Dahlin control system which is well suited for the design of the longitudinal position regulator. Section 5.7 presents the design of the Dahlin controller for the ROPOS system. The decoupled positioning system consisting of the Dahlin controller for longitudinal positioning and PD controller for depth regulation is described in Section 5.8. In Section 5.9, the position regulation system is applied to study the step response of the full ROPOS system. Section 5.9 demonstrates the effective regulation of the control node position, when the system is subjected to an ocean current. It is shown that position regulation of the control node brings about a significant reduction in cable disturbance on the vehicle in the face of the ocean current.

5.2 Background to the control system design.

In this section, the system being controlled, the Remotely Operated Platform for Ocean Sciences (ROPOS), is described. The coupled dynamics model of the tether and vehicle dynamics is presented.

5.2.1 The Remotely Operated Platform for Ocean Sciences (ROPOS)

The ROPOS system consists of two elements:

1. A vehicle or robotic platform equipped with end-effectors and vision systems.

2. A fiber optic tether linking the platform underwater to the deployer vessel on the surface, and serving as a conduit for power and telemetry for control of the robotic platform from the surface.

The robotic platform shown in Figure 5.1 is an Electro-Hydraulic Work Class HySub ROV produced by International Submarine Engineering of Port Coquitlam, B.C.

Figure 5.1: The ROPOS robotic platform.

The vehicle is linked to the surface vessel through an armored flexible tether. The properties of the tether are summarized in Table 5.1 below.

Property	Value
Tether Diameter	0.0254 m
Axial Stiffness (EA)	2170 kN
Bending Stiffness (EI)	9.0 Nm^2
Torsional Rigidity (GJ)	14.4 Nm^2
Viscous Damping Coefficient (C_{ID})	437 Ns
Tether Density (ρ_c)	4003 kg/m^3

Table 5.1: Properties of the ROPOS tether

The initial configuration of the tethered ROPOS system is described below. The service depth of the vehicle is around 2100 m. The vehicle operates in liveboating mode: it is linked directly to the winch on board the deployer ship with no intermediary garage or cage, as was shown in Figure 1.2 (b). The total length of the tether is 2371 m. The lower half of the ROPOS configuration is shown in Figures 5.2 (a) and (b).

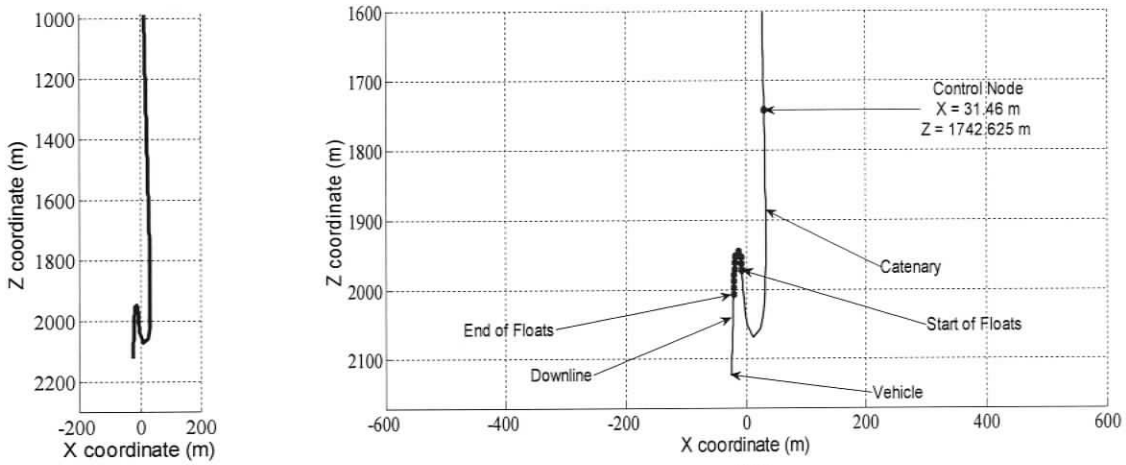

Figure 5.2 (a) Lower half of the initial tether profile. The upper portion continues to the deployer. (b) Close-up view of the floated section of tether close to the vehicle.

Figure 5.2: Configuration of the ROPOS system. The section with floats is shown in Figure 5.2(b). The floats attached to the tether form a lazy wave configuration to minimize the disturbance on the vehicle. The control node, whose position is regulated, is shown in Figure 5.2 (b).

The tether is required to be in a state of low tension close to the vehicle to isolate it from disturbances originating at the surface. This is achieved by attaching floats to a section of the tether close to the vehicle. The tether profile is essentially straight except

for a lazy wave near the vehicle formed by the series of football floats. The seven floats are attached over a 100m section that begins at the curvilinear coordinate $s = 2154$ m. Each float provides a buoyant force of 500 N. The section of tether with floats close to the vehicle is shown in Figure 5.2 (b). A catenary, or sag, of cable extends between the point $s = 1742.6$ m and the start of the floated section of tether. This weight of this catenary acts to depress the tether being suspended from the ship.

The spatially discrete tether model consists of 187 elements. The element lengths are shown in Table 5.2 below.

Element	Length (m)
1 to 50	5
51 to 151	18.5
152 to 176	9
177 to 187	2.5

Table 5.2 : Element Lengths in the spatially discrete ROPOS system.

5.2.2 Dynamics Simulation of the Coupled ROPOS System.

The ROPOS system simulation is composed of the two nonlinear dynamics models. The first is the tether dynamics model developed in this work, and the second is a nonlinear model of the robotic platform itself. The platform model was previously developed and is described in Steinke [28]. The vehicle was treated as a rigid body and the hydrodynamic drag coefficients were determined from empirical data. The thrust capability of the ROPOS vehicle resulting from one heave, one lateral, and two surge

thrusters was modeled. Within the simulation, a virtual pilot was implemented. The pilot emulated the human inputs to the ROV thrusters to drive the robotic platform over prescribed trajectories for specified maneuvers using a way-point navigation scheme.

The state of the ROV tether is given by the assembled vector of node positions as described in Chapters 2 and 3. The final node position is taken from the ROPOS dynamic model's state information: using the position and orientation information, the tether terminations location and orientation is calculated.

To evaluate the node curvatures, and complete the element geometries, the continuity equation (2.25) of Section 2.2.3 is evaluated. The tether termination at the vehicle is fixed and the slope of the last or N^{th} cable node $\mathbf{r}'^{(N)}$ is specified based on the vehicle state. Using the node positions, velocities, and curvatures in the last element, $\mathbf{r}^{(N-1)}, \dot{\mathbf{r}}^{(N-1)}, \mathbf{r}''^{(N-1)}, \mathbf{r}^{(N)}, \dot{\mathbf{r}}^{(N)}$, and $\mathbf{r}''^{(N)}$ the tether force on the termination is calculated as:

$$\mathbf{F}_{tether} = -\left(\left\{\left[\mathbf{K}_A\right]_N + \left[\mathbf{K}_B\right]_N + \left[\mathbf{K}_T\right]_N\right\}\mathbf{X}_N + \mathbf{H}_N + \mathbf{W}_N\right) \tag{5.1}$$

Where $\left[\mathbf{K}_A\right]_N, \left[\mathbf{K}_B\right]_N, \left[\mathbf{K}_T\right]_N$ are the assembled axial, bending and torsional stiffness, defined in Chapter 2 matrices for the last element. $\mathbf{X}_N$ is the vector of generalized displacements for the last element, and $\mathbf{H}_N, \mathbf{W}_N$ are the hydrodynamic and buoyancy load vectors for the last element. In addition to the force, the tether also exerts a bending moment and torque on the vehicle. The net tether moment is given by:

$$\mathbf{M}_{tether} = -\left(EI\kappa_N\hat{\mathbf{b}}^{(N)} + GJ\tau_N\hat{\mathbf{t}}^{(N)}\right) \tag{5.2}$$

Where EI is the bending stiffness of the tether, κ_N is the curvature of the last element, $\hat{\mathbf{b}}^{(N)}$ is the binormal vector at the bottom node or the tether termination point, GJ is the

torsional rigidity of the tether, τ_N is the twist of the last element and $\hat{\mathbf{t}}^{(N)}$ is the tangent vector at the bottom node of the tether.

The ROPOS system simulation structures the ROPOS and tether dynamics evaluations to enable this coupling. The two state vectors are assembled and passed to a single integrator to obtain the time domain simulation of the coupled tether-vehicle system. In the tethered ROPOS configuration simulated, the vehicle initially has no yaw, pitch or roll angles.

5.3 Problem Description.

A common ROPOS maneuver is station-keeping. Station-keeping forms an important part of the ROV operation. Typically the vehicle is stationed at a desired location or set-point and the manipulator performs the commanded tasks. In the dynamics simulation for the station-keeping maneuver, the virtual pilot acts to point ROPOS to the set-point and drive back towards the set-point. In the field operation, the system is subjected to ocean currents. In this case, the vehicle experiences disturbance forces not only due to the hydrodynamic forces accumulated over the ROPOS chassis itself, but also due to the drag accumulated over the tether.

Figure 5.3 shows the displacement, from the initial position, of the control node shown in Figure 5.2 (b), when uniform ocean current of 0.5 m/s (1 knot) is directed in the negative inertial X axis on the station-keeping ROV system.

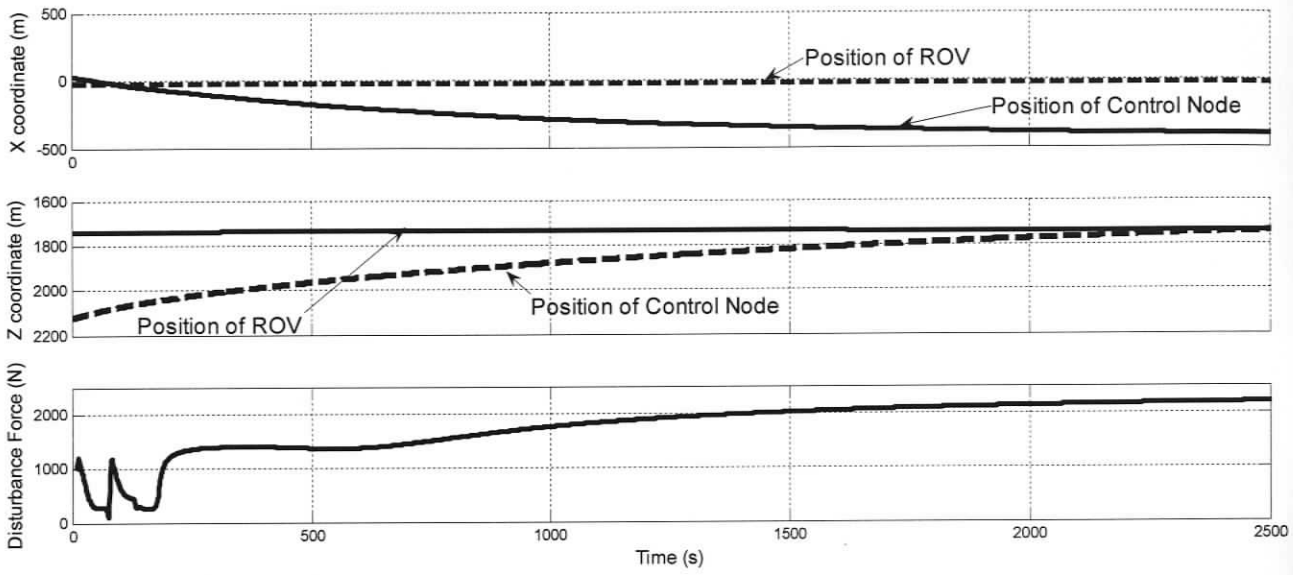

Figure 5.3: Effect of ocean current on the ROV station keeping maneuver. The current causes a significant excursion of the control node in the X direction. The low heave thrust capacity of ROPOS results in the inability to hold its vertical position. The disturbance force shown is the resultant of the X and Z components of the tether disturbance force at the tether termination point on the vehicle. The initial variation in disturbance force is due to the flipping of the tether profile within the first 500 seconds, as shown in Figure 5.4.

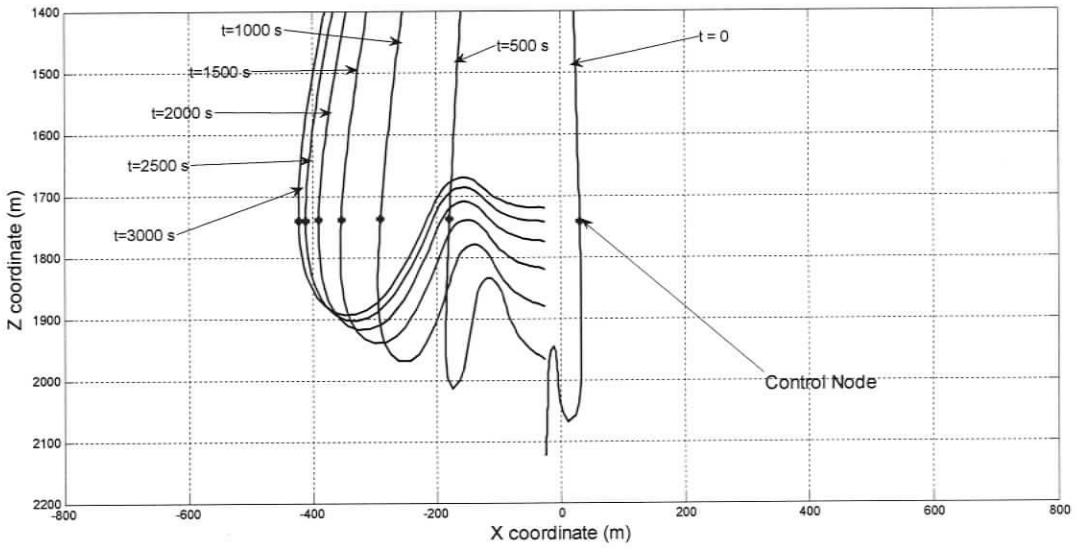

Figure 5.4: Evolution of the cable profile with time when it is subjected to a 1 knot ocean current. The tether profile flips into the current within the first 500 seconds. The control node displays a large excursion in the X direction, but little depth change. The limited heave thrust capacity of the vehicle causes it to rise upwards.

It is seen that the cable undergoes a large displacement from its equilibrium position due to the ocean current, which would cause it to exert a disturbance force on the station-keeping vehicle. This force must be countered by the vehicle thrusters. The ROPOS thruster capacity used in the dynamics model is listed in the Table 5.2.

Thruster	Capacity in Forward Direction (N)	Capacity in Reverse Direction (N)
Lateral	2200	1600
Heave	650	650
Surge – port	2200	2200
Surge – starboard	2200	2200

Table 5.3: Thrust capacity of ROPOS used in this work. The surge thrusters are used in differential mode to produce the yaw moment to align the nose of the vehicle into the current.

The thrust capacity of the ROV is limited. It is seen that the low heave thrust capacity of the vehicle causes it to rise under the influence of the floats. It is hence desirable to minimize the tether disturbance force as far as possible, in order to make the station-keeping of the vehicle easier.

In the preceding, no use was made of the surface deployer vessel and the winch bearing the tether to assist in the station-keeping. It is envisioned that if the position of the control node could be regulated in the inertial XZ plane with the ship providing surge motion along the X axis, and the winch providing depth or Z axis regulation, the disturbance force of the cable on the vehicle could be reduced. This is the rationale behind the position control system investigated in this Chapter.

5.4 Design of the Position Control System

The portion of tether between the control node and ROPOS is primarily motivated by the ROPOS thrusters. Hence, for the positioning of the control node using the ship and

the winch, this portion of the tether is modeled as a sphere, or clump weight placed at the control node, as shown in Figure 5.5. This reduced order model is used for the synthesis of the control node positioning system.

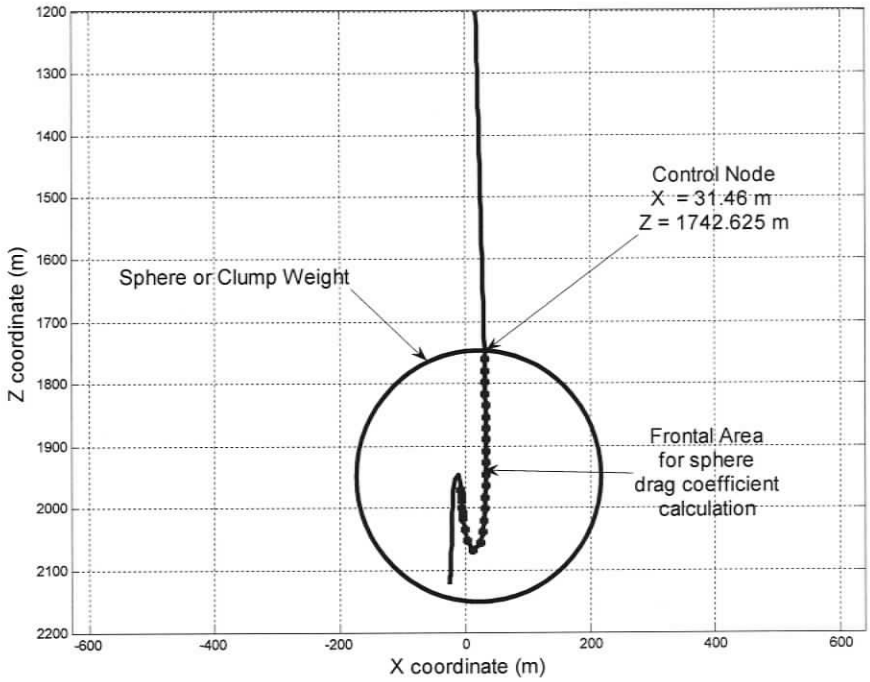

Figure 5.5: Reduced order model for the ROPOS controller synthesis. The steel clump weight shown is used to replace the span of cable between the control node and the vehicle. The mass of the clump weight is obtained from static equilibrium calculations, and is equivalent to the static tension in the cable at the point where the weight is introduced. The equivalent drag coefficient is obtained to match the hydrodynamic drag of the frontal area of the cable being replaced as shown.

The equivalent diameter d_s of the steel clump weight is obtained by equating it to the static cable tension in the portion of the tether being replaced. Hence, the following equality results:

$$(\rho_s - \rho_w)\left(\frac{4}{3}\pi\frac{d_s^3}{8}\right)g = (\rho_c - \rho_w)LA_c g - N_{float}F_{float} \tag{5.3}$$

where,

ρ_s = density of steel = 11320 kg/m^3
ρ_w = density of water = 1025 kg/m^3
ρ_c = density of cable = 4003 kg/m^3
g = gravity = 9.8 m/s^2
L = nominal length of tether being replaced = 602 m
A_c = cross sectional area of the cable = 5.066×10^{-4} m^2
N_{float} = number of floats = 10
F_{float} = buoyant force of each float = 500 N

The above calculation gives the diameter of the sphere d_s to be 0.42 m.

The equivalent hydrodynamic drag coefficient of the sphere C_{Ds} is obtained by compensating for the hydrodynamic drag of the tether being replaced. For this purpose, it is necessary to specify the projected area of the tether being replaced by the sphere. Here, this projected area is taken as the frontal area of the catenary, from the point of attachment of the sphere to the start of the floated section shown in Figure 5.5. The drag coefficient C_{Ds} is obtained from the relation:

$$C_{Ds}\left(\frac{\pi}{4}d_s^2\right) = C_{Dc}L_{catenary}d_c \tag{5.4}$$

where,

C_{Dc} = hydrodynamic drag coefficient of the cable = 1.650
$L_{catenary}$ = span of the catenary upto the first float = 405 m
d_c = diameter of the cable = 0.0254 m

For the diameter $d_s = 0.42\,m$ calculated previously, the hydrodynamic drag of the sphere is obtained as $C_{Ds} = 122.5$.

The synthesis of this controller is completed using this simplified representation of the ROPOS configuration. An acoustic position fix on the control node location is used to close the feedback loop. Next, the open loop step response of the system is considered for unit step input of surge or X motion of the ship, and vertical cable payout of the winch. In this work, the ship or deployer is modeled as a simple first order lag with a time constant of 50 seconds, although any suitable value could be adopted depending upon the dynamic response of the particular ship being considered. The transfer function relating the commanded and actual ship displacement along the X coordinate is given by:

$$G_s = \frac{1}{50s+1} \tag{5.5}$$

This ship transfer function was introduced within the computational dynamics simulation of the ROPOS system described in Section 5.2.2, and the simulation executed for a unit step input to the ship. Figure 5.6 shows the response of the control node to unit step input of surge motion commanded to the ship, and unit step of vertical cable payout rate from the winch mounted on the ship.

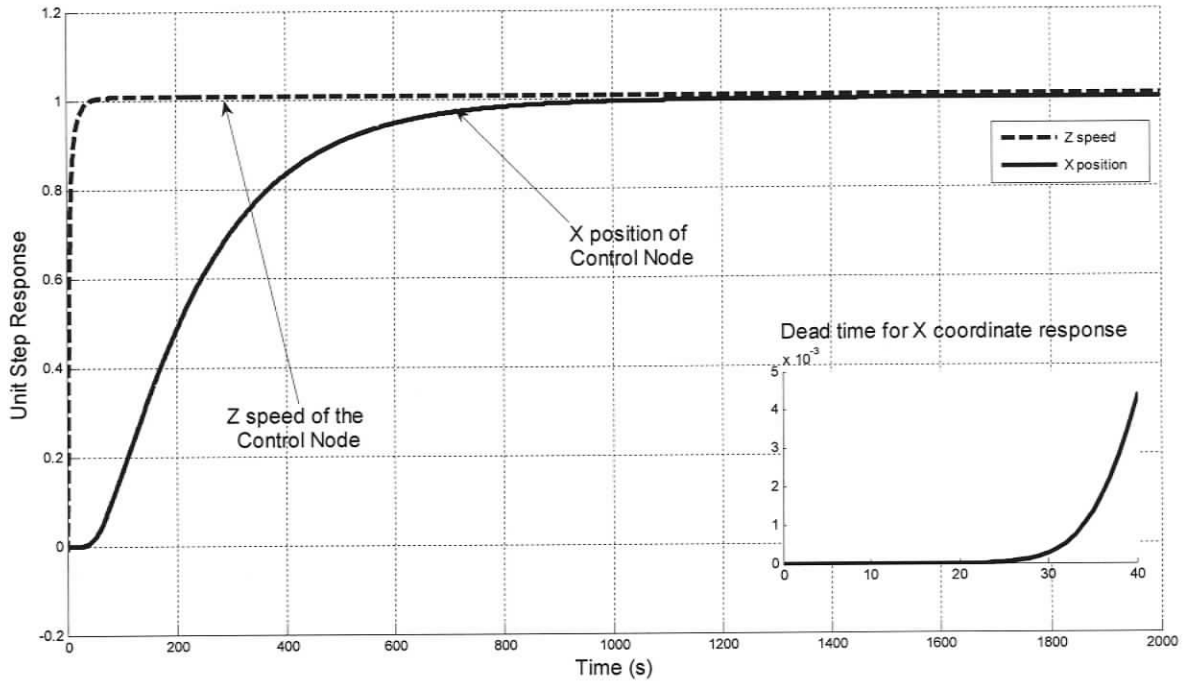

Figure 5.6: Response to unit step inputs in ship surge (X coordinate displacement input) and winch payout rate (speed in the Z coordinate). As can be seen, the speed of the control node rapidly adopts the speed of the winch payout. There is no dead time. On the other hand, there is a 25 second time delay before the control node begins to respond to a unit step surge motion of the deployer.

As can be seen, a 25 second dead time exists for the response of the control node to a longitudinal unit step displacement of the deployer, whereas the response to a unit step of winch vertical payout speed shows no dead time. It is well known that transverse motions propagate much more slowly in the submerged cable than motions along the vertical cable profile. This has been referred to as the water pulley effect (Kennedy [39]). As the surface ship accelerates forward, the cable tends to slide along its own profile and the bottom node initially moves vertically as seen in Figure 5.7.

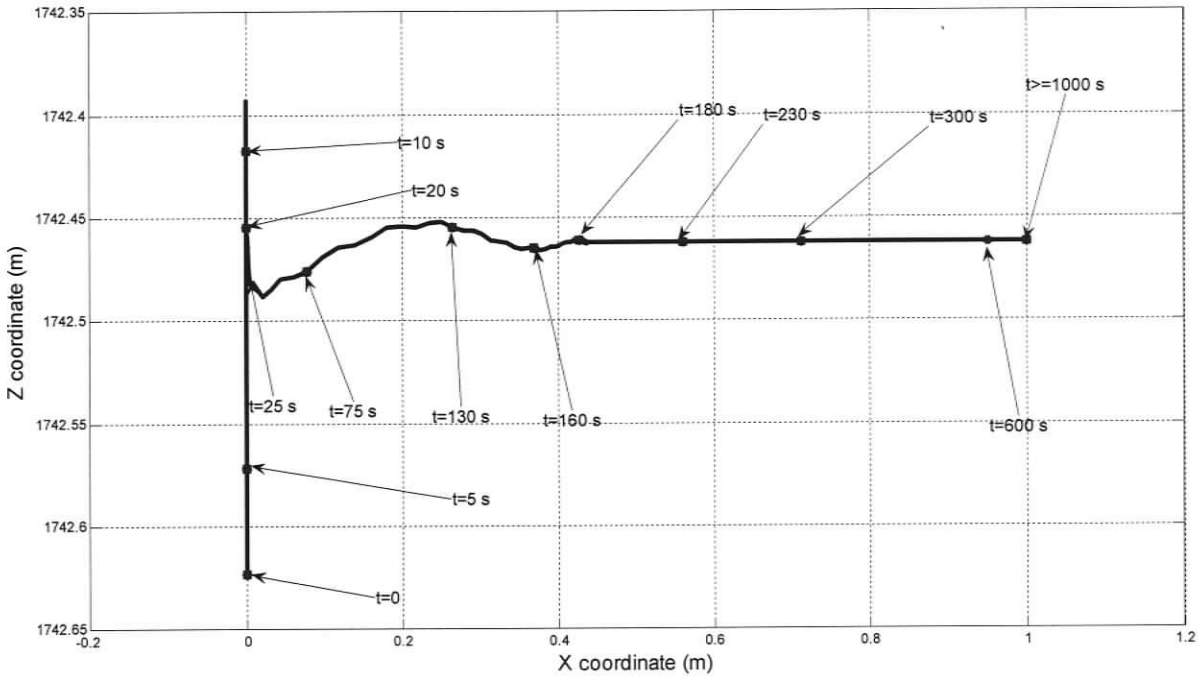

Figure 5.7: Path of the control node in time showing the water pulley effect. From the loci of positions, it is clear that the node rises through water column during the dead time. It is also seen that the response in X position begins from the 25 s instant onwards. This is consistent with the dead time observed in Figure 5.6

As a consequence, positioning of the X coordinate involves a time delay, or dead time, that is not present during depth regulation. Thus, the closed loop controllers for longitudinal and depth positioning must be decoupled and designed separately for the ROPOS system. For the depth or Z position control of the node, in the absence of any dead time, the well known Proportional-Derivative (PD) controller is used with the deployment/retrieval rate of cable at the winch serving as the control signal. For

longitudinal X positioning, a suitable closed loop feedback controller capable of handling significant dead time is investigated.

5.5 Design of the Longitudinal Positioning System.

For the longitudinal or X axis positioning of the control node, the system shows a large dead time or time delay as seen in Figure 5.6. Automatic control of a system with time delay involves making decisions based on state feedback that would be available a finite interval of time in the future (Smith [29]). This makes effective closed loop control for the X coordinate positioning of the control node a difficult problem. Kim et al. have shown that conventional PID controllers are not well suited for processes with large dead time [30] Triantafyllou and Grosenbaugh have used a Smith Predictor for closed loop positioning of an intermediary heavy cage within a two-body ROV system (Figure 1.2 (a)). However, the extent of the commanded motion was very limited – 10 m over a 20 minute maneuver [10]. As seen in Figure 5.3, the automatic controller must compensate control node motions of the order of hundreds of meters. In addition, the Smith Predictor is a continuous-time controller relying on continuous information of the control node position. In this work, we seek a suitable discrete time controller, since acoustic fixes on the control node position are available only at discrete instants of time. The Dahlin Controller is a frequently used discrete time controller for closed loop feedback control of plants with large dead times. It hence deserves consideration as a candidate for the longitudinal positioning system. A review of the Smith Predictor and the equivalence between the Smith Predictor and Dahlin Controller can be found in Appendix B.

5.6 The Dahlin Controller

Eric Dahlin [32] proposed a discrete time controller for systems with time delay in 1968. The Dahlin controller belongs to the family of direct Z-domain design algorithms. As the name indicates, these algorithms are designed for systems where the signals are sampled at discrete instants of time. Figure 5.8 shows a typical digital process loop.

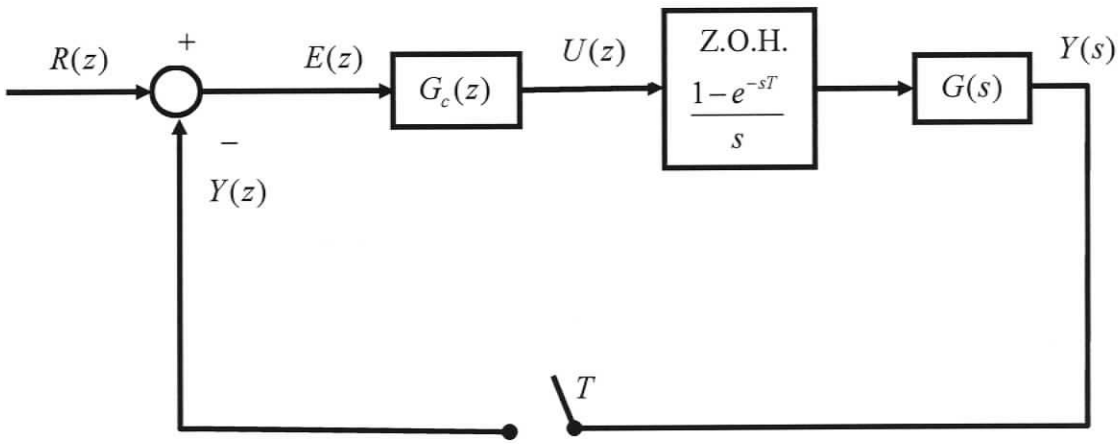

Figure 5.8: Digital Process Loop used for the design of the Dahlin controller. The continuous longitudinal dynamic response of the cable is contained within the plant transfer function $G(s)$.

In the above:

$R(z)$ is the commanded longitudinal or X position of the control node

$Y(z)$ is the actual X position of the control node sensed by the acoustic pinger, from a self contained emitter strapped onto the tether at the control node.

$E(z)$ is the error signal

$G_c(z)$ is the Dahlin Compensator

$U(z)$ is the control signal for the longitudinal positioning of the ship, which is converted into continuous form by passing it through a Zero Order Hold (Z.O.H.) as shown.

$G(s)$ is the continuous plant transfer function, which comprises of the ship dynamics (given by the transfer function $G_s(s)$ of equation (5.5)) in series with the longitudinal cable dynamics incorporating the dead time.

T is the sampling time for the system which is taken as 5 seconds for the Ultra Short Baseline (USBL) acoustic pinger used for the ROPOS system.

In the direct design methodology, the objective is to design the controller $G_c(z)$ in such a manner that a desired closed loop performance is obtained.

In the above system, the output signal is given by:

$$Y(z) = G(z)G_c(z)\left[R(z) - Y(z)\right] \tag{5.6}$$

Where $G(z)$ is the Z-transform of the continuous plant and the zero order hold, and is given by:

$$G(z) = \mathbf{Z}\left\{\frac{1-e^{-sT}}{s}G(s)\right\} \tag{5.7}$$

For a given desired overall closed loop transfer function $H(z) = \dfrac{Y(z)}{R(z)}$, the controller can be designed using the relation :

$$G_c(z) = \frac{Y(z)/R(z)}{G(z)(1 - Y(z)/R(z))} \tag{5.8}$$

The benchmark transfer function $Y(z)/R(z)$ is most commonly specified to satisfy two objectives, resulting in two different direct Z-domain control algorithms. These objectives are:

1. For the output to follow the input within one time step, that is to annihilate the time delay,

$$Y(z)/R(z) = z^{-1} \tag{5.9}$$

The resulting controller $G_c(z)$ from equation (5.8) for such a selection of $Y(z)/R(z)$ is referred to as the deadbeat controller.

2. For the overall closed loop transfer function to behave as a first order process.

$$Y(z)/R(z) = \mathbf{Z}\left\{\frac{1}{(\lambda s+1)}\right\} \tag{5.10}$$

In this case the Dahlin controller results. In equation (5.10), λ is the time constant of the first order model, and acts as an algorithmic tuning parameter. While this is the form of the benchmark transfer function for the classical Dahlin controller, Zhang et al [33] show that for systems higher than first order, it is preferable to apply a benchmark transfer function of the same order as the system being modeled. For an n^{th} order system, the Dahlin controller results from selecting

$$Y(z)/R(z) = \mathbf{Z}\left\{\frac{1}{(\lambda s+1)^n}\right\} \tag{5.11}$$

This simple design process yields a powerful control algorithm with inherent dead time compensation. It is used as the basis for the X coordinate positioning of the control node on the submerged tether in this work.

5.7 Design of the Dahlin Controller.

Having reviewed the theory of the Dahlin Controller, its design for the longitudinal positioning of the control node is taken up. The unit step response for the overall system consisting of the ship dynamics and the cable dynamics was shown in Figure 5.6. However as seen in Figure 5.4 , under the effect of ocean current, the control node displays excursions that are of the order of hundreds of meters. In this work, to account for these large motions of the control node, the controller is designed for a step of 50 m.

The 3 steps in the design of the Dahlin controller are:

Step 1 : Obtaining the open loop plant transfer function $G(z)$.

Step 2 : Selecting desired benchmark transfer function $H(z)$.

Step 3 : Applying the design equation (5.8) to obtain the transfer function of the Dahlin compensator $G_c(z)$.

5.7.1 Open loop plant transfer function.

The step response of the control node to a 50 m commanded step at the ship is shown in Figure 5.9.

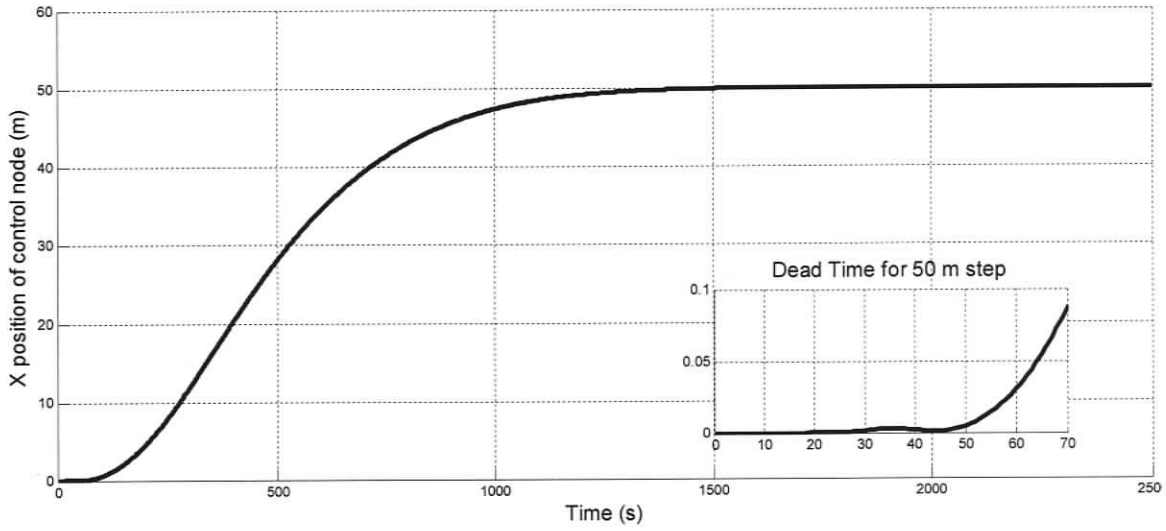

Figure 5.9: Response of the control node to a 50 m commanded step. As seen in the inset, the dead time is approximately 50 s, as opposed to 25 s for the unit step response of Figure 5.6.

As seen in Figure 5.9, the dead time can be taken to be 50 s. This is the response of the control node to a commanded 50 m step to the ship. The plant transfer function $G(s)$ is obtained by fitting a second order transfer function to the observed response of the control node in Figure 5.9. The parameter estimation technique of Smith [35] is used. A second order transfer function is defined completely by three parameters, the damping ratio ζ, the natural frequency ω_n and the dead time θ, and is of the form:

$$G(s) = \frac{e^{-s\theta}}{\frac{s^2}{\omega_n^2} + 2\zeta\frac{s}{\omega_n} + 1} \tag{5.12}$$

Based on a dead time of 50 s, as seen in Figure 5.9, the model transfer function is found to be:

$$G(z) = \mathbf{Z}\left\{\frac{e^{-50s}}{7.111\times10^{4}\mathrm{s}^{2} + 453.3s + 1}\right\} \tag{5.13}$$

Figure 5.10 shows the good agreement between the observed response and the response of the model transfer function.

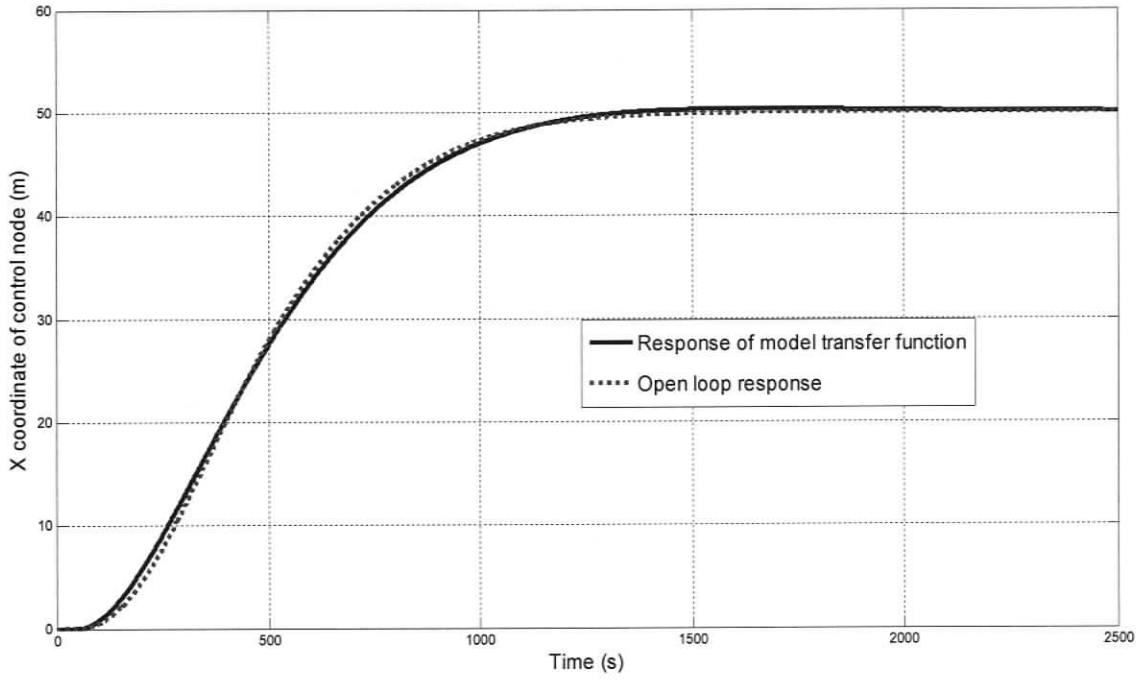

Figure 5.10: Good agreement is obtained between the observed 50 m open loop step response, and the second order fitted transfer function of equation (5.13).

5.7.2 Selection of the desired overall closed loop response

Having obtained an accurate model for the plant, the next step is to select a suitable benchmark transfer function $H(s) = Y(s)/R(s)$. Here, the approach of Zhang et al [33] is adopted to define

$$H(s) = \frac{Y(s)}{R(s)} = \frac{1}{(\lambda s + 1)^n} \tag{5.14}$$

where $n=2$ for the second order model transfer function. The tuning parameter λ is selected to be 100. This benchmark transfer function is selected to yield a faster response than the open loop uncontrolled response as shown in Figure 5.11.

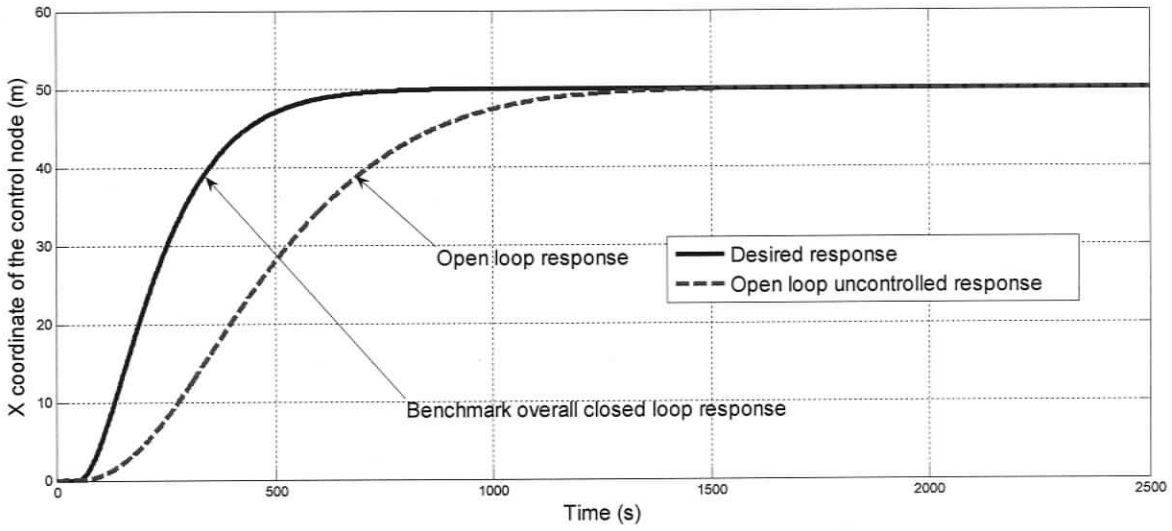

Figure 5.11: Benchmark open loop transfer function $H(s)$ used in the controller design. This choice is made to ensure that the controlled system provides a faster response than the open loop system.

5.7.3 Application of the Dahlin design equation.

The transfer function of the Dahlin compensator is determined using MATLAB, solving the design equation (5.8) with the expression for desired closed loop transfer function from equation (5.14) and plant transfer function from equation (5.13). Discretization of the continuous transfer functions requires the specification of a sampling time. The sampling time is determined from the update rate of the position pinger. ROPOS uses an Ultra Short Baseline (USBL) system for this purpose. The

corresponding sampling time is 5 seconds. The resultant Dahlin controller transfer function obtained in the discrete time Z-domain is given by:

$$G_c(z) = \frac{6.952 - 6.959z^{-1} - 6.501z^{-2} + 6.513z^{-3}}{1 - 0.913z^{-1} - 0.9775z^{-2} + 0.8953z^{-3}} \tag{5.15}$$

5.8 Decoupled longitudinal and depth controllers for ROPOS.

The design of the longitudinal or X coordinate feedback controller has been described in the previous Section. In order to position the node in the XZ plane, it remains to develop a controller to regulate the depth or Z coordinate of the control node. As has been discussed in Section 5.1, the surging motions of the cable produce a depth change of the control node through the water pulley effect. As seen in Figure 5.7, the depth change occurs during the initial dead time. To regulate the depth of the control node, an independent Proportional-Derivative (PD) control on the winch is implemented, with the deployment/retrieval rate acting as the control signal. The PD controller gains are tuned by simulation. Figure 5.12 shows the decoupled longitudinal and depth position control system.

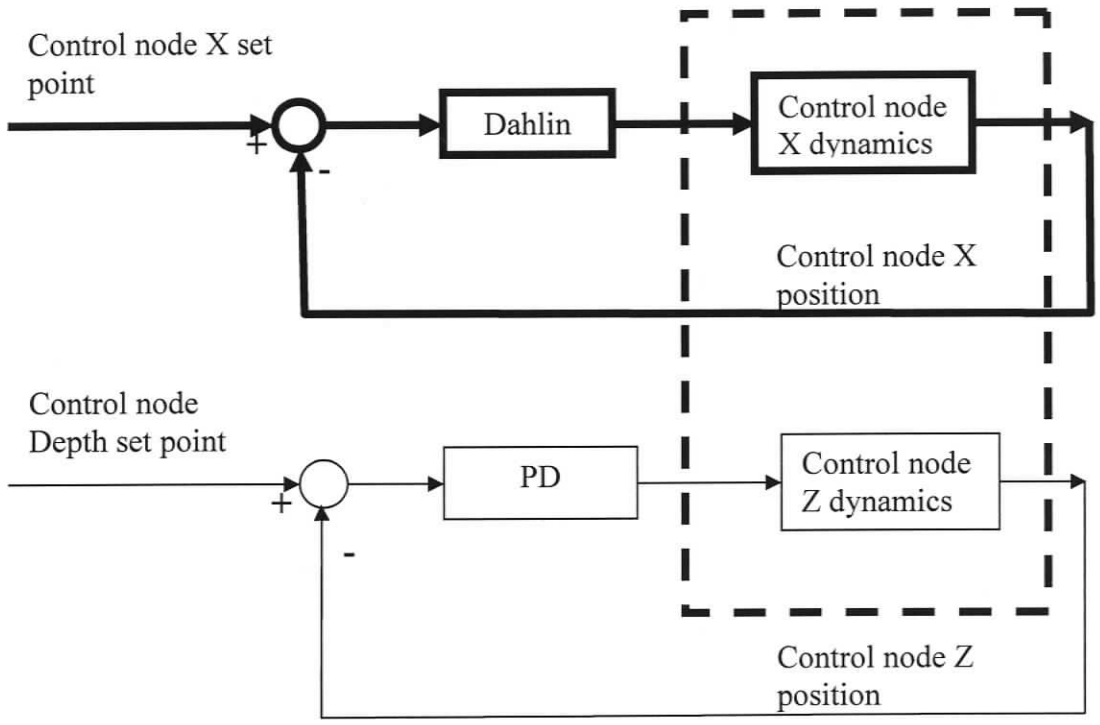

Figure 5.12: Decoupled longitudinal and depth controllers for positioning the control node in the XZ plane.

5.10 Application of the Controllers to the tethered ROPOS system.

The next step is to apply the controllers within the model of the actual ROPOS system, through the nonlinear tether-vehicle coupled simulation described in Section 5.2.2. The acoustic depth estimation system was used to ping the position of the control node. The X

coordinate of the control node was used as the feedback signal for the Dahlin Controller and the depth of the control node was used as feedback for the PD depth regulator.

The step responses of the control node for 50 m and 100 m commanded steps at the ship are as shown in Figure 5.13

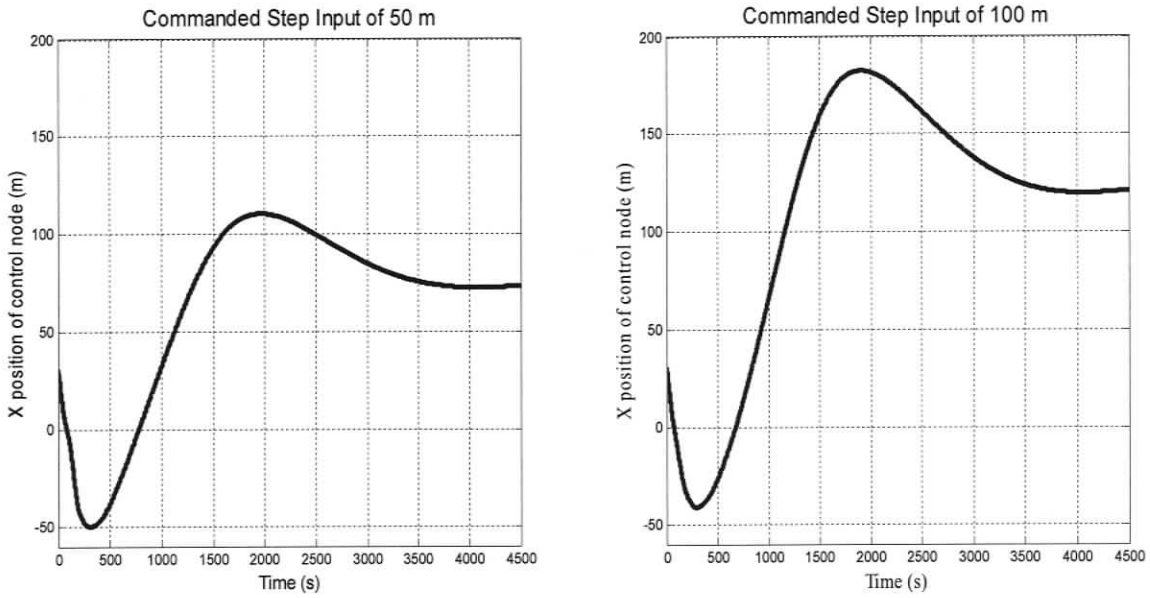

Figure 5.13: Step response of the control node for the longitudinal Dahlin Controller applied to the full ROPOS dynamics simulation. There is an increase in the delay time and overshoot in the response compared to the dynamic response expected when the controller was designed for the reduced order system described in Section 5.4.

It is seen from Figure 5.13 that the performance of the controller deteriorates when it is applied to the full nonlinear tethered ROPOS system. An increase in the dead time and an overshoot are observed. The discrepancies can be attributed to the fact that the linear controller design was carried out on the reduced order representation of ROPOS described in Section 5.4. The catenary, floated section and the vehicle were lumped into a

sphere or clump weight and the controller was designed assuming that all these constituents of the clump weight move like a rigid body. This condition however cannot be guaranteed as the ship accelerates in response to large commanded step inputs. For instance, it is seen in Figure 5.4 that the heave thruster of the ROV has a relatively small thrust capacity, and could rise up through the water column under the influence of the floated section of tether. Hence these unmodeled dynamics would interfere with the nominal dynamics of the reduced order system for which the controller is designed.

However, the primary objective of this work is not the positioning of the control node to commanded longitudinal ship motions. The decoupled controller designed here is intended to use a combination of ship motion and winch payout/payin to actively regulate the position of the control node during an ROV station-keeping operation to reduce tether disturbance on the vehicle. From this point of view, it is shown in Section 5.11 that the controller performs this task successfully.

The depth regulation is realized by the winch PD controller using the depth of the control node as the feedback signal and winch activity as the control signal. The parameters of the PD controller are listed in Table 5.3.

Sampling Time	5 s (same as the Dahlin Controller)
Proportional Gain	0.01
Derivative Gain	0.02

Table 5.4: Parameters of the PD depth regulator

The winch PD regulator is seen to successfully regulate control node depth in Figure 5.14. Since the majority of the depth regulation occurs during the initial dead time, there appears to be no interference between the longitudinal and depth controllers.

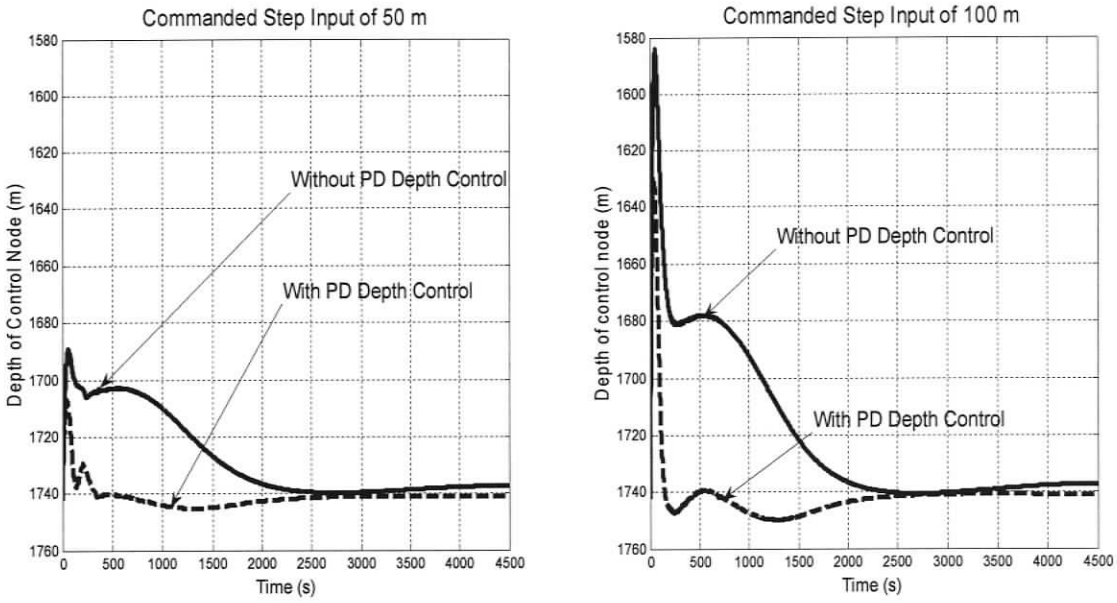

Figure 5.14: Depth regulation of the control node. As seen, the water pulley effect causes large depth changes, during the initial dead time, which increase with increasing magnitude of the longitudinal step commanded. The winch PD controller successfully reduces depth excursions of the control node.

5.11 Disturbance Mitigation for the ROPOS station-keeping maneuver.

Having developed the decoupled longitudinal and depth regulators, it remains to apply them to the ROPOS station-keeping maneuver. As discussed in Section 5.3, in the face of an ocean current, the control node gets blown towards a new equilibrium position, as shown in Figure 5.4. It was hypothesized that regulating the position of the control node

would reduce the tether induced disturbance force on the vehicle. In order to validate this hypothesis, the longitudinal and depth controllers are applied to the tethered ROPOS system for a station-keeping mission subjected to a steady ocean current of 0.5 m/s (1 knot) along the negative inertial X direction. The controllers endeavor to maintain the control node at its initial location of X= 31 m and Z = 1742 m throughout the station-keeping operation. The resultant controller action in regulating the control node position in the XZ plane is shown in Figures 5.15 – 5.17.

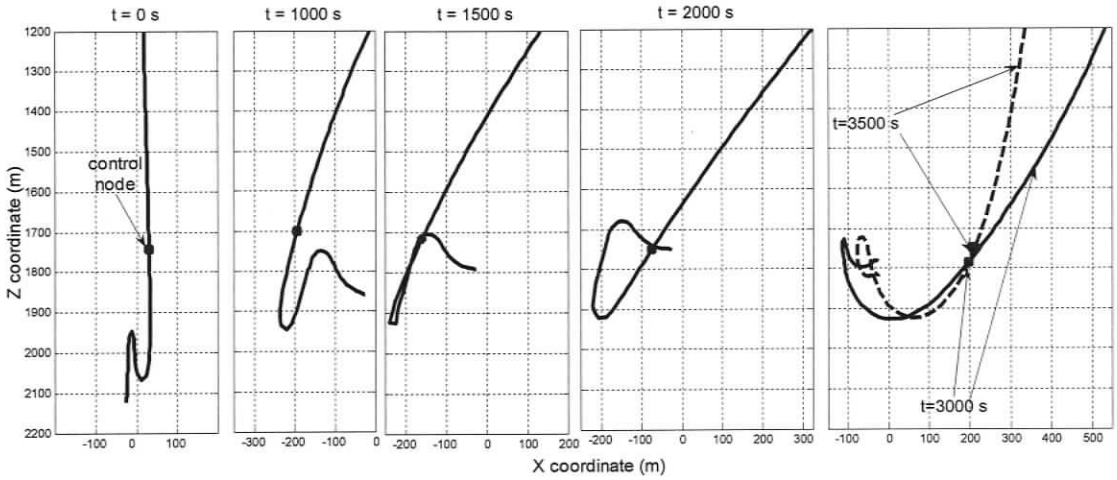

Figure 5.15: Time evolution of the cable profile during station-keeping. The decoupled control system prevents the excursion of the control node when subjected to the 1 knot current (Figure 5.4), by keeping it within a range of $X = \pm 200$ m and within 50 m of the original depth.

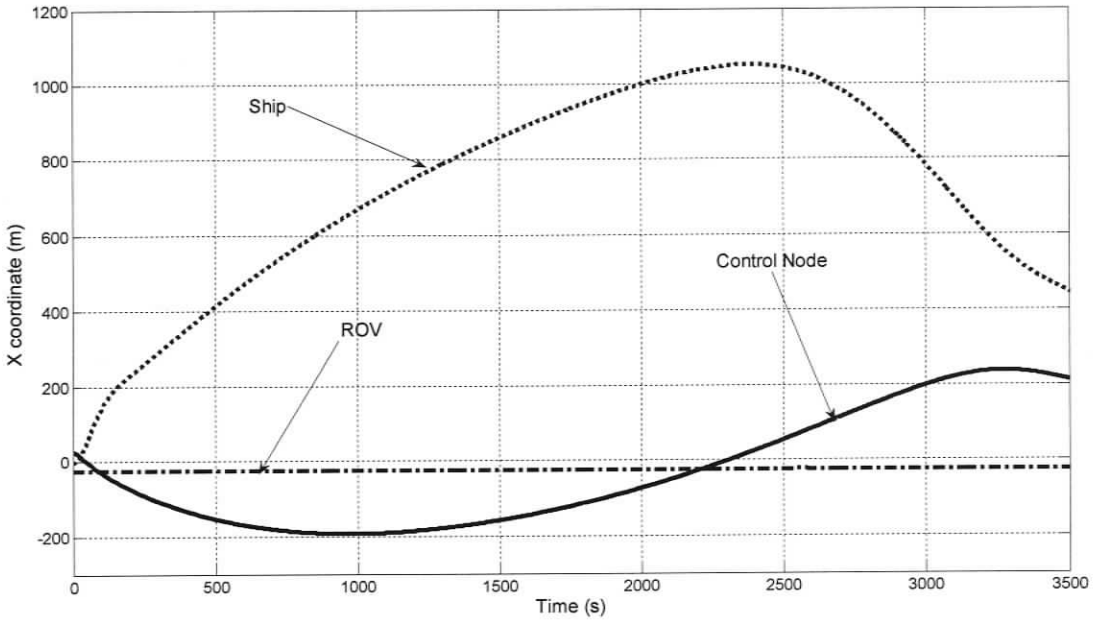

Figure 5.16: X coordinate regulation of the control node during ROV station-keeping. The control signal - the surge motion of the ship, is used to prevent the control node from getting blown away.

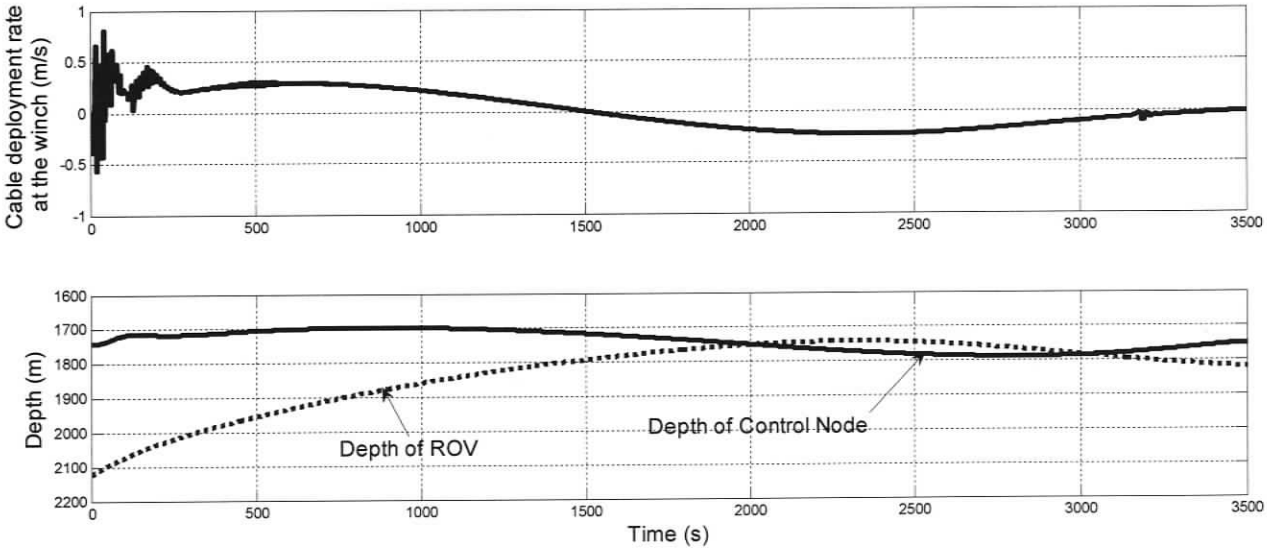

Figure 5.17: Regulation of control node depth. It is seen that the PD gains of Table 5.3 are selected to cap the deployment/retrieval rate at 1 m/s.

It is seen that the control node is maintained within a range of approximately of $X = \pm 200$ m and within 50 m of the target depth.

The resultant mitigation in tether disturbance force on the vehicle is shown in Figure 5.18

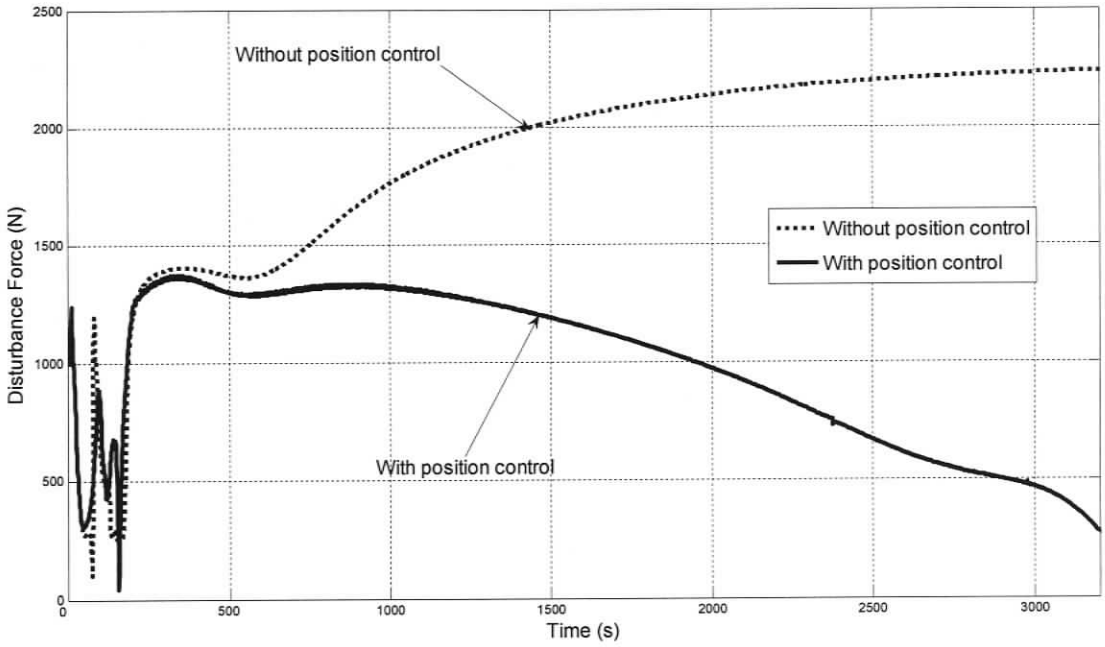

Figure 5.18: Disturbance Force reduction for 1 knot (0.50 m/s) of uniform ocean current. The cable disturbance force is reduced by up to a factor of 4 over the time domain. This shows the ability of the position regulation system to realize its primary objective of reducing tether disturbance force on the vehicle.

It is seen that the position regulation scheme developed here is quite effective in reducing the tether-induced disturbance force on the vehicle. The otherwise passive ship and cable winch are leveraged to realize the objective of reducing the tether disturbance force on the vehicle, which is a significant concern in ROV operation. One of the

distinguishing features of un-tethered underwater vehicles or AUVs is superior maneuverability in the absence of tether disturbances on the vehicle. By reducing the undesirable tether-vehicle coupling through the use of the position regulation system in this work, it may be possible to realize the superior maneuverability of a tetherless vehicle with the robustness of the human-in-the-loop controlled ROV, for station-keeping maneuvers. This additional capability is realized at the reasonable cost of tracking the position of the control node, which is in addition to the ROV at the bottom of the tether. This application demonstrates the utility of the dynamics model developed in this work for advanced ROV mission planning.

5.12 Closure

In this Chapter a decoupled control system for the XZ plane positioning of a submerged point on the tether, called the control node, has been developed. The Dahlin design methodology has been used to synthesize the longitudinal or X-coordinate positioning system. It is shown that the water pulley effect couples the longitudinal positioning with undesirable depth changes. A winch PD controller is demonstrated to successfully regulate the depth of the control node. The controller synthesis is carried out on a reduced order model of the Remotely Operated Platform for Ocean Sciences (ROPOS) system. The resulting controller is applied to a computational dynamics model of the fully nonlinear coupled ROPOS tether-vehicle system to realize significant reduction of tether disturbance forces during station-keeping of the vehicle in the face of an ocean current. This establishes the effectiveness of the dynamic positioning system developed.

Chapter 6
Conclusions and Future Work

6.1 Conclusions

In this work, a computational dynamics model was developed to simulate the dynamics of variable length underwater vehicle tether. The variable length model was based on an existing fixed length dynamics model with low tension capability and minimal state variable requirement described in Chapter 2. Consequently, the variable length model developed in Chapter 3, obtained by augmenting the fixed length model using Newton's second law for variable mass systems, inherited the virtues of this fixed length model. The ability of the model to simulate high and low tension cable dynamics was illustrated through time domain simulations of cable deployment and retrieval in Chapter 4.

Chapter 5 demonstrated a practical implementation of the dynamics model developed in the previous chapters. The combination of ship motion and winch payin/payout was shown to bring about substantial reduction in tether-induced disturbance on the vehicle during station-keeping of the ROPOS tethered underwater system in the face of an ocean current. This provides an interesting use of the dynamics model by allowing the computation of the cable disturbance force and demonstrating its mitigation through ship motion and winch activity. One possible application of this would be mission planning

for dexterous underwater intervention tasks and ROV thruster capacity analysis for specific missions. This rapid prototyping capability would be of value to the operators of tethered underwater systems as it reduces some of the uncertainty associated with the vehicle operation.

6.2 Future Work

Three areas for future work can be identified.

1. The profiles of the cable shown in Chapter 4 were obtained from time domain simulation using the dynamics model. These results could be verified using visual data for ROV tether deployments using a suitable data acquisition system. The comparison of shape data obtained and cable profiles predicted by the dynamics model could be used to verify the fidelity of the model, including the validity of the Eulerian framework whereby the variable length dynamics are restricted to the region of the cable close to the winch.

2. Torsional effects in a cable subjected to alternating low and high tensions are known to cause it to form kinks through the process of hockling. It would be interesting to investigate the effect of cable deployment/retrieval on the formation of kinks using the model developed here.

3. Presently, ROV pilots rely on experience and intuition while regulating the deployed tether during ROV missions. The dynamics model formulated here could serve as the kernel for a large scale virtual ROV pilot training system, to hone pilot skills without having to resort to costly live sea trials.

Bibliography

[1] Delaney, J.;Barnes, C.; Beauchamp, P.; Chave, A.;McNutt, M.; Madden, J.; "Project NEPTUNE: An interactive, regional cabled ocean observatory in the Northeast Pacific", *Oceans Conference Record (IEEE)*, v 2, 2003, p 1038-1042.

[2] Colombo, G.; Gaposchkin, E.M.; Grossi, M.D.; and Weiffennbach, G.C., "Long-tethered satellites for the Shuttle Orbiter". *Proceedings of the International Conference on Technology of Scientific Space Experiments*, Paris, France, May 1975.

[3] Leamy, M.J.; Noor, A.K.; Wasfy, T.M .," Dynamic simulation of a tethered satellite system using finite elements and fuzzy sets", *Computer Methods in Applied Mechanics and Engineering*, v 190, n 37-38, Jun 22, 2001, p 4847-4870.

[4] Kamman, James W. ; Huston, Ronald L.," Modeling of variable length towed and tethered cable systems", *Journal of Guidance, Control, and Dynamics*, v 22, n 4, 1999, p 602-608.

[5] Banerjee, Arun K.; and Do, Van N.," Deployment control of a cable connecting a ship to an underwater vehicle", *Journal of Guidance, Control, and Dynamics*, v 17, n 6, Nov-Dec, 1994, p 1327-1332.

[6] Makarenko, A. I.; Poddubnyi, V. I.; Kholopova, V. V., "Study of the Nonlinear Dynamics of Self-Propelled Submersibles Controlled by a Cable", *International Applied Mechanics*, v 33, n 3, 1997, p 251.

[7] Baddour, R.E.; Raman-Nair, W., "Marine tether dynamics: Retrieval and deployment from a heaving platform", *Ocean Engineering*, v 29, n 13, Jun 7, 2002, p 1633-1661.

[8] Triantafyllou, M.S; Howell, C.T., "Ill-Posed problem of a cable in compression", *International Journal of Offshore and Polar Engineering*, v 3, n 3, Sep, 1993, p 168-171.

[9] Burgess, J.J., "Equations of motion of a submerged cable with bending stiffness", *Proceedings of the International Offshore Mechanics and Arctic Engineering Symposium*, v 1, n pt A, Offshore Technology, 1992, p 283-290.

[10] Triantafyllou, Michael S.; Grosenbaugh, Mark A., "Robust control for underwater vehicle systems with time delays", *IEEE Journal of Oceanic Engineering*, v 16, n 1, Jan, 1991, p 146-151.

[11] Buckham, Brad; Driscoll, Frederick R.; Nahon, Meyer, "Development of a finite element cable model for use in low-tension dynamics simulation", *Journal of Applied Mechanics, Transactions ASME,* 71, n 4, July, 2004, p 476-485.

[12] Tiersten, M., "Force, momentum change, and motion", *American Journal of Physics,* v 37, 1969, p 82-87.

[13] De Sousa, Celia A. ; Rodrigues, Vitor H., "Mass redistribution in variable mass systems", *European Journal of Physics,* v 25, n 1, January, 2004, p 41-49.

[14] Walton, T.S.; Polachek, H.," Calculation of Transient Motion Submerged Cables", *Mathematics of Computation,* v 14, no. 69, 1960, p 27-46.

[15] Park, H.I; Jung, D.H.; Koterayama, W.," A numerical and experimental study on dynamics of a towed low tension cable", *Applied Ocean Research*, v 25, n 5, 2003, p 289-299.

[16] Ablow, C. M.; Schechter, S.," Numerical simulation of undersea cable dynamics", *Ocean Engineering*, v 10, n 6, 1983, p 443-457.

[17] Nordgren, R. P., "On computation of the motion of elastic rods", *Journal of Applied Mechanics, Transactions ASME*, v 41 Ser E, n 2, Sep, 1974, p 777-780.

[18] Love, A. E. H, *A Treatise on the Mathematical Theory of Elasticity*, Dover, New York, 1944.

[19] O'Brien, P.J.; McNamara, J.F., "Analysis of flexible riser systems subject to three-dimensional seastate loading", *Proceedings of the International Conference on Behaviour of Offshore Structures*, 1988, p 1373.

[20] Tabarrok, B.; Farshad, M.; Yi, H., "Finite element formulation of spatially curved and twisted rods", *Computer Methods in Applied Mechanics and Engineering,* v 70, n 3, Oct, 1988, p 275-299.

[21] Pinheiro, Mario J., "Some remarks about variable mass systems", *European Journal of Physics*,v 25, n 1, January, 2004, p L5-L7.

[22] Hulbert, Gregory M.; Chung, Jintai, "Time integration algorithm for structural dynamics with improved numerical dissipation: the generalized- α method", *Journal of Applied Mechanics, Transactions ASME*, v 60, n 2, Jun, 1993, p 371-375.

[23] Gobat, Jason I.; Grosenbaugh, Mark A.; Triantafyllou, Michael S., "Generalized-α time integration solutions for hanging chain dynamics", *Journal of Engineering Mechanics*, v 128, n 6, June, 2002, p 677-687.

[24] Buckham, Bradley J.; Driscoll, Frederick R.; Nahon, Meyer; Radanovic, Branka, "Torsional mechanics in dynamics simulation of low-tension marine tethers", *International Journal of Offshore and Polar Engineering*, v 14, n 3, September, 2004, p 218-226.

[25] Newmark, Nathan M., "Method of computation for structural dynamics", *AGARD Conference Proceedings*, v 2, 1972, p 1235-1264.

[26] Miranda, Isidoro ; Ferencz, Robert M.; Hughes, Thomas J.R. "Improved implicit-explicit time integration method for structural dynamics", *Earthquake Engineering & Structural Dynamics*, v 18, n 5, Jul, 1989, p 643-653.

[27] Press, W.;Flannery, B. P.;Teukolsky, S. A.; and Vetterling, W. T., *Numerical Recipes in C*, Cambridge, UK: Cambridge University Press, 1993.

[28] Steinke, Dean "Position and Orientation Estimation of an Underwater Vehicle using Model Based Signal Processing", Master of Applied Science Thesis, University of Victoria, 2005.

[29] Smith, O. J. M., "Closer control of loops with dead time", *Chemical Engineering Progress*, v 53, 1957, p 217-219.

[30] Kim, J.; Park, J.; Lee, S.; and Chong, E.K.P., "Control of Systems with Deadzones using PD Controllers with Fuzzy Precompensation," *Proc. of the 1993 IEEE International Symposium on Intelligent Control,* 1993, p 451-456.

[31] Bahill, A. Terry, "Simple adaptive smith-predictor for controlling time-delay systems", *IEEE Control Systems Magazine*, v 3, n 2, May, 1983, p 16-22.

[32] Dahlin, E. B., "Designing and tuning digital controllers",*Instrum. Control Syst.*,v 41 1968, p 77-83.

[33] Zhang, Weidong; He, Xing; Xu, Xiaoming, "Comparison of several well-known controllers used in process control", *ISA Transactions,* v 42, n 2, April, 2003, p 317-325.

[34] Garcia, Carlos E.; Morari, Manfred, "Internal model control - 1. Unifying review and some new results", *Industrial & Engineering Chemistry, Process Design and Development,* v 21, n 2, Apr, 1982, p 308-323.

[35] Smith, Cecil L., *Digital computer process control*, Intext Educational Publishers, Scranton, 1972.

[36] Smith, Carlos A., *Automated Continuous Process Control,* John Wiley & Sons, New York, 2002.

[37]K.J. Bathe and E.L. Wilson. *Numerical Methods in Finite Element Analysis*. Prentice-Hall, Englewood Cliffs, New Jersey, 1976.

[38] Modak, Sukomal; Sotelino, Elisa D., "The generalized method for structural dynamics applications", *Advances in Engineering Software,* 33, n 7-10, July/October, 2002, p 565-575.

[39] Kennedy, R.M., "Crosstalk dynamics of a long cable towed in the ocean", *Proc. IEEE Oceans,,* 1981, p 966-970.

Appendix A

Stability of Numerical Integrators

In this Appendix, the stability of the time domain integration associated with the use of the explicit and implicit integrators described in Section 4.2 is examined, following the results of Press et al [27]. When the time derivatives are approximated by backward differences, the resulting numerical scheme is referred to as the Explicit Euler scheme and when the time derivatives are approximated by forward differences, the Implicit Euler scheme results. A simple linear, first order differential equation is considered to demonstrate the superior stability of the implicit integration scheme for the linear problem.

Consider the equation

$$\frac{dy}{dt} = -cy \tag{A.1}$$

where $c > 0$, and t represents time.

The explicit Euler integration scheme based on the backward differences discretizes the continuous time derivative by considering the time differential term "back" at the start of the time step:

$$\frac{y_{n+1} - y_n}{h} = \left.\frac{dy}{dt}\right|_{t=n} \tag{A.2}$$

where h is the time step.

From equations (A.1) and (A.2),

$$y_{n+1} = (1 - ch) y_n \tag{A.3}$$

The implicit integration scheme uses a forward difference, with the time differential considered "forward" at the end of the time step:

$$\frac{y_{n+1} - y_n}{h} = \left.\frac{dy}{dt}\right|_{t=n+1} \tag{A.4}$$

From equations (A.1) and (A.4),

$$y_{n+1} = \frac{y_n}{1 + ch} \tag{A.5}$$

Equations (A.3) and (A.5) give the recurrence relations for the Explicit and Implicit Euler integrators. Next, a numerical example is considered. For an initial value of $y|_{t=0} = 1000$, the time domain response is computed for three different values of the time-step size, h, in Figure A.1.

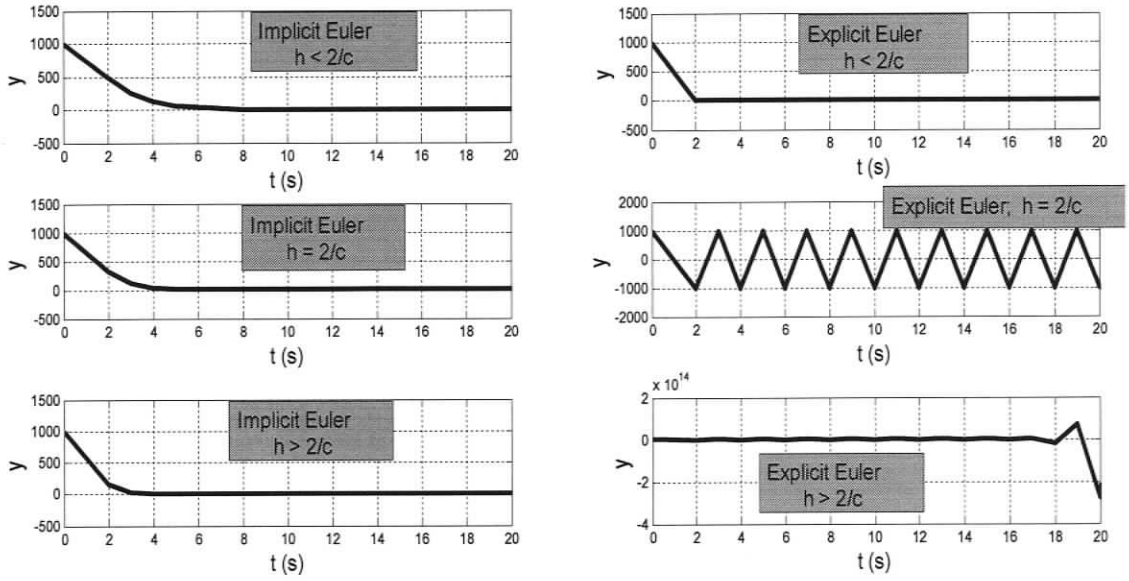

Figure A.1: Stability of the Explicit and Implicit Euler Integrators. The Implicit integrator is stable for any magnitude of the time step h for the linear problem considered here. The explicit integrator on the other hand is conditionally stable. It is stable for $h < 2/c$. For $h = 2/c$ it is critically stable, with sustained oscillations of constant frequency and amplitude. For $h > 2/c$ it is unstable, and the integrator "blows up" as seen.

From the preceeding, it is seen that for the explicit integrator, small time steps are required for stability. For a time step $h > 2/c$ in the explicit integrator, $|y_n| \to \infty$ as $n \to \infty$ in equation (A.3). On the other hand in equation (A.5) $y_n \to 0$ even for infinitely large time steps $h \to \infty$, which is the consistent with the analytical solution of equation (A.1) wherein y should decay exponentially to 0 as $t \to \infty$, thus establishing the unconditional stability of the implicit integrator.

These observations are valid only for the linear problem, as there exists no means to guarantee the stability of any integrator for a nonlinear governing differential equation.

However, the results here may serve as a guide when selecting integrators and time steps for the time domain simulation of the nonlinear cable dynamics equation in Chapter 4.

Appendix B

Smith and Dahlin Controllers

In this Appendix, the Smith Predictor Algorithm used by Grosenbaugh and Triantafyllou [10] in the design of the positioning system for the intermediary cage of a two-body tethered underwater vehicle is reviewed. The equivalence between the Smith Predictor and the Dahlin Controller used in the design of the longitudinal positioning system for the control node in Chapter 5 is brought out through the Internal Model Controller concept of Zhang et al [33]. This establishes a link between the present work and that of Grosenbaugh and Triantafyllou [10].

B.1 The Smith Predictor Control Algorithm

This control algorithm was developed by Otis Smith [29] in 1957. It represents the first step towards what is known today as the Model Predictive Control methodology. The transfer function of a process having a dead time of θ seconds is represented in the Laplace domain by:

$$L(s) = G(s)\, e^{-s\theta} \tag{B.1}$$

G(s) represents the rational part of the overall transfer function. Consider the process with dead time θ with a closed loop controller having transfer function $G_c(s)$ shown in Figure B.1

u

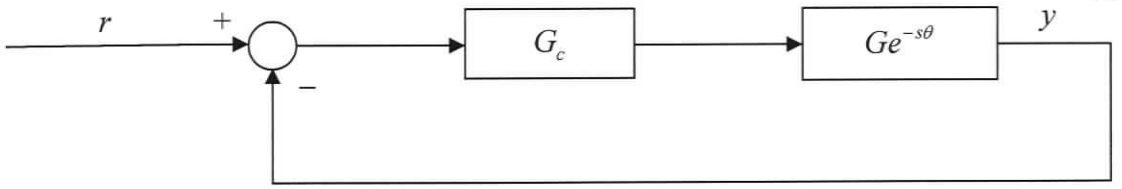

Figure B.1: Block diagram of process with dead time.

For the above system, *r(t)* is the reference input, *u(t)* is the control signal, and *y(t)* is the output. The closed loop transfer function is given by:

$$H(s) = \frac{G_c(s)\,G(s)e^{-s\theta}}{1+G_c(s)\,G(s)e^{-s\theta}} = \frac{Y(s)}{R(s)} \tag{B.2}$$

The roots of the characteristic polynomial which is given by $1+G_c(s)\,G(s)e^{-s\theta}$ must lie on the left half of the s-plane for Bounded Input Bounded Output (BIBO) stability. The presence of the exponential term in the denominator makes it difficult to obtain an exact evaluation of the characteristic polynomial. One may resort to representing the exponential by a series. This leads to a few options as reported by Bahill [31]. They are:

1. Taylor Series expansion:

$$e^{-s\theta} = 1 - s\theta + \frac{(s\theta)^2}{2!} - \frac{(s\theta)^3}{3!} + \ldots \tag{B.3}$$

2. Pade approximation:

$$e^{-s\theta} = \frac{1 - s\theta/2}{1 + s\theta/2} \tag{B.4}$$

3. Discrete time approximation:

$$e^{-s\theta} = z^{-nh} \tag{B.5}$$

where h is the sampling time and n is the closest integral value to the ratio $\frac{\theta}{h}$.

4. Laplace domain approximation:

$$e^{-s\theta} = \frac{1}{(1+\frac{s\theta}{n})^n} \tag{B.6}$$

where n is a large number.

To eliminate the dead time complications, the feedback loop needs to be adjusted to eliminate the $e^{-s\theta}$ term from the plant transfer function. The physical realization of this change is a measurement of control node longitudinal motion that would occur if the water pulley effect did not exist.

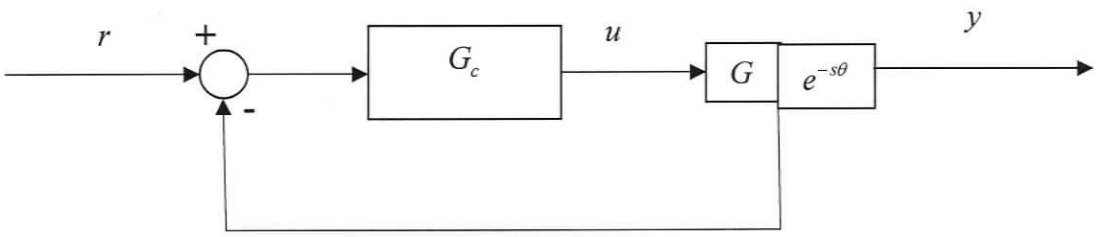

Figure B.2: Eliminating the effect of dead time.

However, this is not practical since the dead time is distributed across the process, and as such cannot be decoupled from the rational part of the overall transfer function. Smith proposed to model the plant as a first order system with dead time as:

$$Ge^{-s\theta} \approx \frac{e^{-s\theta}}{\tau s+1} \tag{B.7}$$

The rational part of the model open loop transfer function can be used to predict the effect of the controller output as shown in Figure B.3 below.

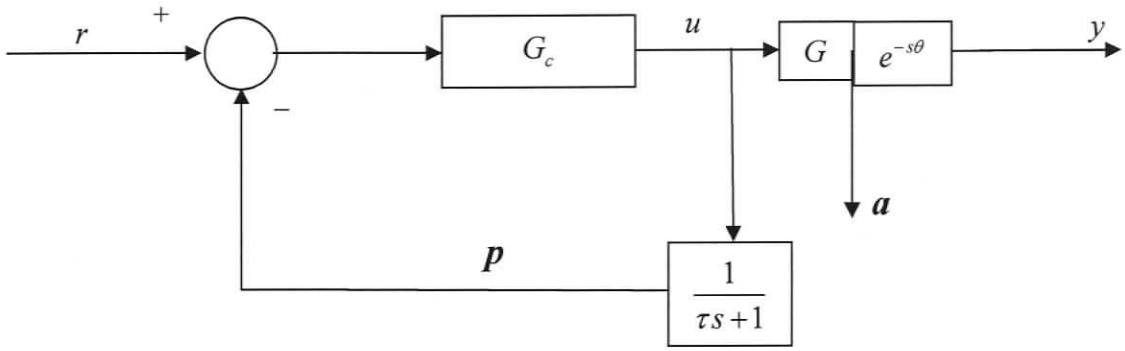

Figure B.3: Smith's model based prediction

In the above, the signal $\boldsymbol{p}$ is the prediction of the rational response of the system $\boldsymbol{a}$. Due to inaccuracies within the representative first order system, Smith proposed to correct the prediction model to get a refined estimate as shown in Figure B4.

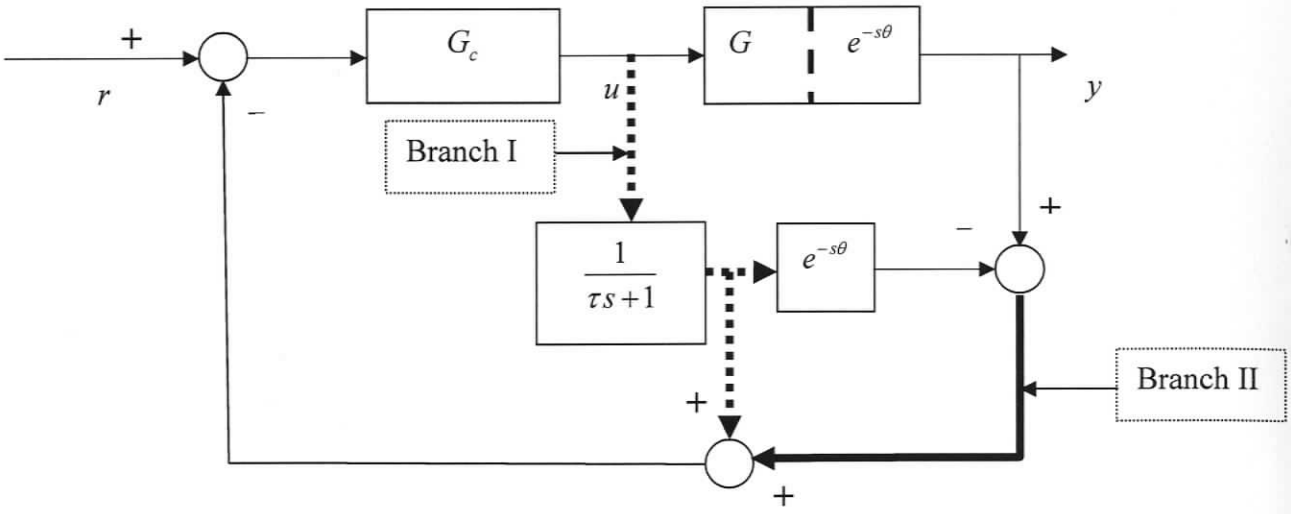

Figure B.4: Smith Predictor for systems with dead time

As seen in Figure B.4 above, whenever the controller changes its output u in an effort to correct the error signal, it receives the summation of two asynchronous feedback signals. Branch I provides immediate response through model based prediction. Branch II provides the correction to the model based prediction at a later instant, after the system dead time. The cumulative effect is a reduction of the influence of system dead time on the closed loop controller activity.

B.2 The Dahlin Controller

The Dahlin Controller has been discussed in detail Chapter 5, Section 5.6. The expression for the Controller was obtained as:

$$G_c(z) = \frac{Y(z)/R(z)}{G(z)(1-Y(z)/R(z))} \tag{B.8}$$

Where the output/input relation $Y(z)/R(z)$ is modeled as a first order process,

$$Y(z)/R(z) = \mathbf{Z}\left\{\frac{1}{(\lambda s+1)}\right\} \tag{B.9}$$

$G(z)$ is the discrete time form of the transfer function of the plant with dead time, being controlled. In the next section, we review recent work by Zhang et al [33] which shows the equivalence between the Dahlin and Smith Controllers through the Internal Model Control concept.

B.3 Equivalence between the Smith and the Dahlin controllers.

In this section the connection between the Dahlin and Smith Controllers is established. The block diagram for the Smith Predictor of Figure B.4 can be represented alternatively in Figure B.5.

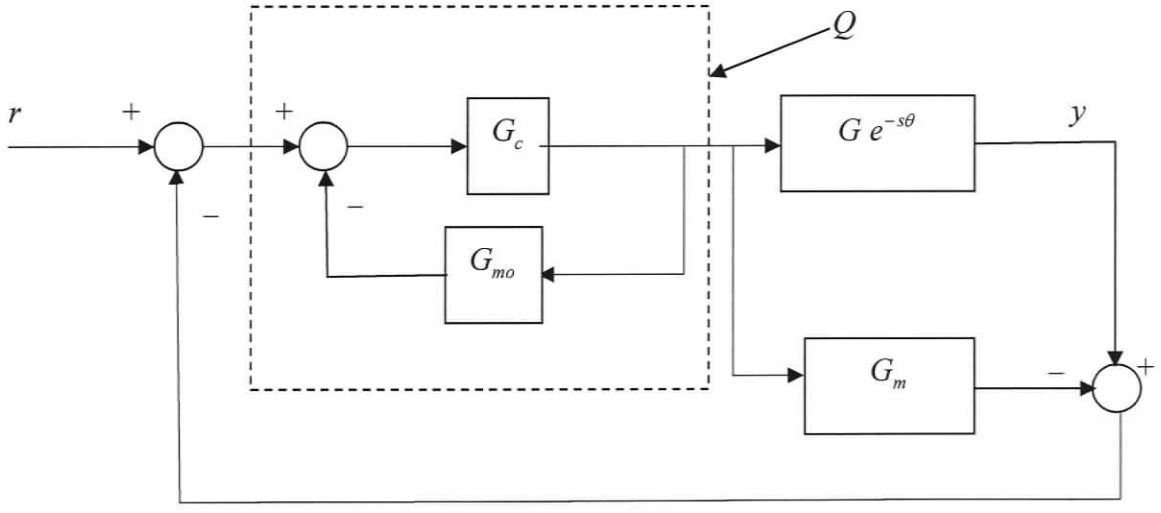

Figure B.5: Equivalent Smith Controller block diagram.

In the figure above, $G_m(s)$ is the model of the plant given by $G(s)$. $G_{mo}(s)$ is the rational delay-free part of the model transfer function $G_m(s)$. The overall closed loop transfer function for the above block diagram may be written as:

$$L(s) = \frac{G_c(s)\,G(s)e^{-s\theta}}{1+G_c(s)\left[G_{mo}(s)-G_m(s)+G(s)e^{-s\theta}\right]} \tag{B.10}$$

The block diagram of Figure B.5, with the difference between model predicted output and actual plant output as feedback, is the basis for Internal Model Control. Further details, and references, regarding the properties of Internal Model Controllers can be found in the work of Garcia and Morari [34]. According to the Internal Model Controller concept, the part of the block diagram within the dotted boundary is replaced by a single transfer function Q, which is given by:

$$Q(s) = \frac{G_c(s)}{1+G_{mo}(s)G_c(s)} \tag{B.11}$$

The controller transfer function is user-specified. It can be selected to match desired overall system response, subject to stability constraints as outlined by Garcia and Morari [34]. In this case, Q is selected as follows:

$$Q(s) = \frac{J(s)}{G_{mo}^{L}} \tag{B.12}$$

Where J is a filter having the same order as the plant being modeled, and is given as:

$$J(s) = \frac{1}{(\lambda s+1)^n} \tag{B.13}$$

The term in the denominator, G_{mo}^{L} is related to the rational part of the model transfer function G_{mo} as follows:

$$G_{mo}(s) = G_{mo}^{R}(s)\, G_{mo}^{L}(s) \tag{B.14}$$

Here G_{mo}^{R} contains all the right of the origin zeros of G_{mo} and G_{mo}^{L} contains all other terms. This selection ensures that the Internal Model Controller given by Q is stable. From the above, it is clear that the Smith Controller is given by:

$$G_{c}(s) = \frac{Q(s)}{1 - G_{mo}(s)Q(s)} \tag{B.15}$$

To fix our ideas, consider the plant modeled by a first order transfer function given by:

$$G_{m}(s) = \frac{e^{-\theta s}}{\tau s + 1} \tag{B.16}$$

By definition ,

$$G_{mo}(s) = \frac{1}{\tau s + 1} \tag{B.17}$$

since there are no right half plane zeros,

$$G_{mo}^{L}(s) = \frac{1}{\tau s + 1} \tag{B.18}$$

For the Internal Model Controller, the filter is defined as:

$$J(s) = \frac{1}{\lambda s + 1} \tag{B.19}$$

So, from equation (B.12)

$$Q(s) = \frac{\tau s + 1}{\lambda s + 1} \tag{B.20}$$

Consequently, the Smith Controller from equation (B.15) is given by:

$$G_c(s) = \frac{\tau s + 1}{\lambda s} \tag{B.21}$$

Now, a simple block diagram reduction shows that Figure B.5 for the Internal Model Controller can be represented by Figure B.6.

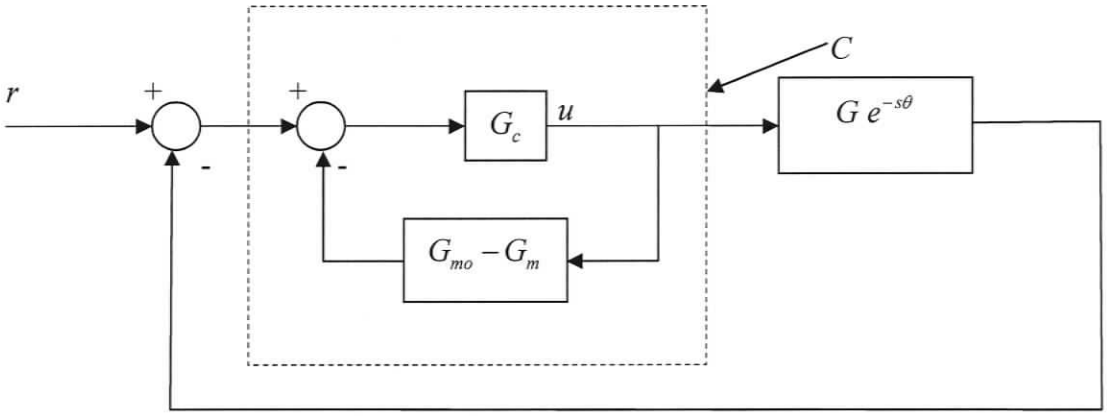

Figure B.6: Equivalent of the Internal Model Controller

At this point, the synergy between the Figure B.6 above, and the Figure 5.8 for the Digital Dahlin Controller is noted. It is clear that the Figure B.6 above is a continuous time version of the Dahlin Controller. From the above, the transfer function of the continuous Dahlin Controller is given by:

$$C(s) = \frac{G_c(s)}{1 + G_c(s)\left[G_{mo}(s) - G_m(s)\right]} \tag{B.22}$$

For the first order system under consideration, and for the Smith Controller G_c corresponding to the block diagram of Figure B.6, the above equation gives:

$$C(s) = \frac{\tau s + 1}{\lambda s + 1 - e^{-s\theta}} \tag{B.23}$$

Now consider the case of the direct design of the Dahlin Controller from Section B.2 previously. For the case at hand, considering the desired overall closed loop transfer function to have the same form as the filter $J(s)$ used in the Internal Model Controller,

$$\frac{Y(s)}{R(s)} = \frac{e^{-s\theta}}{\lambda s + 1} \tag{B.24}$$

And the plant is given by:

$$G(s) = \frac{e^{-\theta s}}{\tau s + 1} \tag{B.25}$$

From direct design equation (B.8) the Dahlin Controller is given by:

$$D(s) = \frac{\tau s + 1}{\lambda s + 1 - e^{-s\theta}} \tag{B.26}$$

Clearly, the form of the Dahlin Controller transfer function is identical when it obtained directly in equation (B.26) and when it is derived through the Internal Model Controller concept applied to the Smith Controller in equation (B.23). This demonstrates the equivalence of the Dahlin and the Smith Controllers, when the filter $J(s)$ is selected to be the same as the desired overall closed loop transfer function $\frac{Y(s)}{R(s)}$ of the Dahlin Controller. The Dahlin Controller is better suited for discrete time implementation since it is based directly on the standard digital control loop described in Section 5.6.